ВІСНИК
КИЇВСЬКОГО НАЦІОНАЛЬНОГО УНІВЕРСИТЕТУ ІМЕНІ ТАРАСА ШЕВЧЕНКА

ISSN 1728-2306

РАДІОФІЗИКА ТА ЕЛЕКТРОНІКА

17/2012

Засновано 1999 року

УДК 517

Публікуються результати експериментальних та теоретичних досліджень у галузях фізичної електроніки, фізики плазми, фізики поверхні твердого тіла, емісійної електроніки, кріогенної та мікроелектроніки, нанофізики та наноелектроніки, високотемпературної надпровідності, квантової радіофізики, функціональної електроніки, твердотільної електроніки, мобільного зв'язку, медичної радіофізики, методів отримання діагностичної інформації та її комп'ютерної обробки.

Для науковців, викладачів вищої школи, студентів.

Experimental and theoretical contributions are published in the following fields: physical electronics, plasma physics, solid-state surface physics, emission electronics, cryogenic electronics, microelectronics, nanophysics and nanoelectronics, high-temperature supercondactive electronics, solid-state electronics, functional electronics, microwave electronics, quantum electronics, mobile communication, medical radiophysics, methods of receipt and computer processing of diagnosis information

Designed for researches, university teachers, students.

ВІДПОВІДАЛЬНИЙ РЕДАКТОР	**І.О. Анісімов, д-р фіз.-мат. наук, проф.**
РЕДАКЦІЙНА КОЛЕГІЯ	**С.М. Левитський, д-р фіз.-мат. наук, проф. (заст. голов. ред.); В.І. Григорук, д-р фіз.-мат. наук, проф. (наук. ред.); Т.В. Родіонова, канд. фіз.-мат. наук, ст. наук. співроб. (відп. секр.); Ю.В. Бойко, канд. фіз.-мат. наук, доц.; В.І. Висоцький, д-р фіз.-мат. наук, проф.; В.В. Данилов, д-р фіз.-мат. наук, проф.; В.В. Ільченко, д-р фіз.-мат. наук, проф.; В.І. Кисленко, канд. фіз.-мат. наук, доц.; В.Ф. Коваленко, д-р фіз.-мат. наук, проф.; І.П. Коваль, канд. фіз.-мат. наук, доц.; М.В. Кононов, канд. фіз.-мат. наук, доц.; В.Г. Литовченко, д-р фіз.-мат. наук, проф.; Г.А. Мелков, д-р фіз.-мат. наук, проф.; В.А. Скришевський, д-р фіз.-мат. наук, проф.**
Адреса редколегії	**03127, Київ-127, просп. акад. Глушкова, 4 г, радіофізичний факультет; ☎ (38044) 526 0560**
Затверджено	**Вченою радою радіофізичного факультету 8 листопада 2010 року (протокол № 4)**
Атестовано	**Вищою атестаційною комісією України. Постанова Президії ВАК України № 1-05/1 від 10.02.10**
Зареєстровано	**Міністерством юстиції України. Свідоцтво про Державну реєстрацію КВ № 15797-4269Р від 02.10.09**
Засновник та видавець	**Київський національний університет імені Тараса Шевченка, Видавничо-поліграфічний центр "Київський університет" Свідоцтво внесено до Державного реєстру ДК № 1103 від 31.10.02**
Адреса видавця	**01601, Київ-601, б-р Т.Шевченка, 14, кімн. 43 ☎ (38044) 239 3172, 239 3222; факс 239 3128**

ЗМІСТ

Максюта М., Висоцький В.
Особливості каналювання релятивістських електронів у заряджених кристалографічних площинах іонних кристалів LiH і LiD 4

Максюта М., Висоцький В.
Особливості каналювання та квазіхарактеристичного випромінювання релятивістських електронів у заряджених кристалографічних площинах іонного кристалу LiF 14

Бех І, Ільченко В., Кравченко А., Телега В., Присяжний В.
Аналіз різних видів продуктів за допомогою напівпровідникових газових сенсорів на основі гетеропереходу SnO_2/p-Si 25

Васильєв Є., Колєнов С.
Дифракція світла на акустичних хвилях в періодичному шаруватому середовищі....28

Верба Р.
Мікрохвильові властивості гексагональних масивів магнітних наноточок 29

Ігнатьєв Я., Радченко С.
Ультразвуковий числовий структурний аналіз ефекту впливу гормонів щитовидної залози на стан її тканини......32

Ільченко О., Обуховський В., Ніконова В., Лемешко В., Куцик А.
Дослідження процесів комплексоутворення в системі метанол-вода за допомогою комбінаційного розсіювання світла....34

Костенко В., Сорочак А., Чамор Т., Чевнюк Л.
НВЧ і магнітні властивості алюмозаміщеного гексаферриту барію 39

Мелков Г., Слободянюк Д.
Поріг параметричної нестійкості в феромагнітному еліпсоїді....41

Моховик А., Радченко С.
Просторове 3D моделювання поширення ультразвуку в стохастично неоднорідних м'яких біологічних тканинах....43

Нетреба А., Нагуляк О., Кононов М.
Реконструкція та сегментація зображень зважених за дифузією з використанням звичайних томографічних даних 46

Павлюк С., Кузьмич Р.
Вплив зовнішньої температури на модифікацію параметрів діодів потужним імпульсом струму....48

Прокопенко О.
Пороговий мікрохвильовий детектор на основі спінового вентиля 50

Танигіна Д., Анісімов І., Левитський С.
Формування потоків заряджених частинок в фоновій плазмі на початковій стадії плазмово-пучкової нестійкості.......52

CONTENTS

Maksyuta M., Vysotskii V.
The peculiarities of relativistic electron channeling in charged crystallographic planes of LiH and LiD ionic crystals 4

Maksyuta M., Vysotskii V.
The pecularities of the channeling and quasicharacteristic radiation of relativistic electrons in charged crystallographic planes of LiF ionic crystal 14

Bekh I., İl'chenko V., Kravchenko A., Telega V., Prysyazhny V.
Analysis of the different kinds of food by semiconductor SnO_2/p-Si sensors 25

Vasyliev I., Kolenov S.
Diffraction of light by acoustic waves in periodic layered 28

Verba R.
Microwave properties of hexagonal arrays of magnetic nano-dots 29

Ignatyev Y., Radchenko S.
Ultrasound quantitative textural analysis in effect of thyroid hormones' influence on tissue gland state 32

İl'chehko O., Obukhovsky V., Nikonova V., Lemeshko V., Kutsyk A.
Raman spectroscopy research on complexation processes in water-methanol solutions 34

Kostenko V., Sorochak A., Chamor T., Chevnyuk L.
Microwave and magnetic properties of aluminium substituted barium hexaferrite 39

Melkov G., Slobodianiuk D.
Prallel pumping threshold in ferromagnetic ellipsoid 41

Mokhovyk A., Radchenko S.
Spatial 3d simulating of the ultrasound propagation in stochastic heterogeneous soft biological tissues 43

Netreba A., Naguliak O., Kononov M.
Diffusion weighted image segmentation and reconstruction using simple MRI data 46

Pavlyuk S., Kuzmych R.
Impact of temperature to modification of diode's parameters of powerful current pulse 48

Prokopenko O.
Threshold spin-torque microwave detector 50

Tanygina D., Anisimov I., Levitsky S.
Formation of charged particles' flows in the background plasma at the initial stage of the beam-plasma instability 52

UDC 539.12

M. Maksyuta, Ph. D., V. Vysotskii, Dr. Sci.

THE PECULIARITIES OF RELATIVISTIC ELECTRON CHANNELING IN CHARGED CRYSTALLOGRAPHIC PLANES OF LiH AND LiD IONIC CRYSTALS

У роботі розглядається каналювання релятивістських електронів у заряджених площинах іонних кристалів LiH і LiD. Показується, що при переході в цих кристалах до високоіндексних кристалографічних площин можливі інверсії потенціальних ям у потенціальні бар'єри. Досліджується також вплив температурного фактора на структури потенціалів взаємодії релятивістських електронів з такими високоіндексними зарядженими площинами. У випадку заряджених площин (111) проводиться розрахунок енергетичних рівнів і спектральних інтенсивностей, а на їх основі здійснюється ідентифікація спектральних ліній з експериментально існуючими спектрами випромінювання.

Ключові слова: каналювання релятивістських електронів, високоіндексні кристалографічні площини, іонні кристали, спектральна інтенсивність, позитроноподібність

The paper deals with the consideration of relativistic electron channeling in charged planes of LiH and LiD crystals. It is shown that the inversions of potential pits into potential barriers may occur at using of high indices crystallographic planes of these crystals. It is also investigated the influence of temperature factor on structures of interaction potentials of relativistic electrons with the high indices charged planes. In the case of the charged planes (111) the calculation of energy levels and spectral intensities is made and the identification of spectral lines to experimentally existing spectral radiations is carried out on their basis.

Keywords: relativistic electron channeling, high indices crystallographic planes, ionic crystals, spectral intensity, positron-likeness

Introduction. The problems of the creation of the intensive sources of short wave radiation and the obtaining of high-directed controlled mono-energetic charged particles beams are still urgent. Great attention is paid to the problem of relativistic particle beams turning. To solve these problems in [6 – 8] it has been proposed to carry out the channeling of the charged particles in the charged planes of ionic crystals of NaCl-type possessing some anomalous peculiarities (in particular in ionic LiH crystal). The essence of these anomalies deals with the fact that in these crystals in positive charged crystallographic planes and axis for the channeling negative charged particles there occur quite deep potential pits in spite of low electron and nucleus densities in these domains. At the same time in negative charged planes and axis the depths of the potential pits decrease, i.e. the orientation motion of negative charged particles in these planes becomes partially positron-like (in particular cases it may be completely positron-like). Such a motion regime could be used, for example, for the optimization of the radiation sources on the basis of the channeling relativistic electrons.

In consequence, in the case of the channeling of positively charged particles an electron-like motion regime arises when the trajectories of the channeling particles cross the planes or chains of crystal atoms. This effect, in particular, can be used for the optimization of nucleus synthesis systems on the basis of particle beams of the same type correlating in a certain way with orientated crystal targets containing nuclei of different type.

At the usage of covalent crystals it is impossible to realize similar regimes in crystals consisting of atoms of any type. In particular, for the crystal lattices of light elements the arising potential pits are not sufficiently deep for getting an intensive high-energetic radiation. From the other side, in the case of heavy atom crystals for which a great binding energy of the channeling particles with crystal matrices exist, the main are the processes of particle exit from the orientation movement regime (such, for example, as dechanneling, dissipation, absorption). Thus, the desirable is the situation when there may coexist both, for the first sight, mutually exceptional factors: the existence of low electron and nucleus densities in the regions of the particles channeling and great binding energies of the particles channeling with crystals. As shown in [7, 8], the advance in this question solution is possible at the realization of planar channeling in the charged (111) – planes of ionic crystal LiH. The given paper deals with the investigation of these phenomena just for ionic LiD crystal.

Note that these crystals are unique objects both for the creation of the effective sources of quasi-characteristic rigid radiation on the basis of the channeling effect and for thermonucleus investigations on the basis of *dd* and *dt* synthesis.

Besides, the given paper shows that the charged particle orientation movement in high indices charged $(2m+1, 2n+1, 2p+1)$ planes of the considered crystals (here m, n, p – non-negative natural numbers) possesses additional anomalous properties (in particular, the influence of temperature factor is investigated).

The calculation of interaction potentials of relativistic electrons with the charged crystallographic planes of LiH and LiD crystals. Let's calculate the potentials of the charged particles interaction with arbitrary charged $(2m+1, 2n+1, 2p+1)$ planes of LiH and LiD crystals. To carry out the numerical analysis it is necessary to proceed from the following one-partial electrostatic potentials for Li^+ and H^- (D^-) ions. At this calculating these one-partial potentials in the case of Li^+ ions the wave function $\psi_1(r)=\sqrt{Z^*/\pi a_0}\exp\left(-Z^* r/a_0\right)$ is used for 1*s*-electrons (localized nearby lithium nucleus) [4], and for 2*s*-electron (partially localized nearby lithium nucleus) the wave function $\psi_2(r)=\left(2\lambda_2^6 r/15\pi a_0^6\right)^{1/2}\exp\left(-\lambda_2 r/a_0\right)$ is used where $\lambda_2 \approx 0{,}797$ [9]. In the case of H^- ion its both electrons will be described by $\psi(r_1,r_2)=C\left[\exp\left(-\alpha_0 r_1-\beta_0 r_2\right)+\exp\left(-\alpha_0 r_2-\beta_0 r_1\right)\right]$ Chandrasekhar wave function, where $C=\left(8\pi a_0^3\right)^{-1}\left[\left(64\alpha_0^3\beta_0^3\right)^{-1}+\left(\alpha_0+\beta_0\right)^{-6}\right]^{-1/2}$ – a normalization $\alpha_0 = 1{,}039$ constant, $\beta_0 = 0{,}283$ (see, for example, [12]). The potentials got in such a way have a form:

$$\varphi_+(r)=e\left\{2\left(\frac{Z^*}{a_0}+\frac{1}{r}\right)\exp\left(-\frac{2Z^*}{a_0}r\right)+\frac{2\lambda_2^4(1-\alpha)}{15a_0^4}\left(r^3+\frac{4a_0}{\lambda_2}r^2+\frac{9a_0^2}{\lambda_2^2}r+\frac{12a_0^3}{\lambda_2^3}+\frac{15a_0^4}{2\lambda_2^4 r}\right)\exp\left(-\frac{r}{a_0}\right)+\frac{\alpha}{r}\right\}, \qquad (1a)$$

$$\varphi_-(r)=e\left\{\frac{(1+\alpha)}{2(1+\kappa_0)}\left[\exp\left(-\frac{2\alpha_0 r}{a_0}\right)\left(\frac{1}{r}+\frac{\alpha_0}{a_0}\right)+\exp\left(-\frac{2\beta_0 r}{a_0}\right)\left(\frac{1}{r}+\frac{\beta_0}{a_0}\right)+2\kappa_0\exp\left[-\frac{(\alpha_0+\beta_0)r}{a_0}\right]\right]-\frac{\alpha}{r}\right\}, \qquad (1b)$$

where a_0 – Bohr radius; $\kappa_0 = 64\alpha_0^3\beta_0^3/(\alpha_0+\beta_0)^6$; $Z^* = Z_{\mathrm{Li}} - \beta = 43/16$ – screened nuclei charge of Li^+; $\beta = 5/16$ – screening parameter corresponding to Li^+ nucleus and calculated by means of a variation method taking into account the fact that every of 1s – electrons partially screens Li^+ ion nucleus from another electron; α – degree of binding ionicity, which determines the probability of electron presence (belonging to Li atoms) nearby H atoms. The contribution of the third electron of Li^+ ion we calculate accounting its $1-\alpha$ probability to be found in the field of a screened lithium nucleus formula and with α probability in the field of hydrogen nucleus formula. It explains the presence of $1-\alpha$ and $1+\alpha$ multipliers in (1a), (1b) formulas.

Thus, from the formulas (1a) and (1b) it is evident that electrostatic potentials of Li^+ and H^- (D^-) ions are represented as a sum of components exponentially descendent and changed by Coulomb law. It means that the first components are originated by electro neutral skeleton of corresponding ions and the second ones arise as a consequence of non-compensated positive or negative charges that in definite directions lead to the origination of the charged axis or charged planes. On the basis of the following standard procedure of the averaging by the planes:

$$V(x) = \frac{2\pi Q}{S}\int_0^\infty \rho\varphi\left(r = \sqrt{\rho^2 + x^2}\right)d\rho, \qquad (2)$$

where S – a square of two-dimensional elementary cell in the channeling planes (see, for example, [4]) with the usage of the formulas (1a), (1b) instead of the potential $\varphi(r)$ in (2) we get the following expression for the potential of the charged particles of Q (further $Q = -e$, since we consider channelling of electrons) charges interaction with all "frozen" charged $(2m+1, 2n+1, 2p+1)$ planes built in turn of Li^+ and H^- (D^-) ions:

$$\begin{aligned} V(x) = V_0 \sum_{k=-\infty}^{\infty} \Bigg\{ & \left(\left|x-kd\right| + \frac{3}{\lambda_*}\right)\exp\left(-\lambda_*\left|x-kd\right|\right) + (1-\alpha)\exp\left(-\frac{2\lambda_2\left|x-kd\right|}{a_0}\right)\left[\frac{\lambda_2^3(x-kd)^4}{15a_0^3} + \frac{2\lambda_2^2\left|x-kd\right|^3}{5a_0^2} + \frac{6\lambda_2(x-kd)^2}{5a_0} + \right. \\ & \left. + 2\left|x-kd\right| + \frac{3a_0}{2\lambda_2}\right] + \frac{(1+\alpha)}{4(1+\kappa_0)}\left[\left(\left|x-kd+\frac{d}{2}\right| + \frac{3a_0}{2\alpha_0}\right)\exp\left(-\frac{2\alpha_0}{a_0}\left|x-kd-\frac{d}{2}\right|\right) + \left(\left|x-kd-\frac{d}{2}\right| + \frac{3a_0}{2\beta_0}\right)\exp\left(-\frac{2\beta_0}{a_0}\left|x-kd-\frac{d}{2}\right|\right) + \right. \\ & \left. + 2\kappa_0\left(\left|x-kd-\frac{d}{2}\right| + \frac{3a_0}{\alpha_0+\beta_0}\right)\exp\left(-\frac{(\alpha_0+\beta_0)}{a_0}\left|x-kd-\frac{d}{2}\right|\right)\right] - \alpha\left(\left|x-kd\right| - \frac{d}{4}\right)\cdot\chi\left(\frac{d}{2} - \left|x-kd\right|\right)\Bigg\}, \end{aligned} \qquad (3)$$

where $V_0 = -2\pi e^2/S$, $\chi(x)$ – a step-like Heaviside function, $\lambda_* = 2Z^*/a_0$. In Fig. 1 the interaction potentials (3) are shown on one period at electron channeling, respectively, in "frozen" charged (111), (311) and (331) planes.

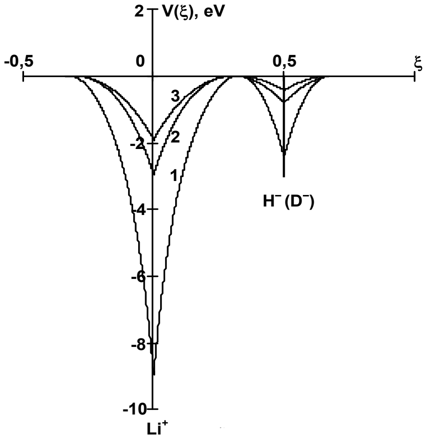

Fig. 1. Electron interaction potentials at their channeling in LiH (or LiD) crystal along charged "frozen" (111) planes (the curve 1), (311) (the curve 2) and (331) (the curve 3)

In this and following figures the distances along abscissa axis correspond to dimensionless $\xi = x/d$ units, where $d = a\Big/\sqrt{(2m+1)^2 + (2n+1)^2 + (2p+1)^2}$ – a distance between crystallographic planes of $(2m+1, 2n+1, 2p+1)$ including Li^+ and H^- (D^-) ions, a – a crystal lattice period. More detailed consideration concerning the receiving of the last component in the formula (3) will be given in the conclusion of the paper.

As it is seen from Fig. 1, these potentials common character in spite of the essential changes of potential pits depth and also the distance between the charged planes at the transition to higher indices directions does not change: the potential pits are present both in Li^+ "frozen" planes and in H^- (D^-) "frozen" planes. It is easy to show that on these planes the potential (3) satisfies the following boundary conditions:

$$\left[\frac{\partial V(kd+0)}{\partial x} - \frac{\partial V(kd-0)}{\partial x}\right] = -\frac{4\pi e^2}{S}Z_{\mathrm{Li}}, \qquad (4)$$

$$\left[\frac{\partial V(kd+d/2+0)}{\partial x} - \frac{\partial V(kd+d/2-0)}{\partial x}\right] = -\frac{4\pi e^2}{S}Z_{\mathrm{H,D}}.$$

Conditions (4) mean that nuclei distribution density on "frozen" planes has a singular character; i.e. is expressed as follows:

$$\rho(x) = \frac{e}{S}\sum_{k=-\infty}^{\infty}\left[Z_{\mathrm{Li}}\,\delta(x-kd) + Z_{\mathrm{H}}\,\delta(x-kd+d/2)\right], \qquad (5)$$

where $\delta(x)$ – Dirac delta-function. It should be emphasized, that the potential obtained in the paper (the curve 1 in Fig. 1) at choosing the degree of ionicity $\alpha \approx 0{,}98$, coincides with the potential obtained in [10] for the analogous "frozen" planes.

However the situation is essentially different accounting the thermal motion of ions: due to the space oscillations of the ions of LiH crystal caused by the thermal motion the inversion of potential pits into the potential barriers is possible. Before confirming the fact let's stop on the procedure of the potential averaging (3) by the thermal oscillations.

By means of the function of the ions deviation from the equilibrium position

$$f(x) = \left(2\pi u^2\right)^{-1/2}\exp\left(-x^2/2u^2\right), \qquad (6)$$

where u – an average amplitude of thermal oscillations, the averaging by the thermal oscillations is represented as the following convolution [2]:

$$U(x)=\int_{-\infty}^{\infty}V(x-y)f(y)dy\ . \qquad (7)$$

Finally, after substituting (3) and (6) into (7) we get the following interaction potential averaging by the thermal oscillations with $(2m+1,2n+1,2p+1)$ planes of LiH (LiD) crystal:

$$U(x)=\sum_{k=-\infty}^{\infty}\left[U_{+}^{(1)}(x-kd)+\frac{(1-\alpha)}{4}U_{+}^{(2)}(x-kd)+\frac{(1+\alpha)}{2}U_{-}(x-kd-d/2)+U_{\pm}(x-kd)\right]=W_0(x)+W_{\pm}(x), \qquad (8)$$

$$U_{+}^{(1)}(x)=-\frac{V_0}{2}\exp\left(\frac{\lambda_* u_+^2}{2}\right)\left\{\exp(-\lambda_* x)\left[P_1^{(+1)}(x)\,\mathrm{erfc}\,\tau_{+1}(x)+u_+\sqrt{\frac{2}{\pi}}\right]\exp\left[-\left(\tau_{+1}(x)^2\right)\right]-\right.$$
$$\left.-\exp(\lambda_* x)\left[P_1^{(+2)}(x)\,\mathrm{erfc}\,\tau_{+2}(x)-u_+\sqrt{\frac{2}{\pi}}\right]\exp\left[-\left(\tau_{+2}(x)^2\right)\right]\right\}, \qquad (8.1)$$

$$U_{+}^{(2)}(x)=-\frac{V_0}{2}\exp\left(\frac{\lambda_0^2 u_+^2}{2}\right)\left\{\exp(-\lambda_0 x)\left[P_4^{(+1)}(x)\,\mathrm{erfc}\,\kappa_{+1}(x)+P_3^{(+1)}(x)\sqrt{\frac{2}{\pi}}\exp\left[-\left(\kappa_{+1}(x)^2\right)\right]\right]+\right.$$
$$\left.+\exp(\lambda_0 x)\left[P_4^{(+2)}(x)\,\mathrm{erfc}\,\kappa_{+2}(x)+P_3^{(+2)}(x)\sqrt{\frac{2}{\pi}}\exp\left[-\left(\kappa_{+2}(x)^2\right)\right]\right]\right\}, \qquad (8.2)$$

$$U_{-}(x)=-\frac{V_0}{2(1+\kappa_0)}\left\{\exp\left(\frac{2\alpha_0^2u_-^2}{a_0^2}\right)\left\{\exp\left(-\frac{2\alpha_0 x}{a_0}\right)\left[P_1^{(-1\alpha_0)}(x)\,\mathrm{erfc}\,\tau_{-1\alpha_0}(x)+u_-\sqrt{\frac{2}{\pi}}\right]\exp\left[-\left(\tau_{-1\alpha_0}(x)^2\right)\right]-\right.\right.$$
$$\left.-\exp\left(\frac{2\alpha_0 x}{a_0}\right)\left[P_1^{(-2\alpha_0)}(x)\,\mathrm{erfc}\,\tau_{-2\alpha_0}(x)+u_-\sqrt{\frac{2}{\pi}}\right]\exp\left[-\left(\tau_{-2\alpha_0}(x)^2\right)\right]\right\}+$$
$$+\exp\left(\frac{2\beta_0^2u_-^2}{a_0^2}\right)\left\{\exp\left(-\frac{2\beta_0 x}{a_0}\right)\left[P_1^{(-1\beta_0)}(x)\,\mathrm{erfc}\,\tau_{-1\beta_0}(x)+u_-\sqrt{\frac{2}{\pi}}\right]\exp\left[-\left(\tau_{-1\beta_0}(x)^2\right)\right]-\right.$$
$$\left.-\exp\left(\frac{2\beta_0 x}{a_0}\right)\left[P_1^{(-2\beta_0)}(x)\,\mathrm{erfc}\,\tau_{-2\beta_0}(x)+u_-\sqrt{\frac{2}{\pi}}\right]\exp\left[-\left(\tau_{-2\beta_0}(x)^2\right)\right]\right\}+$$
$$+2\kappa_0\exp\left(\frac{(\alpha_0+\beta_0)^2u_-^2}{2a_0^2}\right)\left\{\exp\left(-\frac{(\alpha_0+\beta_0)x}{a_0}\right)\left[P_1^{(-1(\alpha_0+\beta_0))}(x)\,\mathrm{erfc}\,\tau_{-1(\alpha_0+\beta_0)}(x)+u_-\sqrt{\frac{2}{\pi}}\right]\exp\left[-\left(\tau_{-1(\alpha_0+\beta_0)}(x)^2\right)\right]-\right.$$
$$\left.\left.-\exp\left(\frac{(\alpha_0+\beta_0)x}{a_0}\right)\left[P_1^{(-2(\alpha_0+\beta_0))}(x)\,\mathrm{erfc}\,\tau_{-2(\alpha_0+\beta_0)}(x)+u_-\sqrt{\frac{2}{\pi}}\right]\exp\left[-\left(\tau_{-2(\alpha_0+\beta_0)}(x)^2\right)\right]\right\}\right\}, \qquad (8.3)$$

$$U_{\pm}(x)=\alpha V_0\left[x\,\mathrm{erf}\left(\frac{x}{u_+}\right)+u_+\sqrt{\frac{2}{\pi}}\exp\left[-\frac{x^2}{2u_+^2}\right]-(x-d/2)\,\mathrm{erf}\left(\frac{x-d/2}{u_-}\right)-u_-\sqrt{\frac{2}{\pi}}\exp\left[-\frac{(x-d/2)^2}{2u_-^2}\right]\right], \qquad (8.4)$$

where $P_1^{(+1,+2)}(x)=x\mp\frac{3}{\lambda_*}\pm\lambda_* u_+^2$, $P_1^{(-1\alpha_0,-2\alpha_0)}(x)=x\mp\frac{3a_0}{2\alpha_0}\pm\frac{2\alpha_0u_-^2}{a_0}$, $P_1^{(-1\beta_0,-2\beta_0)}(x)=x\mp\frac{3a_0}{2\beta_0}\pm\frac{2\beta_0u_-^2}{a_0}$,

$P_1^{(-1(\alpha_0+\beta_0),-2(\alpha_0+\beta_0))}(x)=x\mp\frac{3a_0}{(\alpha_0+\beta_0)}\pm\frac{(\alpha_0+\beta_0)u_-^2}{a_0}$, $P_3^{(+1,+2)}(x)=\pm\frac{\lambda_0^3}{60}x^3+\frac{\lambda_0^2\left(4-\lambda_0^2u_+^2\right)}{20}x^2\pm\frac{\lambda_0\left(3\lambda_0^4u_+^4-19\lambda_0^2u_+^2+72\right)}{60}x-$

$-\frac{\lambda_0^6u_+^6}{60}+\frac{7\lambda_0^4u_+^4}{60}-\frac{4\lambda_0^2u_+^2}{5}+4$, $P_4^{(+1,+2)}(x)=\frac{\lambda_0^3}{60}x^4\mp\frac{\lambda_0^2\left(\lambda_0^2u_+^2-3\right)}{15}x^3+\frac{\lambda_0\left(\lambda_0^4u_+^4-5\lambda_0^2u_+^2+12\right)}{10}x^2\mp$,

$\mp\frac{\left(\lambda_0^6u_+^6-6\lambda_0^4u_+^4+27\lambda_0^2u_+^2-60\right)}{15}x+\frac{\lambda_0^7u_+^8}{60}-\frac{\lambda_0^5u_+^6}{10}+\frac{13\lambda_0^3u_+^4}{20}-\frac{14\lambda_0u_+^2}{5}+\frac{6}{\lambda_0}$, $\tau_{-1\alpha_0,-2\alpha_0}(x)=\frac{1}{\sqrt{2}}\left(\frac{2\alpha_0u_-}{a_0}\mp\frac{x}{u_-}\right)$,

$\tau_{-1\beta_0,-2\beta_0}(x)=\frac{1}{\sqrt{2}}\left(\frac{2\beta_0u_-}{a_0}\mp\frac{x}{u_-}\right)$, $\tau_{-1(\alpha_0+\beta_0),-2(\alpha_0+\beta_0)}(x)=\frac{1}{\sqrt{2}}\left(\frac{(\alpha_0+\beta_0)u_-}{a_0}\mp\frac{x}{u_-}\right)$, $\tau_{+1,+2}(x)=\frac{1}{\sqrt{2}}\left(\lambda_* u_+\mp\frac{x}{u_+}\right)$,

$\kappa_{+1,+2}(x)=\frac{1}{\sqrt{2}}\left(\lambda_0u_+\mp\frac{x}{u_+}\right)$, $\lambda_0=2\lambda_2/a_0$, $W_0(x)$ – the interaction potential originated by electro neutral skeletons of Li^+ and H^- (D^-) ions, $W_{\pm}(x)$ – interaction potential occurring as a result of non-compensated positive and negative charges of these ions (in the final part of this paper we'll return to these potentials analyzing them in detail). Here u_+ and u_- – the amplitudes of thermal oscillations of Li^+ and H^- (D^-) ions, respectively, which are calculated below accordingly with Debye theory (see, for example, [2]):

$$u_{\pm}=\hbar\left\{\frac{3}{m_{\pm}k_BT_D}\left[\frac{1}{4}+\left(\frac{T}{T_D}\right)^2\int_0^{T_D/T}\frac{\xi d\xi}{\exp\xi-1}\right]\right\}^{1/2}, \qquad (9)$$

where $m_{\pm}$ – Li^+ and H^- ion masses respectively T_D – Debye temperature.

Let's turn to the consideration of temperature factor influence on the interaction potential (8) in LiH and LiD crystals. In the case of LiH crystal for the numerical meanings of $m_+ \approx 6{,}941 m_A$, $u_- \approx 0{,}205A$, $T_D = 860$ K by means of the formula (9) we find the values of the magnitudes of thermal oscillations: at $T = 0$ K – $u_+ \approx 0{,}078A$, $u_- \approx 0{,}205A$, at $T = 600$ K – $u_+ \approx 0{,}234A$, $u_- \approx 0{,}352A$. Here m_A – atomic unit of the mass. Substituting these meanings into the formulas (8.1) ÷ (8.4) and further into (8), we are convinced of the existence of the potential pits at $T = 0$ K in H^- (111) planes potential pits exist and starting from $T = 600$ K, disappear. This transformation corresponds to the inversion of potential pits into the barriers and is represented in Fig. 2.

The situation is essentially different accounting ion thermal motion. In real situation, as it is shown below, when it is necessary to take into account the space oscillations of crystal ions caused by thermal motion, the inversion of potential pits into potential barriers is possible. For example, in LiH crystal in H^- (111) planes the potential pit depths decrease at temperature increase and at $T = 600$ K, as it is illustrated in Fig. 2, these pits transform into potential barriers.

Just in the case of LiD crystal accounting the greater mass of D^- ions, thermal oscillation amplitudes of u_- will be smaller and that is why the transformation of the potential pits into potential barriers should have been taken place at somewhat higher temperature of the crystal. The estimations show that this temperature is essentially higher then the temperature of crystal fusion i.e. unlike LiH crystal the inversion effect of the potential pits into the potential barriers for LiD crystal in (111) planes is not observed.

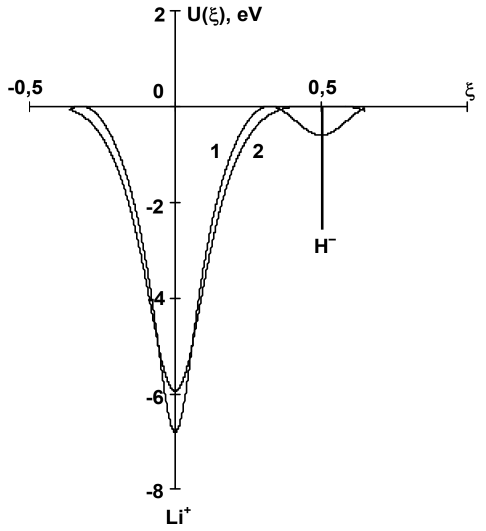

Fig. 2. Electron interaction potential at their channeling in LiH crystal along (111) charged planes: at T = 0 K – the curve 1; at T = 600 K – the curve 2

Essential changes of the structure of interaction potentials take place at the transition to high indices charged planes as well. In Fig. 3a, b it is illustrated the potential barriers appearance at the transition from Li^+ (111) planes to Li^+ (311) ones (at this the amplitudes of the thermal oscillations are equal to $u_+ \approx 0{,}102A$, $u_- \approx 0{,}266A$, were calculated at $T = 300$ K by means of the formula (9)).

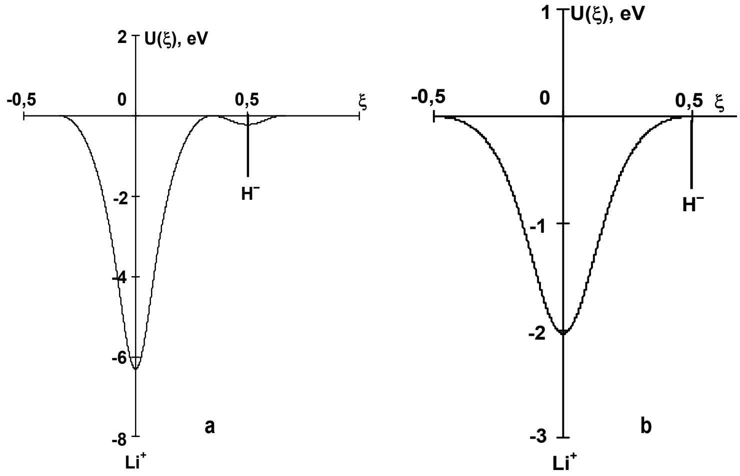

Fig. 3. Interaction potentials of the channeling electrons in LiH crystal at T = 300 K: (a) – with (111) planes; (b) – with (311) planes

In Fig. 4a, 4b the analogous appearance of the potential barriers is shown for LiD crystal at the transition from (111) planes to (331) ones (at this the amplitudes of the thermal oscillations equal to $u_+ \approx 0{,}102A$, $u_- \approx 0{,}188A$, are also calculated at $T = 300$ K by means of the formula (9)).

Thus from Fig. 3 and Fig. 4 it is seen that both for the case of LiH crystal and LiD one the inversion of the potential pits into the potential barriers occurs just at $T = 300$ K, however for higher indices crystallographic planes: for LiH, beginning from (311) planes and for LiD, beginning from (331) ones.

Now let's proceed to the analysis of the arising radiation transitions in the potential pits shown in Fig. 3 and Fig. 4, and to the calculation of the spectral intensities as well.

The investigation of quasi-characteristic radiation (QCR) at relativistic electron channeling in charged crystallographic planes of LiH and LiD crystals. Let's write down the solution of the following one-dimensional stationary Schrödinger equation with the relativistic mass of $m\gamma$ (m – electron rest mass):

$$\left[-\frac{\hbar^2}{2m\gamma}\frac{d^2}{dx^2}+U(x)\right]\psi(x)=\varepsilon\psi(x), \qquad (10)$$

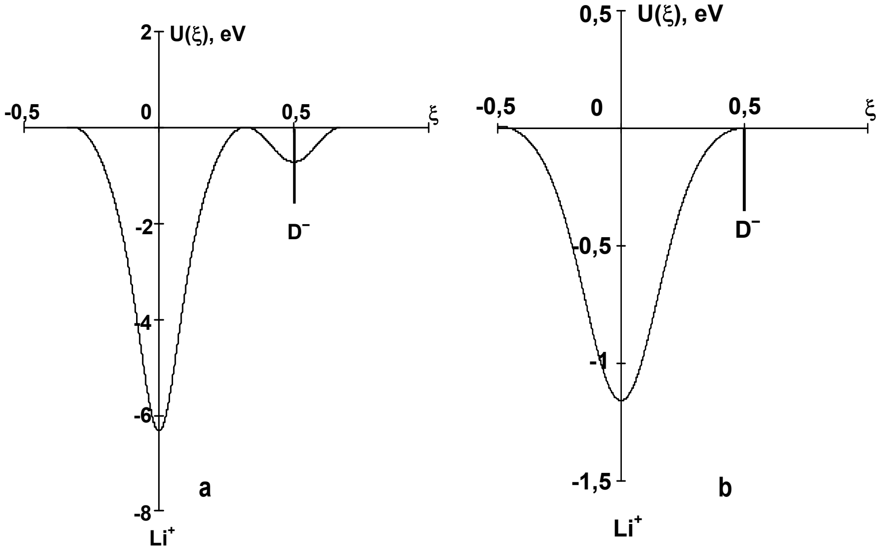

Fig. 4. Interaction potentials of the channeling electrons in LiD crystal at T = 300 K: (a) – with (111) planes; (b) – with (311) planes

in which for the potential $U(x)$ energy, as it is usually done in the case of planar channeling (see, for example, [2]), we choose the following Pashle-Telller approximation:

$$U(x) = -U_0\,\mathrm{ch}^{-2}\left(\frac{x}{b}\right). \tag{11}$$

After the substitution of (11) into (10) we get the energy level spectra of the transverse motion

$$\varepsilon_n = -\frac{\hbar^2}{2m\gamma b^2}(s-n)^2, \quad n = 0,1,\ldots,[s], \tag{12}$$

where $s = \left(2m\gamma U_0 b^2/\hbar^2 + 1/4\right)^{1/2} - 1/2$, $[s]$ – the integer part of *s* number, and also their corresponding proper wave functions

$$\psi_n(x) = \frac{\Gamma(2s-2n+1)}{2\Gamma(s-n+1)}\left[\frac{n!(s-n)}{b\Gamma(2s-n+1)}\right]^{1/2}\left(\mathrm{ch}\frac{x}{b}\right)^{n-s}\cdot \\ \cdot C_n^{s-n+1/2}\left(\mathrm{th}\frac{x}{b}\right), \tag{13}$$

where $\Gamma(x)$ – a Gamma-function, $C_n^{\lambda}(x)$ – a Gegenbauer polynomial [3].

Let's start the investigation of radiation transitions and QCR spectrum for LiH crystal. We calculate the meanings of U_0 and *b* parameters for the potential pits represented in Fig. 3a, b in the case of relativistic electron channeling with Lorentz-factor of $\gamma = 106{,}7$ (this meaning γ is taken from [13]), and also for every potential pit we find *s* parameters and by means of the formula (12), at last we calculate the energy levels of the channeling motion. Thus, for the potential pits in Li^+ (111) planes we have $U_0 \approx 6{,}32\,\mathrm{eV}$, $b \approx 0{,}28A$, $s \approx 3{,}26$, $\varepsilon_0 \approx -4{,}83eV$, $\varepsilon_1 \approx -2{,}32eV$, $\varepsilon_2 \approx -0{,}72eV$, $\varepsilon_3 \approx -0{,}03eV$; in H^- (111) planes – $U_0' \approx 0{,}22\,\mathrm{eV}$, $b' \approx 0{,}22A$, $s' \approx 0{,}24$, $\varepsilon_{0'} \approx -0{,}04eV$; in Li^+ (311) planes – $U_0 \approx 2{,}06\,\mathrm{eV}$, $b \approx 0{,}21A$, $s \approx 1{,}17$, $\varepsilon_0 \approx -1{,}11eV$, $\varepsilon_1 \approx -0{,}02eV$. These energy levels are shown in Fig. 5a, b.

By means of the energetic channeling particles proceeding from the theory of the radiation

$$\hbar\omega_{mn} = 2\gamma^2(\varepsilon_m - \varepsilon_n) \tag{14}$$

(see, for example, [2]) we calculate the energies of the spectral lines of quasi-characteristic radiation (QCR), occurring for direct radiation transitions between the neighboring energy levels in Li^+ (111) potential pits (in Fig. 5a they are schematically marked by vertical arrows): $\hbar\omega_{10} \approx 54{,}6\,\mathrm{keV}$, $\hbar\omega_{21} \approx 36{,}5\,\mathrm{keV}$, $\hbar\omega_{32} \approx 17{,}2\,\mathrm{keV}$, and also for indirect $0' \to 1$, $0' \to 2$, $0' \to 0$ tunnel transitions (in Fig. 5a these transitions are represented by inclined arrows): $\hbar\omega_{0'1} \approx 51{,}8\,\mathrm{keV}$, $\hbar\omega_{0'2} \approx 15{,}4\,\mathrm{keV}$, $\hbar\omega_{0'0} \approx 109\,\mathrm{keV}$. Comparing these data with the given meanings in Table 1 in [13] one may conclude that we observe a close fit only for the second spectral line with $37\,\mathrm{keV}$ energy. The first spectral line is formed not only for the expense of direct $1 \to 0$ transitions but at the expense of the tunnel $0' \to 1$ transitions (at this as it will be shown further, their partial contribution is compared with the one of direct transitions). Just the appearance of the third line of the radiation in the energy regions of $20\,\mathrm{keV}$ we explain not at the expense of the tunnel $0' \to 1$ transitions (similar pick of QCR in our case is concentrated in the domain of energies of some $50\,\mathrm{keV}$), but for the expense of $3 \to 2$ transitions realized in the potential pits of Li^+ (111) planes and at the expense of the tunnel $0' \to 2$ transitions from $n = 0'$ levels of shallow potential pits in H^- (111) planes on $n = 2$ levels of deeper neighbor potential pits in Li^+ (111) planes arises in the same energy region (more convincing argumentation on the basis of spectral intensity calculation of (QCR) is given below).

Fig. 5c by means of vertical arrows represents the identification of the experimental picks of the radiation taken from [13] with radiation transitions realized in our paper.

Thus as it follows from Fig. 5c the first two lines demonstrate a satisfactory identification. Just in the case of the third not very distinct one the identification with $3 \to 2$ and $0' \to 2$ transitions becomes possible as due to great depths of energy levels $n' = 0'$ and $n = 2,3$ (it represents schematically in Fig. 5a) the radiation on these transitions may exceed the domain of $25\,\mathrm{keV}$ energies.

To be completely convinced in the correctness of our calculations and to make clear the contribution of all the radiation transitions into a complete version let's find out just a spectral intensity in correspondence with the following formula [2]:

$$\frac{dI}{d\omega}=\frac{e^2\omega}{c^3}\left\{\sum_{i=1}^{3}x_{i,i-1}^2\Omega_{i,i-1}^2 f\left(\frac{\omega}{2\gamma^2\Omega_{i,i-1}}\right)P_i(\vartheta)+P_{0'}(\vartheta)\sum_{j=0}^{2}x_{0',j}^2\Omega_{0',j}^2 f\left(\frac{\omega}{2\gamma^2\Omega_{0',j}}\right)\right\}, \qquad (15)$$

where $f(x)=\left(1-2x+2x^2\right)\chi(1-x)$, $\Omega_{i,i-1}=\frac{\hbar\left[2(s-i)+1\right]}{2m\gamma b^2}$ – a frequency of a straight transition between a neighboring energy levels of $i,i-1$ in Li^+ – pit, $\Omega_{0',j}=\frac{\hbar}{2m\gamma}\left[\frac{(s-j)^2}{b^2}-\frac{s'^2}{b'^2}\right]$ – a frequency of a tunnel transition between the energy level of $0'$ in H^- – pit and the energy level of *j* in Li^+ – pit, $P_i(\vartheta)$, $P_{0'}(\vartheta)$ – the probabilities of the channeling particles capture accordingly on the levels of *i* and 0′, $\vartheta\approx p_x/mc\gamma$ – the angle of particles incidence on a crystal. Supposing the description of a particle transverse motion by a plane wave $\psi(x)=(d)^{-1/2}\exp(ip_x x/\hbar)$, we get the magnitudes $P_n(\vartheta)$ calculated in accordance with the theory of sudden perturbations in a following way [2]:

$$P_n(\vartheta)=\frac{1}{d}\left|\int_{-d/2}^{d/2}\exp\left(\frac{im\gamma\vartheta x}{\hbar}\right)\psi_n(x)\,dx\right|^2. \qquad (16)$$

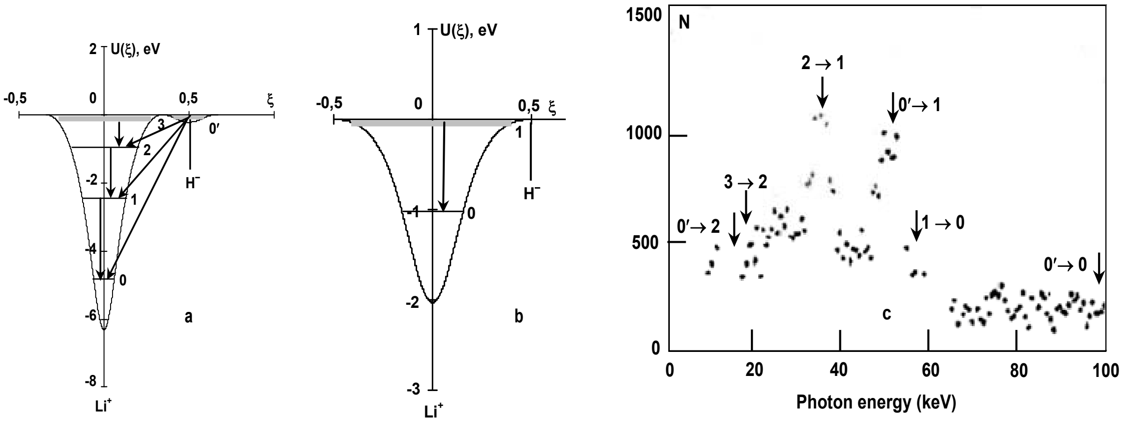

Fig. 5. Interaction potentials and the systems of the transverse energy ε_n levels arising at electron channeling with a longitudinal energy *E* = 54 MeV in LiH crystal at T = 300 K:
(a) – along (111) planes; (b) – along (311) ones (the arrows show the considered radiation transitions).
(c) –the measured radiation spectrum arising for the electrons channeling along (111) planes in LiH-crystal with the same energy taken in [13] (the arrows illustrate the identification of the spectral lines with the radiation transitions arising in our paper, ordinate axis shows the intensity in the number of *N* radiation impulses)

Proceeding from the common formula (13) let's write down the following wave functions at the definite meanings $n'=0'$ and $n=1,2,3$:

$$\psi_{0'}(x)=\frac{1}{2^{s'}\Gamma(s')}\left[\frac{2\Gamma(2s')}{b'}\right]^{1/2}\text{ch}^{-s'}\left(\frac{x}{b'}\right), \qquad (17.1)$$

$$\psi_1(x)=\frac{1}{2^{s-1}\Gamma(s)}\left[\frac{(s-1)\Gamma(2s)}{b}\right]^{1/2}\text{sh}\left(\frac{x}{b}\right)\text{ch}^{-s}\left(\frac{x}{b}\right), \qquad (17.2)$$

$$\psi_2(x)=\frac{1}{2^{s-2}\Gamma(s)}\left[\frac{(s-2)\Gamma(2s)}{2(2s-1)b}\right]^{1/2}\text{ch}^{-s}\left(\frac{x}{b}\right)\cdot\left[(s-1)\text{sh}^2\left(\frac{x}{b}\right)-\frac{1}{2}\right], \qquad (17.3)$$

$$\psi_3(x)=\frac{1}{2^{s-1}\Gamma(s)}\left[\frac{(s-1)(s-3)\Gamma(2s)}{3(2s-1)b}\right]^{1/2}\text{ch}^{-s}\left(\frac{x}{b}\right)\cdot\text{sh}\left(\frac{x}{b}\right)\left[(2s-1)\text{sh}^2\left(\frac{x}{b}\right)-3\,\text{ch}^2\left(\frac{x}{b}\right)\right]. \qquad (17.4)$$

Fig. 6 represents the graphs of $P_n(\vartheta)$ functions, which are got after the substitution of wave functions (17.1) ÷ (17.4) into the formula (16). From Fig. 6 it is seen that at small incident angles the contribution to the radiation from tunnel transitions will be evident and, for example, the radiation at the expense of $1\to 0$ and $3\to 2$ transitions will be unessential. It means that the formation of the first and the third spectral lines occur to some extent at the expense of the tunnel transitions. However to make the picture of spectrum radiation clearer it is necessary to know matrix elements of all multipole moments (in the given paper we'll be restricted to dipole transitions).

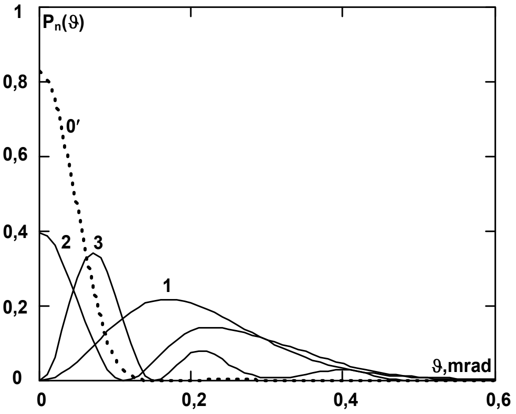

Fig. 6. The probabilities of a capture on $\varepsilon_{0'}$ and ε_n (*n* = 1, 2, 3) levels in a plane channel (111) of LiH crystal for *E* = 54 MeV electrons in dependence of a flying angle of ϑ measured in milliradians

Matrix elements of $x_{1,0}$, $x_{2,1}$ and $x_{3,2}$ dipole transitions are found from the following formula [2]:

$$x_{m,m-1}=\frac{b(m-1)!}{2\Gamma(2s-m+1)}\left[\frac{m(s-m)(s-m+1)}{2s-m+1}\right]^{1/2}\sum_{l=0}^{m}\sum_{k=0}^{m-1}\frac{(-1)^{k+l}\,\Gamma(2s+k-m+2)\Gamma(2s-m+l+1)}{2^{k+l}k!l!(m-l)!(m-k-1)!\Gamma(s+l-m+1)\Gamma(s+k-m+2)}\cdot$$

$$\cdot\sum_{p=0}^{k+l}\frac{(-1)^{p}(k+l)!}{(k+l-p)!\Gamma(2s-2m+p+1)}\sum_{r=0}^{p}\frac{(-1)^{r}}{r!(p-r)!}\sum_{i=0}^{\infty}\frac{(-1)^{i}\,\Gamma(2s-2m+p+i+1)}{i!(r+s+i-m+1/2)^{2}}, \tag{18}$$

i.e. we have

$$x_{1,0}=b\left(\frac{s-1}{2}\right)^{1/2}\left(\frac{\Gamma\left(s-\frac{1}{2}\right)}{\Gamma(s)}\right)^{2},\ x_{2,1}=\frac{(4s-5)}{(2s-3)^{2}}\left[(s-2)(2s-1)\right]^{1/2}x_{1,0},\ x_{3,2}=\frac{3b\left(8s^{2}-24s+13\right)}{(2s-3)(2s-5)^{2}}\left[\frac{(s-2)(s-3)}{3}\right]^{1/2}x_{1,0}\,. \tag{19}$$

Just the matrix elements of $x_{0',0}$, $x_{0',1}$ and $x_{0',2}$ dipole tunnel transitions are calculated in accordance with the following expression:

$$x_{0',m}=\int_{-\infty}^{+\infty}\psi_{0'}(x)x\psi_{m}(x-d/2)dx\,. \tag{20}$$

Using the probabilities of the capture of $P_{0'}(\vartheta)$, $P_1(\vartheta)$, $P_2(\vartheta)$ and $P_3(\vartheta)$ calculated for three meanings of the incident angles of $\vartheta_1\approx 0{,}02\,\mathrm{mrad}$, $\vartheta_2\approx 0{,}04\,\mathrm{mrad}$, and $\vartheta_3\approx 0{,}06\,\mathrm{mrad}$ (these angles are less than Lindhard critical angles $\vartheta_c\approx\sqrt{U_0/mc^2\gamma}\approx 0{,}3\,\mathrm{mrad}$, $\vartheta_c'\approx\sqrt{U_0'/mc^2\gamma}\approx 0{,}07\,\mathrm{mrad}$ accordingly in the potential pits of Li^+ (111) and H^- (111) planes) and also the meanings of the dipole transitions matrix elements found by the formulas of (19) and (20) by means of the formula (15) we get the graphic dependencies of relative spectral densities of QCR intensity $\zeta(\omega)=(dI/d\omega)/(dI/d\omega)_{\max}$, constructed below in Fig. 7a, b, c.

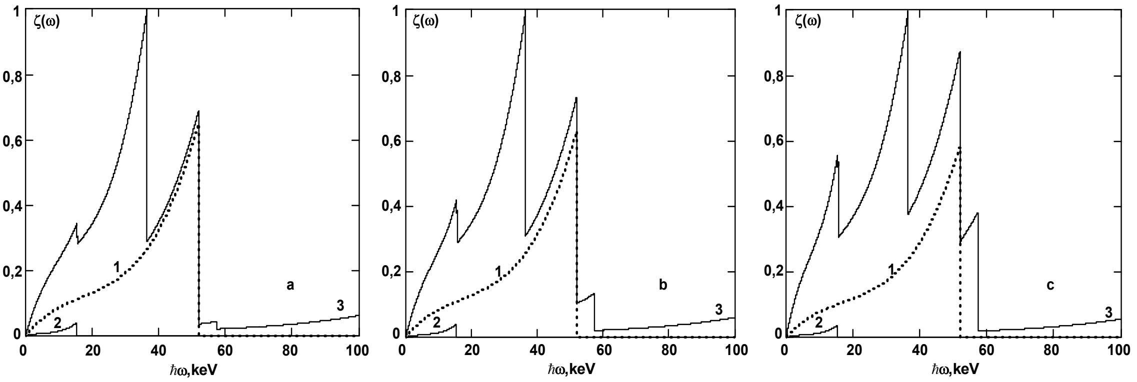

Fig. 7. Relative spectral density of QCR intensity (calculated in a dipole approximation) occurring at relativistic electron channeling with *E* = 54 MeV energy along the crystallographic (111) planes of LiH crystal in the cases of incident angles of: (a) – ϑ = 0,02 mrad, (b) – ϑ = 0,04 mrad, (c) – ϑ = 0,06 mrad. Numbers 1, 2, 3 indicate the partial contributions into a complete radiation of the radiation bound to 0′→1, 0′→2 and 0′→0 tunnel transitions, respectively

These figures show that we may estimate the partial contribution of the radiation to the total picture of QCR spectrum at all the transitions at the incident angle alternation. For example, it is evident that the radiation at the expense of the tunnel $0'\to 0$ and $0'\to 2$ transitions is small. Fig. 7a, b, c just observe that the incident angle increase causes the decrease of the weight part of the radiation due to $0'\to 1$ transitions (dotted curves) and at $\vartheta > 0{,}1\,\mathrm{mrad}$, as it follows from Fig. 6 this radiation does not give any partial contribution at all. It is seen that in the energy region up to $20\,\mathrm{keV}$ the radiation is almost completely formed at the expense of the radiation transitions $3\to 2$, $2\to 1$ and $0'\to 1$ transitions (there is a little contribution on a background level from direct $1\to 0$ transitions and from the tunnel $0'\to 2$ and $0'\to 0$ transitions), in the energy regions from $20\,\mathrm{keV}$ to approximately $40\,\mathrm{keV}$ $2\to 1$ and $0'\to 1$ transitions are playing the main role and there is a negligible contribution from $1\to 0$ and $0'\to 0$ transitions, in the energy regions of $20\div 60\,\mathrm{keV}$ QCR appears at the expense of $0'\to 1$ and $1\to 0$ transitions with a negligible contribution from $0'\to 0$ transitions and at last, in the energy regions higher $60\,\mathrm{keV}$ there is only radiation due to the tunnel $0'\to 0$ transitions (the radiation at the expense of $3\to 0$ transitions will be an order lower).

Thus, even in this very idealized case quite a close fit is observed between the experimental dependence shown in Fig. 5c, and the theoretical dependencies calculated by means of the formula (15) not accounting the widths of the energy levels and electron beam angular dispersion (as it is seen from Fig. 7a, b the closest fit is realized at small incident angles of the particles on a crystal). A more realistic situation could be considered when an angular divergence of an incident beam of electrons is taken into account. It is demonstrated below as the example on LiD crystal.

Let's accounting for the angular divergence of the electron beam. For this at first let's carry out in the following way a probability averaging of the channeling particle capture $P_n(\vartheta)$ by means of a normal distribution $g(\vartheta)=\left(2\pi\vartheta_0^2\right)^{1/2}\exp\left(-\vartheta^2/2\vartheta_0^2\right)$ (here ϑ_0 – an angular dispersion):

$$\left\langle P_n(\vartheta)\right\rangle = \int_{-\infty}^{\infty} P_n(\vartheta-\vartheta')g(\vartheta')d\vartheta' . \qquad (21)$$

In Fig. 8 the dependences (21) are constructed for $\vartheta_0 \approx 0{,}15\,\text{mrad}$ meaning.

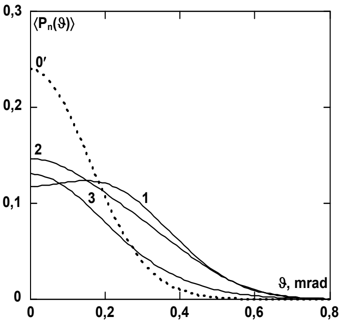

Fig. 8. Averaging probabilities of a capture on $\varepsilon_{0'}$ and ε_n (n = 1, 2, 3) levels in a planar channel (111) of LiH crystal for E = 54 MeV electrons depending on a striking corner ϑ, measured in milliradians

As it is seen from Fig. 8 the averaging of population probability from one side leads to the decrease of the total spectral intensity and from the other side even at small incident angles ϑ it is possible to observe the radiation on $1 \to 0$ transition.

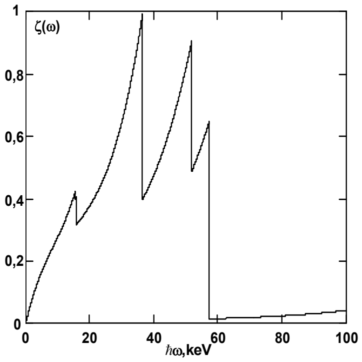

Fig. 9. The spectral intensity of QCR calculated in a dipole approximation and occurring at a beam of relativistic electrons E = 54 MeV channeling along crystallographic (111) planes of LiH crystal (with an angular dispersion of $\vartheta_0 \approx 0{,}15$ mrad and the incident angle of $\vartheta = 0$)

This is illustrated in Fig. 9, where the graph of a relative spectral density of intensity $\zeta(\omega)$ for a zero incident angle is constructed by the formula (15), in which instead of functions $P_n(\vartheta)$ the functions $\left\langle P_n(\vartheta)\right\rangle$.are substituted. Besides, the dependence in Fig. 9 proves a significant contribution of the tunnel $0' \to 1$ transitions into the radiation (it is evident from the structure of the first spectral line).

Thus, note that in common there quite a close fit between the calculated spectral intensity given in Fig. 9 and the measured one in [13] (see Fig. 5c) (it is interesting to note that the third spectral line is small and indistinct, just as it is presented in Fig. 5c).

At the same time in the case of LiD crystal as it is shown in [16], the third spectral line in a spectrum low-energy region is more distinct as compared with the analogous spectral line in LiH crystal. To make clear the reason of such a difference it is necessary to repeat the calculation algorithm for LiD crystal as well. At $u_+ \approx 0{,}102A$, $u_- \approx 0{,}188A$ meanings of the amplitudes calculated at $\text{T} = 300$ K by means of the formula (9), we find the parameters of the arising potential pits using the formulas $(8.1) \div (8.4)$ and (11) and by means of the formula (12) calculate the system of the energy levels in them. In Li$^+$ (111) planes we have $U_0 \approx 6{,}34\,\text{eV}$, $b \approx 0{,}3A$, $s \approx 3{,}53$, $\varepsilon_0 \approx -4{,}94eV$, $\varepsilon_1 \approx -2{,}54eV$, $\varepsilon_2 \approx -0{,}93eV$, $\varepsilon_3 \approx -0{,}11eV$, and in H$^-$ (111) planes – $U_0' \approx 0{,}72\,\text{eV}$, $b' \approx 0{,}22A$, $s' \approx 0{,}61$, $\varepsilon_{0'} \approx -0{,}27eV$. The energies of QCR spectral lines which for this crystal were calculated at $\gamma = 106{,}7$ (see [13]), will be the following: $\hbar\omega_{10} \approx 54{,}7\,\text{keV}$, $\hbar\omega_{21} \approx 36{,}6\,\text{keV}$, $\hbar\omega_{32} \approx 18{,}6\,\text{keV}$, $\hbar\omega_{0'1} \approx 51{,}5\,\text{keV}$, $\hbar\omega_{0'2} \approx 14{,}8\,\text{keV}$ and $\hbar\omega_{0'0} \approx 106{,}1\,\text{keV}$. Fig. 10a illustrates these potential pits and their energy levels construction, Fig. 10b realizes the identification of the experimental picks with possible radiation transitions on the basis of these data by means of vertical arrows.

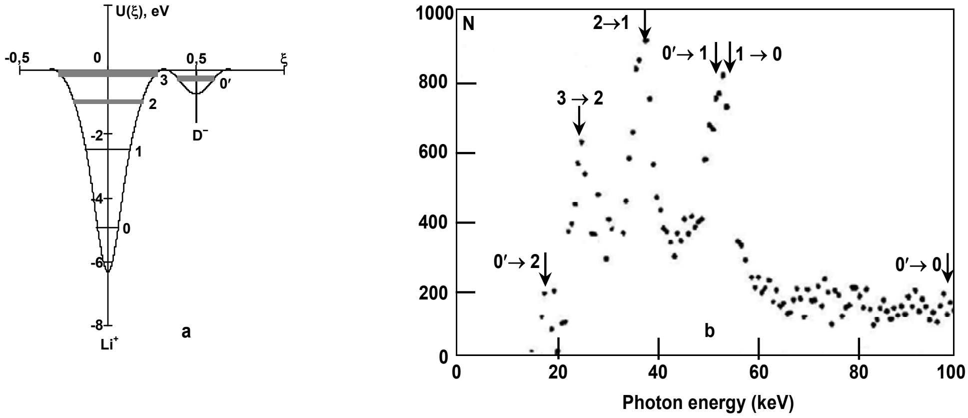

Fig. 10. (a) – the interaction potential and the transverse energy level system of the transverse energy ε_n, occurring at the channeling of electrons with the longitudinal energy E = 54 MeV in crystallographic (111) planes in LiD crystal at T = 300 K: (b) – the measured radiation spectrum arising at the channeling of such electrons along (111) planes in LiD crystal taken in [13] (the arrows illustrate the identification of spectral lines with the arising radiation transitions, in Fig. 10b along the ordinate axis the intensity is built in a number of N radiation impulses)

It is seen from here that like in the case of LiH crystal, the first line is formed at the expense of $0' \to 1$ and $1 \to 0$ transitions, the second – at the expense of $2 \to 1$ transitions, and the third one – at the expense of $3 \to 2$ transitions.

At this, since the depths of the potential pits in D^- (111) planes are almost three times exceed the depths of the analogous potential pits in H^- (111) planes, the energy level $0'$ is placed deeper that leads to the decrease of the specific contributions to the radiation from all the tunnel transitions (further it is confirmed by the calculation of the spectral intensity). Besides, the radiation at the expense of $0' \to 2$ transitions is shifted in a low-energy region of a spectrum. Note one more peculiarity of the received data. The first two spectral lines are quite in a close fit with the measured picks. Just the third line measured by ourselves is shifted in the domain of lesser energies. It can be explained by the fact that we didn't take into account the depths of the lines (the depths of the levels are schematically illustrated in Fig. 10a), limited both to zone broadening and a broadening at the expense of the processes of dissipation and de-channeling. It takes into account that upper 2 and 3 levels have limited widths, we could easily reach the energies of some $25\,\text{keV}$ order.

Now let's stop at the calculation of the spectral intensity for LiD crystal. At this we'll consider only the case with the dispersion choosing it by the dimension as for LiH crystal, namely, $\vartheta_0 \approx 0{,}15\,\text{mrad}$. Evidently, for more objective estimations and in given case we can't do without the graph construction for the averaging of the probability of the capture on the levels of the channeling $\varepsilon_{0'}$ and ε_n $(n = 1,2,3)$ in a planar (111) channel of LiD crystal. Accounting the above mentioned parameters for the potential pits in Li^+ (111) and D^- (111) planes by means of the formula (21) the functions of the averaged probabilities of the capture are calculated $\langle P_n(\vartheta)\rangle$, and in Fig. 11 their graphical dependencies by means of which one may trace the difference from the analogous dependences given in Fig. 8 are constructed.

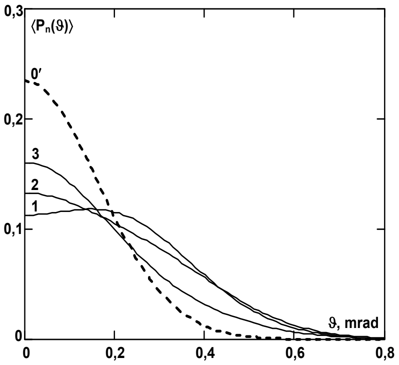

Fig. 11. Averaging probabilities of a capture on $\varepsilon_{0'}$ and ε_n (*n* = 1, 2, 3) levels in a planar channel (111) of LiD crystal for *E* = 54 MeV electrons depending on a striking corner ϑ, measured in milliradians

Really as it is seen from Fig. 11, the positions of the curves 2 and 3 have changed. If in Fig. 8 the curve 3 (describing the probability of the particle capture on the third energy level) was lower then the curve 2 (describing the probability of the particle capture on the second energy level), then in Fig. 8 the situation is opposite – now the curve 3 is upper than the curve 2. Evidently the fact is definite for the explanation of the third spectral line structure.

To be more convinced in the correctness of the above mentioned arguments let's carry out like in the case of LiH crystal the calculation of a spectral intensity by means of the formula (15), where instead of the functions $P_n(\vartheta)$ the functions of $\langle P_n(\vartheta)\rangle$. Afterwards we construct the graphic dependence of a relative spectral intensity density of QCR in the case of a zero incident angle and at the meaning of $\vartheta_0 \approx 0{,}15\,\text{mrad}$ angular dispersion. This construction is given below in Fig. 12 where in addition the contributions to a total spectral intensity density of QCR of $0' \to 0$, $0' \to 1$ and $0' \to 2$ tunnel transitions are shown (the curves 1, 2 and 3 respectively).

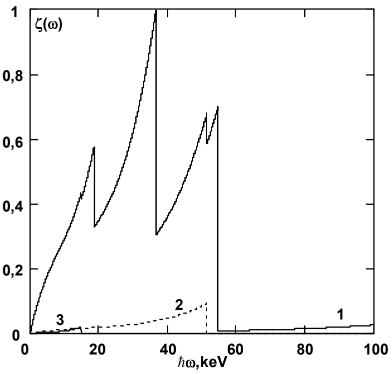

Fig. 12. The spectral intensity density of QCR calculated in a relative units in a dipole approximation and occurring at a beam of relativistic electrons *E* = 54 MeV channeling along (111) planes of LiD crystal (an electron beam has an angular dispersion of $\vartheta_0 \approx$ 0,15 mrad and the incident angle of ϑ = 0)

From Fig. 12 it is seen that the third spectral line becomes significantly more distinct at the background of two other lines than it was in the case of LiH crystal (see Fig. 9). Such an integral redistribution of the spectral intensity between three picks in the case of LiD crystal evidently is due to the change in the averaging probabilities of a capture which is demonstrated in Fig. 11 and deals with the decrease of the contribution to the radiation spectrum of $0' \to 1$ tunnel transitions (see the dotted curve 2 in Fig. 12). Thus, we have shown that there is almost a close fit between the experimental dependence given in Fig. 10b and a spectral dependence in Fig. 12 which convincingly proves the correctness of the calculated interaction potential (8).

Additional confirmation of the correctness of the calculated interaction potential (8) could be experimentally got the only spectral line with $\hbar\omega_{10}^{(311)} \approx 24{,}7\,\text{keV}$ energy occurring on $1 \to 0$ transition (see Fig. 5b) in the case of relativistic electrons channeling with $E = 54\,\text{MeV}$ energy along the charged (311) planes of LiH crystal.

In the conclusion of this item it is necessary to note that in the potential pits shown in Fig 10 in [13] and approximated by the functions $U_{\text{Li}^+}(x) = -5{,}2/\text{ch}^2(x/0{,}27)$ and $U_{\text{H}^-}(x) = -1{,}5/\text{ch}^2(x/0{,}24)$, the calculation by means of the formula (10) leads to the following energy levels: $\varepsilon_0 \approx -3{,}84\,\text{eV}$, $\varepsilon_1 \approx -1{,}59\,\text{eV}$, $\varepsilon_2 \approx -0{,}32\,\text{eV}$, $\varepsilon_{0'} \approx -0{,}8\,\text{eV}$, $\varepsilon_{1'} \approx -0{,}01\,\text{eV}$. From here, first, we get close fits of $0' \to 1$ tunnel transitions to the spectral lines with $18{,}34\,\text{keV}$ energy which does not coincide with $25\,\text{keV}$, declaring in [13] and, second, these data make it impossible to get for these data the second spectral line with the energy in the region of $37\,\text{keV}$.

One more mistaken explanation of the third line appearance is given in [13]. For the approximations of

$U_{\mathrm{Li}^+}(x) = -3{,}9/\mathrm{ch}^2(x/0{,}33)$, $U_{\mathrm{H}^-}(x) = -0{,}3/\mathrm{ch}^2(x/0{,}21)$, given in (10) by means of the formula (10) we get $\varepsilon_0 \approx -2{,}93\,\mathrm{eV}$, $\varepsilon_1 \approx -1{,}3\,\mathrm{eV}$, $\varepsilon_{0'} \approx -0{,}07\,\mathrm{eV}$. In this case $0' \to 1$ transition is close fit to the spectral line with the energy of some $28{,}55\,\mathrm{keV}$ order, which approximates $25\,\mathrm{keV}$ meaning. However at this it is impossible to get a spectral line with the energy in the region of $55\,\mathrm{keV}$ from three energetic levels.

General analysis of the effects of relativistic electron channeling in charged high-indices planes of ionic LiH и LiD crystals. To sum up we came to a general conclusion: the reasons of non-coincidence in the explanations of spectral line position both in the case of LiH and LiD crystals (in [13]) with our analytical results are evidently due to non-correct calculation of electron interaction potentials with charged planes in these papers (charged planes in these papers are not taken into account at all). Planar potential calculation leads in the long run to the following conditionally convergent series:

$$V_\pm(x) = V_0 \sum_{n=-\infty}^{\infty} \left[\left| x + nd - \frac{d}{2} \right| - \left| x + nd \right| \right]. \qquad (22)$$

From mathematical point of view series (22) don't lead to a definite meaning. However if takes into account a real physical situation where a longitudinal crystal dimension is many times less than the transverse one, the problem could be solved. Then as it was done in [8, 11], the interaction potential with the alternative positively and negatively charged "frozen" (111) planes (or Li^+ and H^- (D^-)) is represented as the following saw potential:

$$V_\pm(x) = \alpha V_0 \sum_{n=-\infty}^{\infty} \left[|x + nd| - \frac{d}{4} \right] \chi\left(\frac{d}{2} - |x + nd| \right). \qquad (23)$$

Further averaging the potential (23) by the thermal oscillations (in positively charged with u_+ amplitude and in negatively charged with u_- amplitude), we get a final expression

$$W_\pm(x) = \sum_{k=-\infty}^{\infty} U_\pm(x - kd). \qquad (24)$$

Namely this expression (24) is a consequence of Coulomb components in one-partial potentials (1a, b) and is not completely taken into account in [13]. It is easy to show that planar (111) potentials given in [13] for LiH and LiD crystals are almost close fit to our potentials at $\alpha = 0$ (these potentials are $U(x, \alpha = 0)$ in relative units ξ are shown in Fig. 13a).

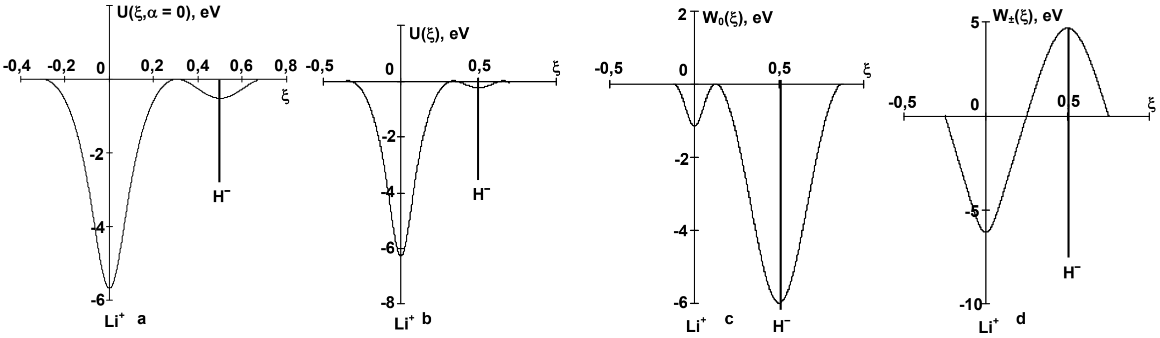

Fig. 13. Interaction potentials of channeling electrons with (111) planes of LiH crystal: (a) – in the case of $\alpha = 0$, corresponding to [10], (b) – in the case of $\alpha \neq 0$ corresponding to the results of our paper, (c) – originated of electroneutral skeletons of Li^+ and H^-ions, (d) – occurring of non-compensated positive and negative charges of these ions

Thus, interaction potentials of channeling electrons with (111) planes used in [13] (obtained on the basis of form-factor formalism) in the case of LiH are quite apparently different of the ones obtained in the given paper (compare with the Fig. 13b), which resulted in many non-coincidences in the positions of the spectral lines mentioned above. Besides, by means of analytical expression $U(x) = W_0(x) + W_\pm(x)$ it is easy to observe the contributions into the potential $U(x)$ of electron neutral main part $W_0(x)$ and non-compensated Coulomb part of $W_\pm(x)$. As it is seen from Fig. 13c, the potential pits in Li^+ – (111) planes for both crystals created by electro neutral skeleton $W_0(x)$ potentials, are very shallow. The account of the potentials $W_\pm(x)$ represented in Fig. 13d leads to a sharp increase of the depths of these potential pits. This is just the essence of positron-like orientation motion of negatively charged particles in such charged planes: in the regions with the reduced electron and nucleus densities quite strong interaction potentials arise.

Conclusion. At the investigation of relativistic electron channeling in charged $(2m + 1, 2n + 1, 2p + 1)$ planes of ionic LiH and LiD crystals it has been shown that potential pits inversion into potential barriers is possible as in the case of crystal temperature increase (the inversion occurs in H^- (111) planes, beginning with $\mathrm{T} = 600\ \mathrm{K}$), and in the case of the transition to more high indices planes (for LiH crystal – these are (311) planes, and for LiD crystal – these are (331)) planes. At the same time there were calculated transverse energy spectra of relativistic electron channeling motion at $\gamma = 106{,}7$ Lorentz-factor. The transitions occurred at this were compared with the experimental data given in [13]. During the detailed discussion we have shown that the given above explanation of spectrum formation mechanism is more substantiated than in [13]. On the basis of our analysis it was proposed to carry out experimental investigations on the study of radiation processes at the relativistic electron channeling with the same energy as in [13] along (311) planes, since in this case due to the existence of the potential pits of the same type the radiation spectra are more predicted.

The obtained results may be used for the optimization of some radiation processes. In particular, they may serve the basis for calculation apparatus at the elaboration and creation of high-effective rebuilding sources of a rigid quasi-monochromatic radiation of X-ray and gamma-ranges on the basis of the channeling of the relativistic electrons. Anomalously weak dissipation, braking and dechanneling of electrons at positron-like motion regime contribute to the narrowing of the radiation line and a sharp increase of its intensity.

By means of the expressions (8.1) ÷ (8.4) it is easy to show that the calculated potential pits in (100) and (110) planes are in a very close fit to the analogous potential pits represented in [13]. On the other side, at $\alpha = 0$ we also come to the similar result. First, all this ascertains that all our calculations are quite correct starting from the consideration of one-partial potentials and finishing with the averaging by planes and by thermal oscillations. Second, contributions into planar potentials (100) and (110) at $\alpha \neq 0$ of interaction potentials originating of non-compensated ion charges are also zero since the amplitudes of thermal oscillations of various ions are different.

The existence of such electron motion peculiarities may contribute to solution of the problem on the creation of gamma-laser on the basis of mono-energetic beam of relativistic electrons based on one of the schemes considered in [5].

1. *Бабаджанян Н.Э* К теории каналирования в кристалле LiH // ЖТФ. – 2006. – 76. вып. 3. 2. *Базылев В.А., Жеваго Н.К.* Излучение быстрых частиц в веществе и во внешних полях. – М.: Наука, 1987. 3. *Бейтмен Г., Эрдейн А.* Высшие трансцендентные функции. – М.: Наука, 1974. 4. *Бете Г., Солпитер Э.* Квантовая механика атомов с одним и двумя электронами. – М.: Физмагиз, 1960. 5. *Высоцкий В.И., Кузьмин Р.Н.* Гамма-лазеры. – М.: Изд.МГУ, 1989. 6. *Высоцкий В.И., Кузьмин Р.Н., Максюта Н.В.* О возможности аномального каналирования электронов в ионных кристаллах // Тез. докл. XVI всесоюз. совещ. по физике взаимод. заряж. частиц с кристаллами. – М.: Изд. МГУ, 1986. 7. *Высоцкий В.И., Кузьмин Р.Н., Максюта Н.В.* Особенности ориентационного движения заряженных частиц в (111) плоскостях кристалла LiH // Материалы VIII Всесоюзной конференции "Взаимодействие атомных частиц с твердым телом". – М.: Изд-во МИФИ, 1987. 2. 8. *Высоцкий В.И., Кузьмин Р.Н., Максюта Н.В.* Аномальное каналирование и квазихарактеристическое излучение нерелятивистских электронов в ионных кристаллах // ЖЭТФ. – 1987. 93, вып. 6(12). 9. *Готт Ю.В.* Взаимодействие частиц с веществом в плазменных исследованиях. – М.: Атомиздат, 1978. 10. *Корхмазян Н.А., Корхмазян Н.Н., Бабаджанян Н.Э.* Потенциал плоскостного каналирования в поверхностном слое кристалла LiH // ЖТФ. – 2004. – 74. вып. 12. 11. *Корхмазян Н.А., Корхмазян Н.Н., Бабаджанян Н.Э.* Эффективный потенциал плоскостного каналирования в кристалле LiH // ЖТФ. – 2003. –.73. вып. 8. 12. *Смирнов Б.М.* Отрицательные ионы. – М.: Атомиздат, 1978. 13. *Berman B.L., Kephart J.O., Datz S. et al.* Channeling radiation from LiH and LiD // Nucl. Instr. and Meth. in Phys. Res. B. – 1996. – 119.

Submitted on 28.12.11

UDC 539.12

M. Maksyuta, Ph. D., V. Vysotskii, Dr. Sci.

THE PECULARITIES OF THE CHANNELING AND QUASICHARACTERISTIC RADIATION OF RELATIVISTIC ELECTRONS IN CHARGED CRYSTALLOGRAPHIC PLANES OF LiF IONIC CRYSTAL

У роботі проводиться дослідження процесу каналювання релятивістських електронів у заряджених площинах іонного кристалу LiF, зокрема показується, що при переході в цьому кристалі до високоіндексних кристалографічних площин відбуваються інверсії потенціальних ям у потенціальні бар'єри. Досліджується також вплив температурного фактора на структури потенціалів взаємодії релятивістських електронів з такими високоіндексними зарядженими площинами. У випадку заряджених площин (111) проводиться аналітичний розрахунок енергетичних рівнів і спектральних інтенсивностей, а на їх основі здійснюється ідентифікація спектральних ліній з експериментально існуючими спектрами випромінювання. Робиться акцент на позитроноподібність орієнтаційного руху електронів в заряджених кристалографічних площинах.

Ключові слова: каналювання релятивістських електронів, високоіндексні кристалографічні площини, іонні кристали, спектральна інтенсивність, позитроноподібність

The paper deals with the investigation of the channeling process of relativistic electrons in charged planes of LiF ionic crystal, besides it is shown that at the transition to high-indices crystallographic planes in this crystal the inversions of potential pits into potential barriers occurs. It is also investigated the influence of temperature factor on the structures of interaction potentials of relativistic electrons with such high indices charged planes. In the case of the charged planes (111) the analytic calculation of energy levels and spectral intensities is made and the identification of spectral lines to experimentally existing spectral radiations is carried out on their basis.

Keywords: relativistic electron channeling, high indices crystallographic planes, ionic crystals, spectral intensity, positron-likeness

Introduction. For the creation of the effective sources of a short-wave radiation in [5] it was proposed to perform the orientation motion of electrons in charged (111) planes of ionic crystals with the structure of NaCl type. In particular as it was mentioned in [14] for this purpose ionic LiF crystal is quite a good sample. Anomalous great dechanneling lengths are possible in it in charged planes constructed of Li^+ ions even in the case of slight relativistic electron channeling. The cause of this anomalous appearance deals with the increase of the potential pits depths in such charged planes at the expense of Coulomb components. If we calculate potential pits in such planes not accounting Coulomb components but taking into account electroneutral skeletons only (we mean the superposition of a strong localized positive charge of Li^+ nuclei ions and special smeared of these ions electron negative charge) potential pits depths will be considerably smaller. More detailed information concerning the fact will be given in the conclusion. Thus, in LiF crystal could be realized the situation when both for the first sight mutual self-exceptional factors may coexist: the presence of low electron and nucleus densities in the channeling particles domains and high binding-energies of the channeling particles with crystals. It is evident that similar motion regime could be used, for example, for the optimization of radiation sources on the basis of the channeling of both ultra-relativistic and slight relativistic electrons.

Proceeding from it the given paper gives a detailed analytic calculation of the interaction potentials of the charged particles with the charged (111) – planes, it has been calculated the energies of the spectral lines occurring at relativistic electrons channeling with various Lorentz-factors and the functions of spectral intensities for all these cases have been found as well. Besides, the paper gives a comparative analysis with the empiric data given in [3].

Besides, the given paper shows that the charged particle orientation motion in high indices charged $(2m+1, 2n+1, 2p+1)$ planes of crystal LiF (here m, n, p – non-negative natural numbers) possesses additional anomalous properties: in Li^+ – planes instead of the potential pits the potential barriers may occur, i.e. positron-like regime for electrons is realized concerning these inverted potentials (in particular, the influence of temperature factor is investigated).

Just if in LiF crystal the positive charged particles channeling is considered the electron-like motion regime may occur when particles trajectories will cross Li$^+$ – planes. This effect, in particular, can be used for the optimization of nucleus synthesis systems on the basis of particle beams of the same type correlating in a certain way with orientated crystal targets containing nuclei of different type.

The calculation of interaction potentials of relativistic electrons with the charges high-indices planes of LiF ionic crystal. Calculating the interaction potentials of the charged particles with arbitrary charged crystallographic $(2m+1,2n+1,2p+1)$ planes of LiF crystal it is necessary to proceed from one-partial electrostatic potentials for Li$^+$ and F$^-$ ions. These potentials could be found by means of $\Delta\varphi(r)=-4\pi\rho(r)$ Poisson equations or at the utilization of $\oint_S \vec{E}(r)d\vec{S}=(4\pi)^2\int_0^r \xi^2\rho(\xi)d\xi$ Ostrogradsky-Gauss theorem. At this to find $\rho(r)$ densities in the case of Li$^+$ ions the wave function $\psi_1(r)=\sqrt{Z^*/\pi a_0}\exp\left(-Z^* r/a_0\right)$ is used for 1*s*-electrons (localized nearby lithium nucleus) [3], and for 2*s*-electron (partially localized nearby lithium nucleus) the wave function $\psi_2(r)=\left(2\lambda_2^6 r/15\pi a_0^6\right)^{1/2}\exp(-\lambda_2 r/a_0)$ is used where $\lambda_2 \approx 0,797$ [6]. One-partial Li$^+$ ion potential got in such a way is written down in the following form:

$$\varphi_+(r)=e\left\{2\left(\frac{Z^*}{a_0}+\frac{1}{r}\right)\exp\left(-\frac{2Z^*}{a_0}r\right)+\frac{2\lambda_2^4(1-\alpha)}{15a_0^4}\left(r^3+\frac{4a_0}{\lambda_2}r^2+\frac{9a_0^2}{\lambda_2^2}r+\frac{12a_0^3}{\lambda_2^3}+\frac{15a_0^4}{2\lambda_2^4 r}\right)\exp\left(-\frac{r}{a_0}\right)+\frac{\alpha}{r}\right\}, \qquad (1)$$

where a_0 – Bohr radius; $Z^*=Z_{\text{Li}}-\beta=43/16$ – screened nuclei charge of Li$^+$; $\beta=5/16$ – screening parameter corresponding to Li$^+$ nucleus and calculated by means of a variation method taking into account the fact that every of 1s – electrons partially screens Li$^+$ ion nucleus from another electron; α – degree of binding ionicity, which determines the probability of electron presence (belonging to Li atoms) nearby F atoms. The contribution of the third electron of Li$^+$ ion we calculate accounting its $1-\alpha$ probability to be found in the field of a screened lithium nucleus (it explains $1-\alpha$ multiplier presence in the second component in (1)) formula and with α probability in the field of fluorine nucleus. It will explain the presence of α multiplier for one-partial potential of F$^-$ ion in the formula we are going to obtain.

For F$^-$ ions it is necessary to get one-partial potential proceeding from the principle of superposition. So let's suppose that one-partial potential for F$^-$ ion is represented as two components. The first component describes fluorine atom for which we choose one-partial potential in the form of the following Coulomb screened potential:

$$\varphi_F(r)=\frac{Z_F e}{r}\exp\left(-\frac{r}{b_F}\right), \qquad (2)$$

where $b_{\text{F}} \approx 0,8853 a_0 Z_{\text{F}}^{-1/3}$ – fluorine atom screening radius, $Z_{\text{F}}=9$ – fluorine atom nucleus charge. The second component will describe the contribution of additional effective electron (effective as an abundant charge nearby F atom in LiF ionic crystal is created not by one electron but all the valence electrons of six neighboring Li atoms) which is found with α probability ($\alpha \approx 0,915$ – ionicity degree of LiF crystal [13]) nearby F atom in the state of [11]

$$\psi(r,\theta)=\frac{r}{\sqrt{\pi}}\sum_{i=1}^{4} a_i\zeta_i^{5/2}\exp(-\zeta_i r)\cos\theta, \qquad (3)$$

where numerical values of a_i and ζ_i parameters are taken from the reference book [10] and are given below in the Table 1.

Having integrated a square module of a wave function (3) by some spherical angles of φ and θ let's come to the following expression for a radial density of valence electron distribution as to F$^-$ ion nucleus:

$$\rho(r)=-\frac{4er^2}{3}\sum_{i=1}^{10} b_i\exp(-\eta_i r), \qquad (4)$$

where $b_i=a_i^2\zeta_i^5$, $\eta_i=2\zeta_i$, $i=1,\ldots,4$; $b_5=2a_1a_2(\zeta_1\zeta_2)^{5/2}$, $\eta_5=\zeta_1+\zeta_2$; $b_6=2a_1a_3(\zeta_1\zeta_3)^{5/2}$, $\eta_6=\zeta_1+\zeta_3$; $b_7=2a_1a_4(\zeta_1\zeta_4)^{5/2}$, $\eta_7=\zeta_1+\zeta_4$; $b_8=2a_2a_3(\zeta_2\zeta_3)^{5/2}$, $\eta_8=\zeta_2+\zeta_3$; $b_9=2a_2a_4(\zeta_2\zeta_4)^{5/2}$, $\eta_9=\zeta_2+\zeta_3$; $b_{10}=2a_3a_4(\zeta_3\zeta_4)^{5/2}$, $\eta_{10}=\zeta_3+\zeta_4$. Using Ostrogradsky-Gauss theorem and the formula (4) we get electrostatic potential of ion F$^-$ valence electron

$$\phi_-(r)=e\left[\frac{4}{3r}\sum_{i=1}^{10} b_i\left(\frac{r^3}{\eta_i^2}+\frac{6r^2}{\eta_i^3}+\frac{18r}{\eta_i^4}+\frac{24}{\eta_i^5}\right)\exp(-\eta_i r)-\frac{1}{r}\right]. \qquad (5)$$

Table 1

Numerical meanings of a_i and ζ_i, parameters used in wave function describing the valence electron in F$^-$ ion

	a_i	ζ_i
1	0,247	0,9568
2	0,099	1,466
3	0,470	2,075
4	0,308	3,933

At last, multiplying the potential (5) by α and then adding it to the potential (2), we get one-particle potential $\varphi_-(r)=\phi_-(r)+\varphi_{\text{F}}(r)$ of F$^-$ ion.

$$\varphi_-(r)=\varphi_F(r)+\phi_-(r)=\frac{e}{r}\left\{Z_F\exp\left(-\frac{r}{b_F}\right)+\alpha\left[\frac{4}{3}\sum_{i=1}^{10} b_i\left(\frac{r^3}{\eta_i^2}+\frac{6r^2}{\eta_i^3}+\frac{18r}{\eta_i^4}+\frac{24}{\eta_i^5}\right)\exp(-\eta_i r)-\frac{1}{r}\right]\right\}. \qquad (6)$$

It is evident that this potential satisfies the following boundary condition: $\lim\limits_{r\to\infty}\varphi_-(r)=-\alpha e/r$.

Thus, from the formulas (1) and (6) it is evident that electrostatic potentials of Li$^+$ and F$^-$ ions are represented as a sum of components exponentially descendent and changing by Coulomb law. It means that the first components are originated by electro neutral skeleton of corresponding ions and the second ones arise as a consequence of non-compensated positive or negative charges that in definite directions lead to the origination of the charged axis or charged planes. On the basis of the following standard procedure of the averaging by the planes:

$$V(x)=\frac{2\pi Q}{S}\int_0^\infty \rho\varphi\left(r=\sqrt{\rho^2+x^2}\right)d\rho, \qquad (7)$$

where S – a square of two-dimensional elementary cell in the channeling planes (see, for example, [1]) with the usage of the formulas (1) and (6) instead of the potential $\varphi(r)$ in (7) we get the following expression for the potential of the charged particles of Q (further $Q=-e$, since we consider channelling of electrons) charges interaction with all "frozen" charged $(2m+1,2n+1,2p+1)$ planes built in turn of Li^+ and F^- ions:

$$V(x)=V_0\sum_{k=-\infty}^{\infty}\left\{\left(\left(|x-kd|+\frac{3}{\lambda_*}\right)\exp\left(-\lambda_*|x-kd|\right)+(1-\alpha)\exp\left(-\frac{2\lambda_2|x-kd|}{a_0}\right)\left[\frac{\lambda_2^3(x-kd)^4}{15a_0^3}+\frac{2\lambda_2^2|x-kd|^3}{5a_0^2}+\frac{6\lambda_2(x-kd)^2}{5a_0}+\right.\right.\right.$$
$$\left.+2|x-kd|+\frac{3a_0}{2\lambda_2}\right]+\frac{4\alpha}{3}\sum_{i=1}^{10}\frac{b_i}{\eta_i^3}\left(|x-kd-d/2|^3+\frac{9(x-kd-d/2)^2}{\eta_i}+\frac{36|x-kd-d/2|}{\eta_i^2}+\frac{60}{\eta_i^3}\right)\exp\left(-\eta_i|x-kd-d/2|\right)+$$
$$\left.+Z_F b\exp\left(-\frac{|x-kd-d/2|}{b_F}\right)-\alpha\left(|x-kd|-\frac{d}{4}\right)\cdot\chi\left(\frac{d}{2}-|x-kd|\right)\right\},\qquad(8)$$

where $V_0=-2\pi e^2/S$, $\chi(x)$ – a step-like Heaviside function, $\lambda_*=2Z^*/a_0$. In the conclusion of the paper we will stop in more detail in the obtaining of the last component in formula (8). In Fig. 1 the interaction potentials (3) are shown on one period at electron channeling, respectively, in charged "frozen" (111), (311) and (511) planes (in this and following figures the distances along abscissa axis correspond to dimensionless $\xi=x/d$ units, where $d=a\big/\sqrt{(2m+1)^2+(2n+1)^2+(2p+1)^2}$ – a distance between crystallographic planes of $(2m+1,2n+1,2p+1)$ including Li^+ and F^- ions, a – a crystal lattice period. More detailed consideration concerning the receiving of the last component in the formula (3) will be given in the conclusion of the paper).

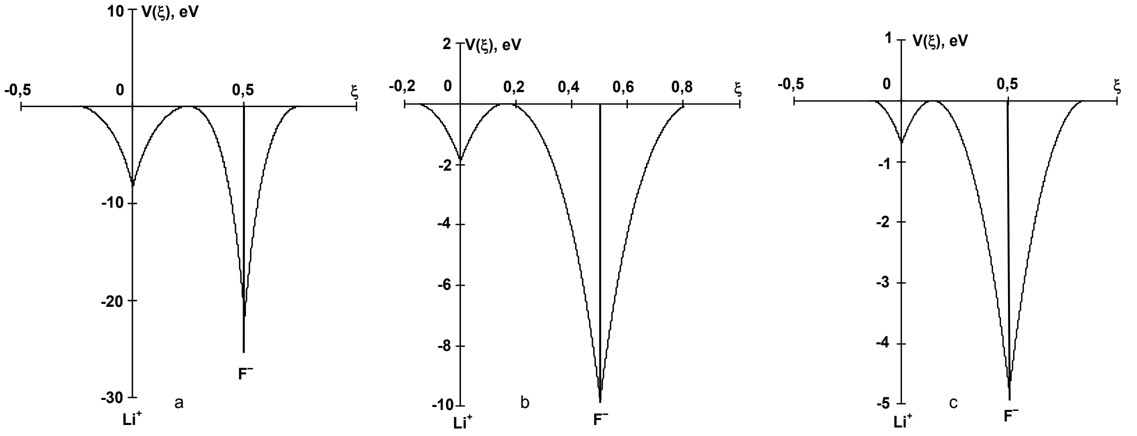

Fig. 1. Electron interaction potentials at their channeling in LiF crystal along charged "frozen" planes: (a) – (111), (b) – (311), (c) – (511)

As it is seen from Fig. 1, these potentials common character in spite of the essential changes of potential pits depth and also the distance between the charged planes at the transition to higher indices directions does not change: the potential pits are present both in Li^+ "frozen" planes and in F^- "frozen" planes. The potential (8) on these planes satisfies the following boundary conditions:

$$\left[\frac{\partial V(kd+0)}{\partial x}-\frac{\partial V(kd-0)}{\partial x}\right]=-\frac{4\pi e^2}{S}Z_{\text{Li}},$$
$$\left[\frac{\partial V(kd+d/2+0)}{\partial x}-\frac{\partial V(kd+d/2-0)}{\partial x}\right]=-\frac{4\pi e^2}{S}Z_{\text{F}}.\qquad(9)$$

Conditions (9) mean that nuclei distribution density on "frozen" planes has a singular character; i.e. is expressed as follows:

$$\rho(x)=\frac{e}{S}\sum_{k=-\infty}^{\infty}\left[Z_{\text{Li}}\,\delta(x-kd)+Z_{\text{F}}\,\delta(x-kd+d/2)\right],\qquad(10)$$

where $\delta(x)$ – Dirac delta-function.

Let's stop on the procedure of the potential (8) averaging by the thermal oscillations. By means of the function of the ions deviation from the equilibrium position

$$f(x)=\left(2\pi u^2\right)^{-1/2}\exp\left(-x^2/2u^2\right),\qquad(11)$$

where u – an average amplitude of thermal oscillations, the averaging by the thermal oscillations is represented as the following convolution [1]:

$$U(x)=\int_{-\infty}^{\infty}V(x-y)f(y)dy\,.\qquad(12)$$

To sum up after substitution of (8) and (11) into (12) we get the following averaging by the thermal oscillations potential of interaction with the totality of high-indices charged $(2m+1,2n+1,2p+1)$ planes of LiF crystal:

$$U(x)=\sum_{k=-\infty}^{\infty}\left[U_+^{(1)}(x-kd)+\frac{(1-\alpha)}{4}U_+^{(2)}(x-kd)+U_-(x-kd-d/2)+U_\pm(x-kd)\right]=W_0(x)+W_\pm(x),\qquad(13)$$

$$U_+^{(1)}(x) = -\frac{V_0}{2}\exp\left(\frac{\lambda_* u_+^2}{2}\right)\left\{\exp(-\lambda_* x)\left[P_1^{(+1)}(x)\,\mathrm{erfc}\,\tau_{+1}(x) + u_+\sqrt{\frac{2}{\pi}}\right]\exp\left[-\left(\tau_{+1}(x)^2\right)\right] - \right.$$

$$\left. -\exp(\lambda_* x)\left[P_1^{(+2)}(x)\,\mathrm{erfc}\,\tau_{+2}(x) - u_+\sqrt{\frac{2}{\pi}}\right]\exp\left[-\left(\tau_{+2}(x)^2\right)\right]\right\}, \qquad (13.1)$$

$$U_+^{(2)}(x) = -\frac{V_0}{2}\exp\left(\frac{\lambda_0^2 u_+^2}{2}\right)\left\{\exp(-\lambda_0 x)\left[P_4^{(+1)}(x)\,\mathrm{erfc}\,\kappa_{+1}(x) + P_3^{(+1)}(x)\sqrt{\frac{2}{\pi}}\exp\left[-\left(\kappa_{+1}(x)^2\right)\right]\right] + \right.$$

$$\left. +\exp(\lambda_0 x)\left[P_4^{(+2)}(x)\,\mathrm{erfc}\,\kappa_{+2}(x) + P_3^{(+2)}(x)\sqrt{\frac{2}{\pi}}\exp\left[-\left(\kappa_{+2}(x)^2\right)\right]\right]\right\}, \qquad (13.2)$$

$$U_-(x) = -\frac{V_0}{2}\left\{Z_F b_F \exp\left(\frac{u_-^2}{2b_F^2}\right)\left[\exp\left(-\frac{x}{b_F}\right)\mathrm{erfc}\,\tau_{b_F}^{(1)}(x) + \exp\left(\frac{x}{b_F}\right)\mathrm{erfc}\,\tau_{b_F}^{(2)}(x)\right] + \frac{4\alpha}{3}\sum_{i=1}^{10}\frac{b_i}{\eta_i^6}\exp\left(\frac{u_-^2\eta_i^2}{2}\right)\left[\exp(-\eta_i x)\left[P_{3i}^{(1)}(x)\cdot\right.\right.\right. \qquad (13.3)$$

$$\left.\left.\left.\cdot\,\mathrm{erfc}\,\tau_i^{(1)}(x) + u_-\eta_i\sqrt{\frac{2}{\pi}}\exp\left[-\left(\tau_i^{(1)}(x)\right)^2\right]P_{2i}^{(1)}(x)\right] - \exp(\eta_i x)\left[P_{3i}^{(2)}(x)\,\mathrm{erfc}\,\tau_i^{(1)}(x) - u_-\eta_i\sqrt{\frac{2}{\pi}}\exp\left[-\left(\tau_i^{(2)}(x)\right)^2\right]P_{2i}^{(2)}(x)\right]\right]\right\},$$

$$U_\pm(x) = \alpha V_0\left[x\,\mathrm{erf}\left(\frac{x}{u_+}\right) + u_+\sqrt{\frac{2}{\pi}}\exp\left[-\frac{x^2}{2u_+^2}\right] - (x-d/2)\,\mathrm{erf}\left(\frac{x-d/2}{u_-}\right) - u_-\sqrt{\frac{2}{\pi}}\exp\left[-\frac{(x-d/2)^2}{2u_-^2}\right]\right], \qquad (13.4)$$

where $P_1^{(+1,+2)}(x) = x \mp \frac{3}{\lambda_*} \pm \lambda_* u_+^2$,

$$P_3^{(+1,+2)}(x) = \pm\frac{\lambda_0^3}{60}x^3 + \frac{\lambda_0^2\left(4-\lambda_0^2u_+^2\right)}{20}x^2 \pm \frac{\lambda_0\left(3\lambda_0^4u_+^4 - 19\lambda_0^2u_+^2 + 72\right)}{60}x - \frac{\lambda_0^6u_+^6}{60} + \frac{7\lambda_0^4u_+^4}{60} - \frac{4\lambda_0^2u_+^2}{5} + 4,$$

$$P_4^{(+1,+2)}(x) = \frac{\lambda_0^3}{60}x^4 \mp \frac{\lambda_0^2\left(\lambda_0^2u_+^2 - 3\right)}{15}x^3 + \frac{\lambda_0\left(\lambda_0^4u_+^4 - 5\lambda_0^2u_+^2 + 12\right)}{10}x^2 \mp \frac{\left(\lambda_0^6u_+^6 - 6\lambda_0^4u_+^4 + 27\lambda_0^2u_+^2 - 60\right)}{15}x + \frac{\lambda_0^7u_+^8}{60} - \frac{\lambda_0^5u_+^6}{10} +$$

$$+\frac{13\lambda_0^3u_+^4}{20} - \frac{14\lambda_0u_+^2}{5} + \frac{6}{\lambda_0},\quad P_{2i}^{(1,2)}(x) = x^2\eta_i^2 \mp x\eta_i\left(2u_-^2\eta_i^2 - 9\right) + u_-^4\eta_i^4 - 7u_-^2\eta_i^2 + 36,\quad P_{3i}^{(1,2)}(x) = x^3\eta_i^3 \mp x^2\eta_i^2\left(3u_-^2\eta_i^2 - 9\right) +$$

$$+x\eta_i\left(3u_-^4\eta_i^4 - 15u_-^2\eta_i^2 + 36\right) \mp u_-^6\eta_i^6 \pm 6u_-^4\eta_i^4 \mp 25u_-^2\eta_i^2 \pm 60,\quad \tau_{+1,+2}(x) = \frac{1}{\sqrt{2}}\left(\lambda_* u_+ \mp \frac{x}{u_+}\right),\quad \kappa_{+1,+2}(x) = \frac{1}{\sqrt{2}}\left(\lambda_0 u_+ \mp \frac{x}{u_+}\right).$$

$$\tau_{b_F}^{(1,2)}(x) = \frac{1}{\sqrt{2}}\left(\frac{u_-}{b_F} \mp \frac{x}{u_-}\right), \qquad \tau_i^{(1,2)}(x) = \frac{1}{\sqrt{2}}\left(\eta_i u_- \mp \frac{x}{u_-}\right),$$

$\lambda_0 = 2\lambda_2/a_0$, $W_0(x)$ – the interaction potential originated by electro neutral skeletons of Li$^+$ and F$^-$ ions, $W_\pm(x)$ – interaction potential occurring as a result of non-compensated positive and negative charges of these ions (in the final part of this paper we'll return to these potentials analyzing them in detail). Here u_+ and u_- – the amplitudes of thermal oscillations of Li$^+$ and F$^-$ ions, respectively, which are calculated below accordingly with Debye theory (see, for example, [1]):

$$u_\pm = \hbar\left\{\frac{3}{m_\pm k_B T_D}\left[\frac{1}{4} + \left(\frac{T}{T_D}\right)^2\int_0^{T_D/T}\frac{\xi d\xi}{\exp\xi - 1}\right]\right\}^{1/2}, \qquad (14)$$

where $m_\pm$ – Li$^+$ and F$^-$ ion masses respectively, T_D – Debye temperature.

As the first example in Fig. 2 the interaction potentials (13) averaging by the thermal oscillations in Li$^+$ (111) and F$^-$ (111) planes have been built. Besides, these potentials were being calculated for three sets of thermal oscillation amplitudes. The first set of the thermal oscillation amplitudes of $u_+ \approx 0{,}117A$ and $u_- \approx 0{,}071A$ for Li$^+$ and F$^-$ ions respectively at $T = 300^\circ K$ was found by means of the formula (14) on the basis of the numerical meanings of $m_+ \approx 6{,}941 m_A$, $m_- \approx 18{,}998 m_A$, $T_D \approx 730$ K. Two other sets are taken from [14], i.e. we have $u_+ \approx 0{,}118A$, $u_- \approx 0{,}092A$ and $u_+ \approx 0{,}118A$, $u_- \approx 0{,}107A$. It is evident that only amplitudes u_- are different.

Visible changes of the depths of the potential pits in F$^-$ (111) planes only is seen from Fig. 2. It is just evident since in these sets only u_- amplitudes have a strong difference. Let's pay attention to quite a high sensitivity of the structure of (13) potential, for example, on the alternation of u_- amplitude (as it is seen from Fig. 2, u_- alternation in the range of $0{,}071A - 0{,}107A$ causes the decrease of the depths of the potential pits in F$^-$ (111) planes from ~16 eV up to ~14 eV). In their turn QCR spectra the detailed consideration of which we are starting now will be sensitive to similar alternations as well.

The investigation of the radiation transitions and QCR spectra at relativistic electron channeling in charged crystallographic planes of LiF crystal. Let's proceed to the analysis of the arisen radiation transitions in the potential pits represented in Fig. 2a, b. For this it is necessary to write down the solution of the following one-dimensional stationary Schrödinger equation with the relativistic mass of $m\gamma$ (m – electron rest mass):

$$\left[-\frac{\hbar^2}{2m\gamma}\frac{d^2}{dx^2} + U(x)\right]\psi(x) = \varepsilon\psi(x), \qquad (15)$$

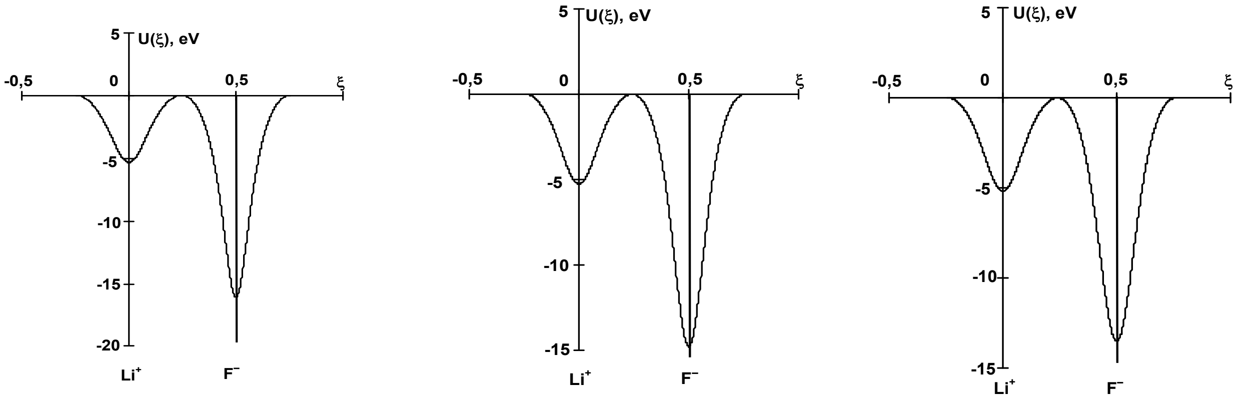

a b c

Fig. 2. Electron interaction potentials averaged by the thermal oscillations at their channeling in LiF crystal along the charged Li$^+$ (111) and F$^-$ (111) planes respectively with the utilization of (a) – the first, (b) – the second and (c)– third sets of amplitudes of the thermal oscillations u_+ и u_-

in which for the potential $U(x)$ energy, as it is usually done in the case of planar channeling (see, for example, [2]), we choose the following Pashle-Telller approximation:

$$U(x) = -U_0\,\mathrm{ch}^{-2}\left(\frac{x}{b}\right). \qquad (16)$$

After the substitution of (16) into (15) we get the energy level spectra of the transverse motion

$$\varepsilon_n = -\frac{\hbar^2}{2m\gamma b^2}(s-n)^2, \quad n = 0,1,...,[s], \qquad (17)$$

where $s = \left(2m\gamma U_0 b^2/\hbar^2 + 1/4\right)^{1/2} - 1/2$, $[s]$ – the integer part of *s* number, and also their corresponding proper wave functions

$$\psi_n(x) = \frac{\Gamma(2s-2n+1)}{2\Gamma(s-n+1)}\left[\frac{n!(s-n)}{b\Gamma(2s-n+1)}\right]^{1/2}\left(\mathrm{ch}\frac{x}{b}\right)^{n-s}\cdot C_n^{s-n+1/2}\left(\mathrm{th}\frac{x}{b}\right), \qquad (18)$$

where $\Gamma(x)$ – a Gamma-function, $C_n^{\lambda}(x)$ – a Gegenbauer polynomial [2]. At this the energies of radiation transitions are calculated by means of the formula

$$\hbar\omega_{mn} = 2\gamma^2(\varepsilon_m - \varepsilon_n). \qquad (19)$$

The following step deals with the comparison of the position of QCR spectral lines calculated in the paper for three given above sets of the thermal oscillation amplitudes with the results of the experiments. For example, let's take advantage of the experimental data on the radiation of the channeling relativistic electrons in (111) planes of LiF crystal given in [14]. For this let's approximate the potential pits in Fig. 2a, b, c with the utilization of the functions (16) and find U_0 and b parameters. In particular, in the case of the first set of amplitudes $u_\pm$ for the potential pits in Li$^+$ (111) planes we have the parameters of $U_0' \approx 5{,}33\,\mathrm{eV}$, $b' \approx 0{,}24A$, and in F$^-$ (111) planes we get the following values: $U_0 \approx 16{,}13\,\mathrm{eV}$ and $b \approx 0{,}21A$, in the case of the second set in the first planes we have $U_0' \approx 5{,}26\,\mathrm{eV}$, $b' \approx 0{,}24A$, and in the second ones – $U_0 \approx 14{,}78\,\mathrm{eV}$ and $b \approx 0{,}21A$. At last in the case of the third set we get such meanings: $U_0' \approx 5{,}18\,\mathrm{eV}$, $b' \approx 0{,}24A$ and $U_0 \approx 13{,}89\,\mathrm{eV}$, $b \approx 0{,}21A$. On the basis of these parameters by means of the formula (17) we calculate numerical values of the transverse energy levels at the energy of the channeling electrons equals to $E = 54{,}2\,\mathrm{MeV}$ which corresponds to the conditions of [19]. Let's enumerate these data in turn for all the three cases. In the first case in Li$^+$ planes we get $s' \approx 2{,}48$, $\varepsilon_{0'} \approx -3{,}80\,\mathrm{eV}$, $\varepsilon_{1'} \approx -1{,}35\,\mathrm{eV}$, $\varepsilon_{2'} \approx -0{,}14\,\mathrm{eV}$, and in F$^-$ planes – $s \approx 4$, $\varepsilon_0 \approx -12{,}9\,\mathrm{eV}$, $\varepsilon_1 \approx -7{,}26\,\mathrm{eV}$, $\varepsilon_2 \approx -3{,}23\,\mathrm{eV}$, $\varepsilon_3 \approx -0{,}81\,\mathrm{eV}$. In the second case Li$^+$ planes we get $s' \approx 2{,}46$, $\varepsilon_{0'} \approx -3{,}72\,\mathrm{eV}$, $\varepsilon_{1'} \approx -1{,}31\,\mathrm{eV}$, $\varepsilon_{2'} \approx -0.13\,\mathrm{eV}$, and in F$^-$ planes – $s \approx 3{,}81$, $\varepsilon_0 \approx -11{,}7\,\mathrm{eV}$, $\varepsilon_1 \approx -6{,}36\,\mathrm{eV}$, $\varepsilon_2 \approx -2{,}64\,\mathrm{eV}$, $\varepsilon_3 \approx -0{,}53\,\mathrm{eV}$. $s \approx 3{,}61$, $\varepsilon_0 \approx -11{,}57\,\mathrm{eV}$, $\varepsilon_1 \approx -6{,}05\,\mathrm{eV}$, $\varepsilon_2 \approx -2{,}30\,\mathrm{eV}$. In the third case in Li$^+$ planes we get $s' \approx 2{,}44$, $\varepsilon_{0'} \approx -3{,}67\,\mathrm{eV}$, $\varepsilon_{1'} \approx -1{,}28\,\mathrm{eV}$, $\varepsilon_{2'} \approx -0.12\,\mathrm{eV}$, and in F$^-$ planes – $s \approx 3{,}68$, $\varepsilon_0 \approx -10{,}92\,\mathrm{eV}$, $\varepsilon_1 \approx -5{,}79\,\mathrm{eV}$, $\varepsilon_2 \approx -2{,}28\,\mathrm{eV}$, $\varepsilon_3 \approx -0{,}37\,\mathrm{eV}$. Numerical values of all the most intensive spectral lines (the calculation is made in accordance with the formula (19)) for direct and tunnel transitions are shown in Table 2.

In Fig. 3a the potentials of interaction averaged by the thermal oscillations are shown (and the systems of transverse energetic levels in them) only with the utilization of the third set of amplitudes since as it is seen from the third column of the Table 2 and the Fig. 3b, quite a good agreement between the calculated for this case spectral lines is observed (the positions of these lines are marked by the vertical arrows) and experimentally given in [14] picks of intensity occurring at the channeling of relativistic electrons with $E = 54{,}2\,\mathrm{MeV}$ energy in the charged (111) planes of LiF crystal.

Table 2.

The numerical meanings of spectral lines occurring in the averaged by the thermal oscillations (three sets of amplitudes are used) potential pits of the charged (111) planes of LiF crystal at the channeling of electrons with Lorentz factor γ = 107,1

Transition	1	2	3
$1 \to 0$	134,2	126,8	119,6
$2 \to 1$	93,4	86,0	78,8
$3 \to 2$	52,6	45,2	38,0
$1' \to 0'$	54,9	54,4	53,8
$3 \to 0'$	68,8	73,2	75,6

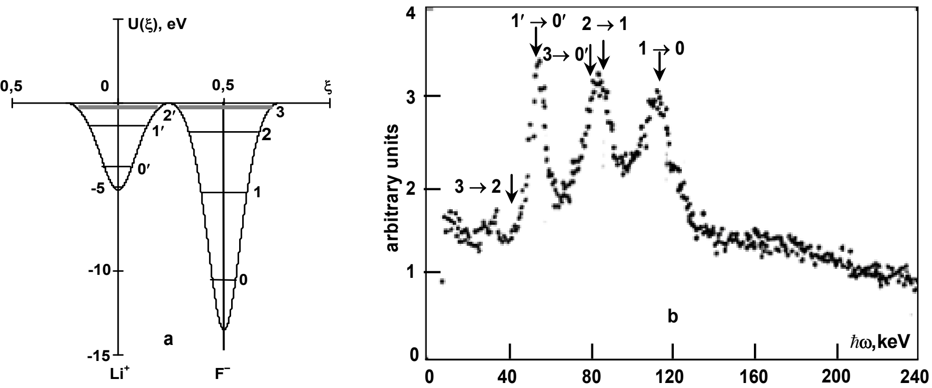

Fig. 3. (a) – the interaction potential and the transverse energy level system of the transverse energy ε_n, occurring at the channeling of electrons with the longitudinal energy *E* = 54,2 MeV in crystallographic (111) planes in LiF crystal at T = 300 K: (b) the measured radiation spectrum arising at the channeling of such electrons along (111) planes in LiF crystal taken in [14] (the arrows illustrate the identification of spectral lines with the arising radiation transitions)

However, note that in the calculations carried out in [14] not all the experimentally observed picks of the intensity of the radiation are compared with the transitions between the levels of the channeling motion, since the number of transitions given in [14] is insufficient for this purpose. Besides, some of the radiation transitions predicted in [14] don't coincide with our ones. The reason for this is evidently connected with some structural differences of the interaction potentials which as it is stated in [14] are got empirically with the utilization of so-called factors of electronic dissipation for the isolated Li^+ and F^- ions. In [14] the calculation of the interaction potentials for the channeling electrons in (111) planes is almost the same as in the calculations in the electro-neutral (100) and (110) planes, i.e. the situation is as if crystallographic (111) planes consist as well of electro-neutral Li and F atoms. In reality, as it stated above, (111) planes are charged as they are built of positively and negatively Li^+ charged and F ions. As proceeds, it is evident that the calculation of planar interaction potentials should be done using the correct one-particle interaction potentials of (1), (6) type and don't use the ones "standard" (and unutilized in this case) potentials of electro-neutral atoms.

Proceeding from the above mentioned, there should be expected some non-coincidences between the systems of transverse energy levels calculated in the given paper (and hence the transitions arising between them) and the ones given in [14]. Really, the formation of the spectral line of quasi-characteristic radiation with $\sim 55\,\text{keV}$ energy we explain by $1' \to 0'$ transition and in [14] by means of two $3 \to 2$ and $1' \to 0'$ transitions ($3 \to 2$ transition as it is seen from Fig. 3b, is connected with the radiation of the energy of $\sim 40\,\text{keV}$), the formation of the spectral line of the radiation with $\sim 80\,\text{keV}$ energy unlike in [14] we connect not only with $2 \to 1$ transitions but with $3 \to 0'$ tunnel transitions as well (see Fig. 3b). We observe a close fit only with the respect of photon radiation with $\sim 120\,\text{keV}$ energy.

To be more convinced in our calculations regularity and to find out the contribution of all the radiation transitions into a total picture let's carry out an analytic calculation of QCR spectral intensity in dipole approximation in accordance with the following formula (see [1]):

$$\frac{dI}{d\omega} = \frac{e^2\omega}{c^3}\left\{\sum_{i'=1}^{2} x_{i',i'-1}^2 \Omega_{i',i'-1}^2 f\left(\frac{\omega}{2\gamma^2\Omega_{i',i'-1}}\right)\left\langle P_{i'}(\vartheta)\right\rangle + \sum_{i=1}^{3} x_{i,i-1}^2 \Omega_{i,i-1}^2 f\left(\frac{\omega}{2\gamma^2\Omega_{i,i-1}}\right)\left\langle P_i(\vartheta)\right\rangle + \left\langle P_3(\vartheta)\right\rangle x_{3,0'}^2 \Omega_{3,0'}^2 f\left(\frac{\omega}{2\gamma^2\Omega_{3,0'}}\right)\right\}, \quad (20)$$

where $f(x) = \left(1 - 2x + 2x^2\right)\chi(1-x)$, $\Omega_{i',i'-1} = \dfrac{\hbar\left[2(s'-i')+1\right]}{2m\gamma b^2}$,

$\Omega_{i,i-1} = \dfrac{\hbar\left[2(s-i)+1\right]}{2m\gamma b^2}$ – the frequencies of the direct transitions between the neighboring energy levels of $i', i'-1$ and $i, i-1$ respectively in Li^+ – pit and F^- – pit, $\Omega_{3,0'} = \dfrac{\hbar}{2m\gamma}\left[\dfrac{s'^2}{b'^2} - \dfrac{(s-3)^2}{b^2}\right]$ – the frequency of the tunnel transition between the energy level 3 in F^- – pit and the energy level $0'$ in Li^+ – pit, $\left\langle P_{i'}(\vartheta)\right\rangle$ and $\left\langle P_i(\vartheta)\right\rangle$ – the averaging capture probabilities of the channeling particles respectively on the levels $\varepsilon_{n'}$ (n' = 1, 2) and ε_n (n = 1, 2, 3) in a planar channel (111) of LiF crystal, $\vartheta \approx p_x/mc\gamma$ – angle of the particle incidence in a crystal, $x_{i',i'-1}$, $x_{i,i-1}$ – matrix elements of dipole transitions between the neighboring energy levels in the case of a direct radiation transitions respectively in Li^+ – pit and F^- – pit, $x_{3,0'}$ – matrix element of the tunnel transition between the energy level 3 in F^- – pit and energy level $0'$ in Li^+ – pit.

At this the probability $\left\langle P_n(\vartheta)\right\rangle$ is found as follows. First we calculate the amount $P_n(\vartheta)$ supposing that the state of the transverse motion of the particle to the crystal is described by the plane wave $\psi(x) = (d)^{-1/2}\exp(ip_x x/\hbar)$, i.e. in correspondence with the theory of sudden perturbations we get [1]:

$$P_n(\vartheta) = \frac{1}{d}\left|\int_{-d/2}^{d/2} \exp\left(\frac{im\gamma\vartheta x}{\hbar}\right)\psi_n(x)\,dx\right|^2. \quad (21)$$

Then let's carry out in the following way the averaging of the probabilities capture of the channeling particles $P_n(\vartheta)$ by means of the function of normal distribution of $g(\vartheta) = \left(2\pi\vartheta_0^2\right)^{1/2}\exp\left(-\vartheta^2/2\vartheta_0^2\right)$ (here ϑ_0 – an angular dispersion):

$$\left\langle P_n(\vartheta)\right\rangle = \int_{-\infty}^{\infty} P_n(\vartheta - \vartheta')\,g(\vartheta')\,d\vartheta'. \quad (22)$$

Matrix elements of dipole direct transitions $x_{m,m-1}$ are found in correspondence with the following formula [1]:

$$x_{m,m-1}=\frac{b(m-1)!}{2\Gamma(2s-m+1)}\left[\frac{m(s-m)(s-m+1)}{2s-m+1}\right]^{1/2}\sum_{l=0}^{m}\sum_{k=0}^{m-1}\frac{(-1)^{k+l}\,\Gamma(2s+k-m+2)\Gamma(2s-m+l+1)}{2^{k+l}k!l!(m-l)!(m-k-1)!\Gamma(s+l-m+1)\Gamma(s+k-m+2)}\cdot$$

$$\cdot\sum_{p=0}^{k+l}\frac{(-1)^{p}(k+l)!}{(k+l-p)!\Gamma(2s-2m+p+1)}\sum_{r=0}^{p}\frac{(-1)^{r}}{r!(p-r)!}\sum_{i=0}^{\infty}\frac{(-1)^{i}\,\Gamma(2s-2m+p+i+1)}{i!(r+s+i-m+1/2)^{2}}. \qquad (23)$$

Just the matrix element of the dipole tunnel transition $x_{3,0'}$ is calculated in correspondence with the following expression:

$$x_{3,0'}=\int_{-\infty}^{+\infty}\psi_{0'}(x)x\psi_{3}(x-d/2)dx. \qquad (24)$$

Thus, using the formula (18) for the wave functions $\psi_n(x)$ we calculate by means of the formulas (21) and (22) the averaging probabilities of the captures of $\langle P_n(\vartheta)\rangle$, then using the formulas (23) and (24) we find all the necessary matrix elements $x_{m',m'-1}$, $x_{m,m-1}$, $x_{3,0'}$, and at last by the formula (20) we calculate the dependencies of relative spectral densities of QCR intensity $G(\omega)$, constructed below in Fig. 4a, b, c for three angles of incidence ϑ (note that the function of the intensity spectral density $dI/d\omega$ we standardize in a way to get an approximate coincidence of the calculated dependence in Fig. 4a with the radiation spectrum measured also at zero incident angle represented in Fig. 3b).

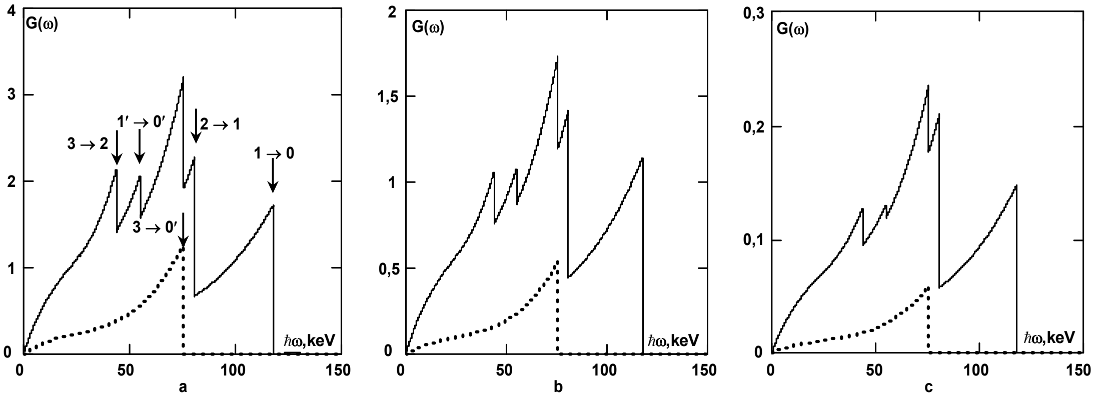

Fig. 4. The spectral density of QCR intensity calculated in relative units in a dipole approximation and occurring as a result of relativistic electron channeling (with a longitudinal *E* = 54,2 MeV energy and an angular dispersion $\vartheta_0 \approx$ 0,3 mrad) along crystallographic (111) planes of LiF crystal in the cases of the following incident angles: (a) – ϑ = 0 mrad, (b) – ϑ = 0,5 mrad, (c)

As it is seen from Fig. 4a, where an identification of spectral lines with possible transitions is made a satisfactory fit with a measured spectrum is observed (a little differences in the magnitudes of main picks of the calculated spectrum are evidently due to dipole approximation utilization and non-accounting of the alternations of the populations of the transverse energy levels in the process of electron channeling. Note that in [12] there is also a radiation spectrum calculated in a dipole approximation for electrons with $\gamma = 107$ Lorentz-factor. It is essentially different of the measured spectrum in Fig. 3b, and the one we calculated in Fig. 4a, since the intensity of the first spectral line appeared to be the biggest one (may be it deals with errors in the calculations since even the formula (10) in [12] has written with an error).

From Fig. 4b, c it is evident that spectral intensity at the incident angle alternation (we have chosen the incident angles of ϑ = 0,5 mrad and ϑ = 1 mrad) falls approximately according to the law as shown in Fig. 7 in [14].

The paper has also calculated the systems of energy levels in Li^{+} (111) planes and in F^{-} (111) planes at Lorentz-factors of $\gamma = 60{,}7$ and $\gamma = 34$. In particular, at $\gamma = 60{,}7$ for the first set of amplitudes in Li^{+} planes we have $s' \approx 1{,}77$, $\varepsilon_{0'} \approx -3{,}4\,\text{eV}$, $\varepsilon_{1'} \approx -0{,}64\,\text{eV}$, and in F^{-} planes – $s \approx 2{,}9$, $\varepsilon_0 \approx -12\,\text{eV}$, $\varepsilon_1 \approx -5{,}16\,\text{eV}$, $\varepsilon_2 \approx -1{,}16\,\text{eV}$, for the second set of amplitudes in Li^{+} planes we have $s' \approx 1{,}75$, $\varepsilon_{0'} \approx -3{,}33\,\text{eV}$, $\varepsilon_{1'} \approx -0{,}61\,\text{eV}$, and in F^{-} planes – $s \approx 2{,}76$, $\varepsilon_0 \approx -10{,}84\,\text{eV}$, $\varepsilon_1 \approx -4{,}41\,\text{eV}$, $\varepsilon_2 \approx -0{,}82\,\text{eV}$ and at last for the third set of amplitudes in Li^{+} planes we have $s' \approx 1{,}74$, $\varepsilon_{0'} \approx -3{,}29\,\text{eV}$, $\varepsilon_{1'} \approx -0{,}59\,\text{eV}$, and in F^{-} planes – $s \approx 2{,}66$, $\varepsilon_0 \approx -10{,}1\,\text{eV}$, $\varepsilon_1 \approx -3{,}94\,\text{eV}$, $\varepsilon_2 \approx -0{,}63\,\text{eV}$. Such a level presence leads to the appearance of three spectral lines of radiation in each of these three cases, numerical data for which are given in Table 3.

Table 3

Numerical meanings of the spectral lines occurring in the averaged by the thermal oscillations (three sets of the amplitudes are used) potential pits of the charged (111) planes of LiF crystal at the electrons channeling with γ = 60,7 Lorentz factor

Transition	1	2	3
$1 \to 0$	51,9	48,8	45,7
$2 \to 1$	28,8	25,6	22,6
$1' \to 0'$	20,1	19,9	21,1

Fig. 5a represents the averaged by the thermal oscillations interaction potentials in Li^{+} (111) and F^{-} (111) planes (and the systems of the transverse energy levels in them) with the utilization of the second set of the amplitudes since as it is seen from the second column of the Table 3 and the Fig. 5b, this case has the closest fit between the calculated spectral lines (the positions of these lines are marked by the vertical arrows) and the picks of the intensity experimentally given in [14] occurring at the relativistic electrons channeling with $E = 30{,}5\,\text{MeV}$ energy.

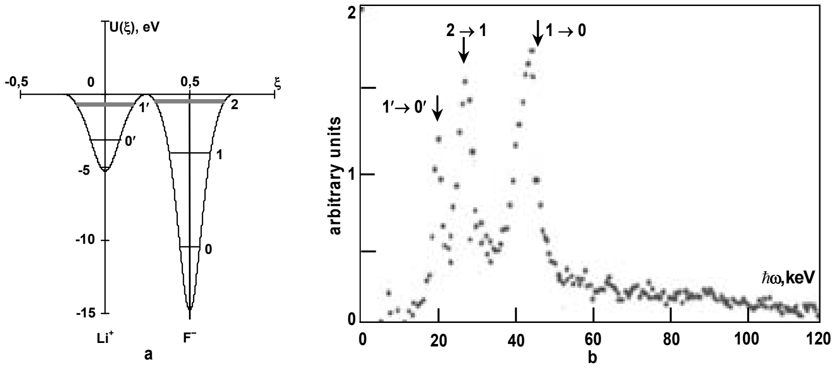

Fig. 5. (a) – the interaction potential and the transverse energy level system of the transverse energy ε_n, occurring at the channeling of electrons with the longitudinal energy *E* = 30,5 MeV in crystallographic (111) planes in LiF crystal at T = 300 K: (b) – the measured radiation spectrum arising at the channeling of such electrons along (111) planes in LiF crystal taken in [14] (the arrows illustrate the identification of spectral lines with the arising radiation transitions)

Note that for this energy of electrons almost a close fit between our calculations and the data in [14] is observed. There is only a little difference for $2 \to 1$ transition. The spectral line corresponding to it in our case has less energy than in [14] (however, as it is seen from Fig. 5b, it does not influence the accuracy of the identification with the experimental data).

There is almost a complete fit at this electron energy just between a radiation spectra namely between the measured spectrum in Fig. 5b and a calculated one in Fig. 6.

From Fig. 6 it is seen that in addition to $1 \to 0$, $2 \to 1$, $1' \to 0'$ direct transitions enumerated in Table 3, $2 \to 0'$, $1' \to 1$ and $1' \to 0$ tunnel transitions contribute definitely to a total spectral intensity splitting the second spectral line (a more complicated structure of the second line is also visible on the experimental dependence of Fig. 5b).

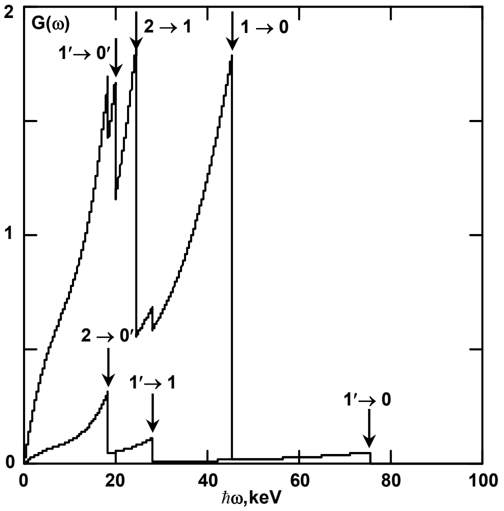

Fig. 6. The spectral density of QCR intensity calculated in relative units in a dipole approximation and occurring at relative electron beam channeling *E* = 30,5 MeV along (111) planes of LiF crystal (an electron beam has an angular dispersion of $\vartheta_0 \approx$ 0,15 mrad and an incident angle of ϑ = 0)

At $\gamma = 34$ for the first set of the amplitudes in Li$^+$ planes we have $s' \approx 1{,}23$, $\varepsilon_{0'} \approx -2{,}94\,\text{eV}$, $\varepsilon_{1'} \approx -0{,}1\,\text{eV}$, and in F$^-$ planes – $s \approx 2{,}07$, $\varepsilon_0 \approx -10{,}87\,\text{eV}$, $\varepsilon_1 \approx -2{,}9\,\text{eV}$, $\varepsilon_2 \approx -0{,}01\,\text{eV}$, for the second set of the amplitudes in Li$^+$ planes we have $s' \approx 1{,}22$, $\varepsilon_{0'} \approx -2{,}88\,\text{eV}$, $\varepsilon_{1'} \approx -0{,}09\,\text{eV}$, and in F$^-$ planes – $s \approx 1{,}96$, $\varepsilon_0 \approx -9{,}78\,\text{eV}$, $\varepsilon_1 \approx -2{,}35\,\text{eV}$ and at last, for the third set of the amplitudes in Li$^+$ planes we have $s \approx 1{,}21$, $\varepsilon_{0'} \approx -2{,}83\,\text{eV}$, $\varepsilon_{1'} \approx -0{,}08\,\text{eV}$, and in F$^-$ planes– $s \approx 1{,}89$, $\varepsilon_0 \approx -9{,}09\,\text{eV}$, $\varepsilon_1 \approx -2{,}02\,\text{eV}$.

Such levels led to the appearance of three spectral lines of radiation in the first case and two spectral lines in another two cases. The numerical data are presented below in Table 4 only for two spectral lines.

Table 4

Numerical meanings of the spectral lines occurring in the averaged by the thermal oscillations (three sets of the amplitudes are used) potential pits of the charged (111) planes of LiF crystal at the electrons channeling with γ = 34 Lorentz factor

Transition	1	2	3
$1 \to 0$	18,8	17,5	16,2
$1' \to 0'$	6,6	6,5	6,4

Comparing the numerical data for spectral lines represented in Table 4 and the experimental picks shown in Fig. 7b it is seen that the best fit at $E = 16{,}9\,\text{MeV}$ electron energy occurs when the averaging by the thermal oscillations of the interaction potentials with Li$^+$ (111) and F$^-$ (111) planes are carried out with $u_+ \approx 0{,}118A$, $u_- \approx 0{,}085A$ amplitude utilization which by the magnitudes are between the first and the second sets. For such amplitudes the potential pits in Li$^+$ (111) planes have the following parameters: $U_0' \approx 5{,}26\,\text{eV}$, $b' \approx 0{,}24A$, and in F$^-$ (111) planes: $U_0 \approx 15{,}2\,\text{eV}$ and $b \approx 0{,}21A$. Further in Li$^+$ planes we have $s' \approx 1{,}22$, $\varepsilon_{0'} \approx -2{,}89\,\text{eV}$, $\varepsilon_{1'} \approx -0{,}09\,\text{eV}$, and in F$^-$ planes – $s \approx 2$, $\varepsilon_0 \approx -10{,}13\,\text{eV}$, $\varepsilon_1 \approx -2{,}52\,\text{eV}$, which leads at $1 \to 0$ transition to the appearance of a spectral line with $\hbar\omega_{10} \approx 17{,}6\,\text{keV}$ energy and at $1' \to 0'$ transition to the spectral line with $\hbar\omega_{1'0'} \approx 6{,}5\,\text{keV}$ energy. Relative potential pits along with the system of energy levels in them are shown in Fig. 7a and the arrows in Fig. 7b indicate the arisen direct transitions.

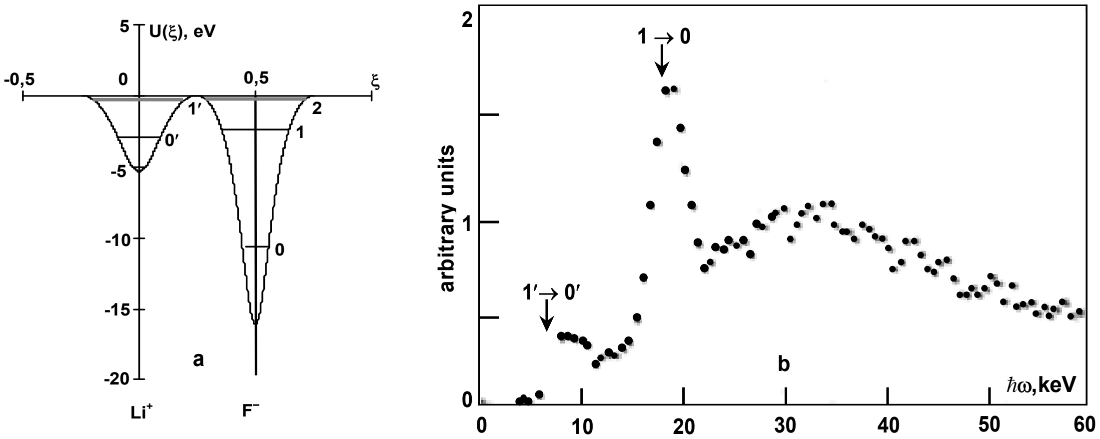

Fig. 7. (a) – the interaction potential and the transverse energy level system of the transverse energy ε_n, occurring at the channeling of electrons with the longitudinal energy *E* = 16,9 MeV in crystallographic (111) planes in LiF crystal at T = 300 K: (b) – the measured radiation spectrum arising at the channeling of such electrons along (111) planes in LiF crystal taken in [14] (the arrows illustrate the identification of spectral lines with the arising radiation transitions)

Note that in the list of the spectral lines in [14] there is only one line in the region of $\sim 17\,\text{keV}$ energies. Just our calculation led to the appearance of one more spectral line in the domain of $\sim 7\,\text{keV}$ energies. Besides, as it follows from the calculation of the spectral density of QCR intensity (see Fig. 8), there is two more weak picks connected with $1' \to 1$ and $1' \to 0$ tunnel transitions.

Evidently this numerous spectral data totality is a convincing confirmation of the calculation regularity of the interaction potential (13) with the charged (111) planes for LiF crystal.

Besides, to find the closest fits between the calculated spectral lines and the experimentally observed ones an interesting objective law was stated. It turns out that the channeling electrons energy increase causes a slight but still visible decrease of the potential pits depths in $\mathrm{F}^- - (111)$ planes. The potential pits at this in $\mathrm{Li}^+ - (111)$ planes remain invariable. One may give a physical explanation to this phenomenon admit the opposite effect of the channeling particles on weakly bound external electrons of F^- ions at the expense of the proportionally increased to the Lorentz factor γ the transverse component of the electric field moving particle. At this the channeling relativistic electron polarizes crystal ions which resulting in the changing of a planar interaction potential itself analogous to the screening effect of ion potential due to media polarization (see, for example, [9]). From the mathematical point of view it is expressed by the alteration of a_i and ζ_i parameters of the wave function of (3). At the same time the channeling particle influence on strictly bound 1s-electrons of Li^+ ions, is apparently negligible. In general,-this question needs a more detailed investigation, since accounting delayed effects in space and in time the screening leads to so-called wake potential appearance [9] which mechanism of origination in ionic crystals is treated in [8].

Comparing the data represented in Fig. 8a and Fig. 9a, b we see that in the case of LiF crystal the inversion effect occurs for more light $\mathrm{Li}^+ - (2m+1, 2n+1, 2p+1)$ planes starting from (511) planes. It means that one more effective confirmation of the calculated interaction potential validity could be the experimental observation of the only spectral line with $\sim 65\,\text{keV}$ energy on $1 \to 0$ transition occurring at the channeling of relativistic electrons with $\gamma = 150$ Lorentz-factor along the charged (511) planes of LiF crystal. In the case of (311) planes at the direct $1 \to 0$ transitions at $\gamma = 107{,}1$ there will be radiation with $\sim 80\,\text{keV}$ energy, at $\gamma = 60{,}7$ – the radiation with $\sim 27\,\text{keV}$ energy and at $\gamma = 34$ the radiation with $\sim 7\,\text{keV}$ energy may occur only at the expense of $0' \to 0$ tunnel transitions.

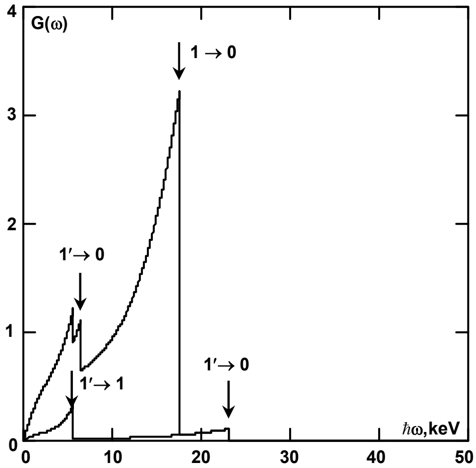

Fig. 8. The spectral density of QCR intensity calculated in relative units in a dipole approximation and occurring at relative electron beam channeling *E* = 16,9 MeV along (111) planes of LiF crystal (an electron beam has an angular dispersion of $\vartheta_0 \approx 0{,}15$ mrad and an incident angle of $\vartheta = 0$)

Let's come to the consideration of electron interaction potentials of electrons with high indices charged $(2m+1, 2n+1, 2p+1)$ planes in LiF crystal. In particular, in Fig. 9a, b there are electron interaction potentials with the charged (311) and (511) planes respectively, calculated at home temperature allowing observing the dynamics of the transformation of the potential pits into the potential barriers at the change of the type of the channeling plane.

At last It should be noted that the influence of temperature factor on the formation of interaction plane potentials for LiF crystal as seen from Fig. 10a, b, c is negligible: temperature increase leads to the decrease of the depths of potential pits in Li^+ and F^- planes, but does not lead to the inversion of the potential relief.

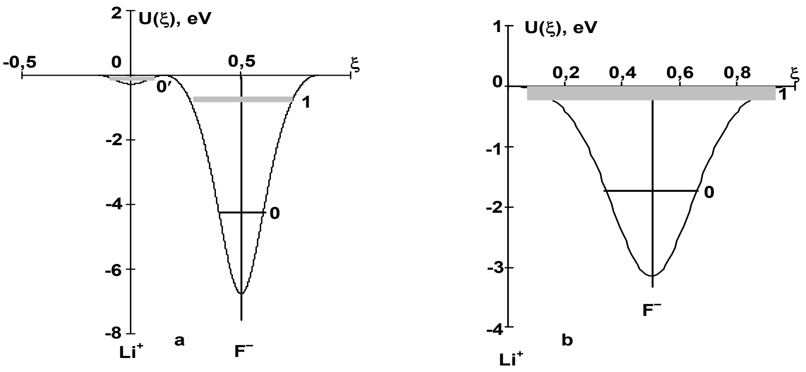

Fig. 9. Electron interaction potentials at their channeling in LiF crystal: (a) – in (311) planes, (b) – in (511) planes and energy levels arising at the channeling of electrons in these planes respectively with Lorentz-factors $\gamma = 107{,}1$ and $\gamma = 150$

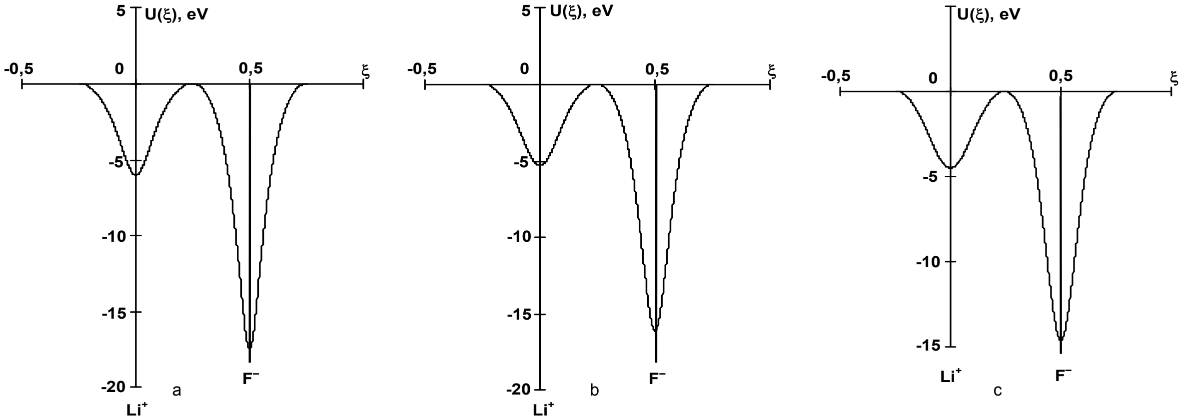

Fig. 10. Electron interaction potentials at their channeling with (111) planes of LiF crystal: (a) – at T = 0 K, (b) – at T = 300°K, (c) – at T = 600 K

General analysis of the effects of relativistic electron channeling in charged high-indices planes of ionic LiF crystal. To sum up we came to a general conclusion: the reasons of non-coincidence in the explanations of spectral line position in LiF crystal (in [14]) with our analytical results are evidently due to non-correct calculation of electron interaction potentials with charged planes in these papers (charged planes in these papers are not taken into account at all). Note that analogous demands could be made completely just to the content of the paper [12], since their calculations of spectral intensities are based on the potential pit structures in (111) planes of LiF crystal given in [14]. In addition if in [14] we speak on a possibility of one-partial interaction potentials restoration for isolated Li^+ and F^- ions by means of form-factors of electron dissipation just in [12] similar calculations are treated only concerning neutral Li and F atoms. In this case to find one-partial potentials one may get used of Tomas-Fermi atom model (see [1, 9]). If return to ions, the calculation of their electrostatic one-partial potentials either by means of factor formalism forms or the way we used in our paper could lead to Coulomb components (see the formulas (1) and (6)). Planar potential calculation leads in the long run to the following conditionally convergent series:

$$V_\pm(x) = V_0 \sum_{n=-\infty}^{\infty} \left[\left| x + nd - \frac{d}{2} \right| - \left| x + nd \right| \right]. \qquad (25)$$

From mathematical point of view series (25) don't lead to a definite meaning. However if takes into account a real physical situation where a longitudinal crystal dimension is many times less than the transverse one, the problem could be solved. Then as it was done in [7], the interaction potential with the alternative positively and negatively charged "frozen" (111) planes (Li^+ and F^-) is represented as the following wake potential:

$$V_\pm(x) = \alpha V_0 \sum_{n=-\infty}^{\infty} \left[\left| x + nd \right| - \frac{d}{4} \right] \chi\left(\frac{d}{2} - \left| x + nd \right| \right). \qquad (26)$$

Further averaging the potential (26) by the thermal oscillations (in positively charged with u_+ amplitude and in negatively charged with u_- amplitude), we get a final expression

$$W_\pm(x) = \sum_{k=-\infty}^{\infty} U_\pm(x - kd). \qquad (27)$$

Namely this expression (27) is a consequence of Coulomb components in one-partial potentials (1) and (6) is not completely taken into account in [14]. It is easy to show that planar (111) potential given in [14] for LiF crystal is almost close fit to our potentials at $\alpha = 0$ (these potentials $U(x, \alpha = 0)$ in dimensioneless units ξ are shown in Fig. 11a).

Thus the potential of the channeling electrons interaction with (111) planes in used in LiF crystal used in [14] (got on the basis of form-factor formalism) is of a little difference from the analogous potential calculated in the given paper (compare with Fig. 11b).

Besides, by means of analytical expression $U(x) = W_0(x) + W_\pm(x)$ it is easy to observe the contributions into the potential $U(x)$ of electron neutral main part $W_0(x)$ and non-compensated Coulomb part of $W_\pm(x)$. As it is seen from Fig. 11c, the potential pits in $\mathrm{Li}^+ - (111)$ planes for both crystals created by electro neutral skeleton

$W_0(x)$ potentials, are very shallow. Just the account of the potential $W_{\pm}(x)$ represented in Fig. 11d leads to a sharp increase of the depths of these potential pits. This is just the essence of positron-likeness orientation motion of negatively charged particles in such charged planes: in the domains with the reduced electron and nucleus densities at the expense of Coulomb component (27) quite strong interaction potentials arise.

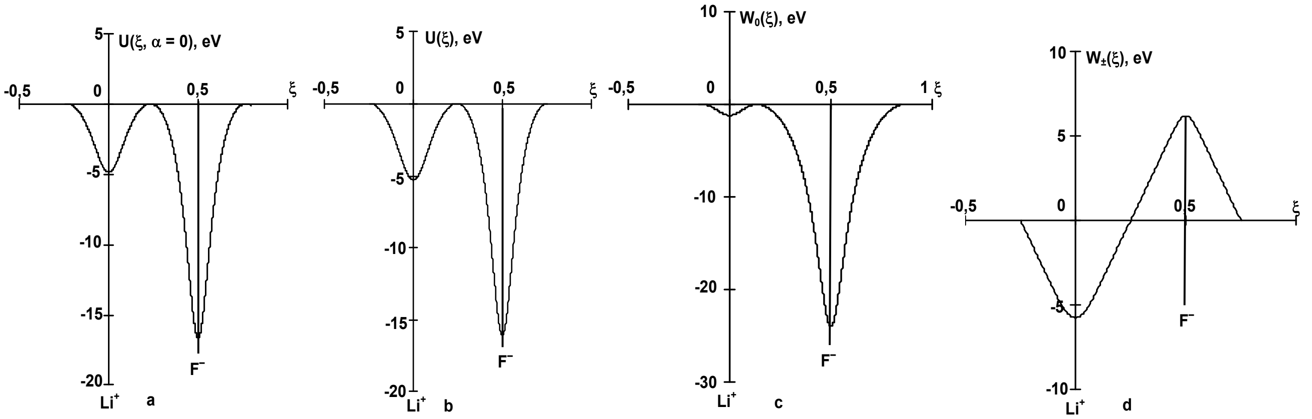

Fig. 11. Interaction potentials of channeling electrons with (111) planes of LiF crystal:
(a) – in the case of α = 0, corresponding to [14], (b) – in the case of α ≠ 0 corresponding to the results of our paper (c) – originated of electroneutral skeletons of Li^+ and H^-ions, (d) – occurring of non-compensated positive and negative charges of these ions

Conclusion. It has been got in the paper the interaction potential (13) of the channeling electrons with the charged $(2m+1, 2n+1, 2p+1)$ planes for the ionic LiF crystal. It has been carried out a detailed analysis in the case of (111) planes resulted in a possible anomalous channeling regime in $Li^+ - (111)$ planes since these planes tend to create quite deep potential pits at relatively low values of electron and nucleus densities. Just in $F^- - (111)$ planes, on the contrary, the potential pits become shallower as compared with those ones which should be present in covalent crystals at the same electron and nucleus densities. Nevertheless, at the transition to high-indices planes the inversion of the potential pits into potential barriers occurs in $Li^+ - (111)$ planes. Really in the paper it has been shown that the inversion of the potential pits into the potential barriers in this crystal takes place beginning with the high indices (511) planes. It means that in this case the processes of the deformation of the potential pits transforming gradually into positive charged planes constructed from Li^+ ions lead to so-called positron-like motion regime concerning these planes (the electrons attracting to $F^- - (511)$ planes are repulsing from $Li^+ - (511)$) planes. Temperature changes at this almost don't influence the inversion effect. As it is seen from Fig. 10a, b, c, only the decrease of the potential pits depths takes place (at this in F^- planes such alternations become stronger than in Li^+ planes which is the main reason for the inversion effect appearance).

For the electrons with Lorentz-factors $\gamma = 106{,}7$, $\gamma = 60{,}7$ and $\gamma = 34$ in (111) planes of LiF crystal transverse level spectrum of channeling motion were calculated and the possibilities of transactions between them were considered. The position of quasi-characteristic radiation spectral lines was calculated and the comparison with experimental data presented in [14] was carried out on the basis of these transitions. Besides, the functions of spectral densities of QCR intensities have been calculated for all these electron energies (along with direct transitions the contribution of indirect transitions to spectral dependencies has been taken into account as well which was not under consideration in [14]). In spite of the fact that all these calculations have been done in dipole approximation, as it follows from the comparison of all these calculations data with the results of the experiments (see [14]) our calculations lead to more adequate close fit between the theory and experiments than it is substantiated in [14].

It is necessary to note that the results of the comparative analysis between the calculated spectral lines and the experimentally observed ones stated that the channeling electrons energy increase leads to their opposite polarize effect on planar interaction potentials resulting in the potential pits depths increase in $F^- - (111)$ planes. Evidently accounting delayed effects in space and time such polarization leads to the appearance of so-called wake potential.

The obtained results may be used for the optimization of some radiation processes. In particular, they may serve the basis for calculation apparatus at the elaboration and creation of high-effective rebuilding sources of a rigid quasi-monochromatic radiation of X-ray and gamma-ranges on the basis of the channeling of the relativistic electrons. Anomalously weak electron dissipation, braking and dechanneling at their motion in positively charged planes of LiF crystal (in positron-like motion regime) promotes radiation lines narrowing and their intensities sharp increase. Note that the term "positron-likeness" in the paper is used in two senses. In the first case it is used when the inversion of the potential pit into a potential barrier occurs and we use this term to emphasize that electrons are not attracted to these planes but repulsed. In the second case the term "positron-likeness" is used to indicate more favourable conditions of the charged particles channeling (for example electrons in Li^+ planes). Naturally these two senses would coincide if we succeeded in the realization of electrons channeling motion in inter-planar space. Analogous remarks could be ascribed to the term "electron-likeness" as well.

Note one more unimportant moment. By means of the expressions (13.1) ÷ (13.4) it is easy to show that the calculated potential pits in (100) and (110) planes are in a very close fit to the analogous potential pits represented in [14]. On the other side, at $\alpha = 0$ we also come to the similar result. First, all this ascertains that all our calculations are quite correct starting from the consideration of one-partial potentials (1), (6) and finishing with the averaging by planes (see (8)) and by thermal oscillations (see

(13.1) ÷ (13.4)). Second, contributions into planar potentials (100) and (110) at $\alpha \neq 0$, reflecting a real situation of interaction potentials originating of non-compensated negative and positive ion charges are also zero since the amplitudes of thermal oscillations of various ions are different. May be this fact will allow at some supplementary conditions to realize electrons channeling motion in a true positron-like regime.

In the conclusion of the paper It should be noted that the presence of all such peculiarities of electron motion in charged crystallographic planes of LiF crystal may contribute to the creation of the intensive reconstructed sources of short wave QCR and also to the solution of gamma-laser construction problem on the basis of mono-energetic beam of relativistic electrons based on one of the schemes considered in [4].

1. *Базылев В.А., Жеваго Н.К.* Излучение быстрых частиц в веществе и во внешних полях. – М.: Наука, 1987. 2*. Бейтмен Г., Эрдейн А.* Высшие трансцендентные функции. – М.: Наука, 1974. 3. *Бете Г., Солпитер Э*. Квантовая механика атомов с одним и двумя электронами. – М.: Физмагиз, 1960. 4. *Высоцкий В.И., Кузьмин Р.Н.* Гамма-лазеры. – М.: Изд.МГУ, 1989. 5. *Высоцкий В.И., Кузьмин Р.Н., Максюта Н.В*. О возможности аномального каналирования электронов в ионных кристаллах // Тез. докл. XVI всесоюз. совещ. по физике взаимод. заряж. частиц с кристаллами. – М.: Изд. МГУ, 1986. 6. *Готт Ю.В.* Взаимодействие частиц с веществом в плазменных исследованиях. – М.: Атомиздат, 1978. 7. *Корхмазян Н.А., Корхмазян Н.Н., Бабаджанян Н.Э.* Эффективный потенциал плоскостного каналирования в кристалле LiH // ЖТФ. – 2003. –.73. вып. 8. 8. *Максюта Н.В*., *Высоцкий В.И.* Расчет и влияние кильватерного потенциала на каналирование релятивистских заряженных частиц в ионных кристаллах // Тез. докл. XXXIX межд. конф. по физике взаимод. заряж. частиц с кристаллами. – М.: Изд. МГУ, 2009. 9. *Оцуки Х.* Взаимодействие заряженных частиц с твердыми телами. – М.: Мир, 1985. 10. *Радциг А.А., Смирнов Б.М*. Параметры атомов и атомных ионов. Справочник. – М.: Энергоатомиздат, 1986. 11. *Смирнов Б.М.* Отрицательные ионы. – М.: Атомиздат, 1978. 12. *Bogdanov O.V., Korotchenko K.B., Pivovarov Yu.L., Tukhfatullin T.A*. Angular distributions of diffracted X-ray radiation from channeled electrons in Si and LiF Crystals: Influence of energy levels band structure // Nucl. Instr. and Meth. in Phys. Res. B. – 2008. – 266. 13. *Phillips J.C.* Ionicity of the chemical bond in crystals // Rev. Mod. Phys. – 1970. – 42. N. 3. 14. *Swent R.L., Pantell R.H., Park H. et al.* Planar and axial channeling radiation from relativistic electrons in LiF // Physical review B. – 1984. – 29. N. 1.

Submitted on 28.12.11

UDC 621.039.6

**I. Bekh, Ph.D., V. İl'chenko, Dr. Sci., A. Kravchenko, Ph.D.,
V. Telega, Ph.D., V. Prysyazhny, stud.**

ANALYSIS OF THE DIFFERENT KINDS OF FOOD BY SEMICONDUCTOR SNO$_2$/P-SI SENSORS

В роботі за допомогою мас-спектрометричної методики досліджено компонентний склад газової атмосфери, що утворюється при зберіганні м'яса та риби протягом різного терміну та при різних температурах. Показано, що з ростом терміну зберігання спостерігається зростання парціального тиску окису та двоокису вуглецю. Аналіз кореляції даних мас-спектрометрії та відгуку напівпровідникових сенсорів на основі гетеропереходу SnO$_2$/p-Si із різною товщиною шару окису олова дозволив обрати сенсор із оптимальними параметрами.

Ключові слова: мас-спектрометрія, газ, сенсорна гетероструктура, кремній, вольт-амперна характеристика, м'ясо, риба.

In these work analysis of the masses-spectroscopy composition of gases, which evolve at various period and temperatures of storage of the meat and fish were carried out. It is shown, that the basic gases, which registered by mass-spectroscopic method, are carbon oxide (CO and CO$_2$). Analysis of the correlation coefficient between sensor response and mass-spectroscopic data allows us to determine the sensor with the optimized parameters.

Keywords: mass-spectroscopy, gas, sensor heterostructure, silicon, current-voltage characteristics and their derivatives of sensor structures, meat, fish.

Introduction. The nanostructure thin film of semiconductors oxides are used for the construction of gas sensor. Such sensors have named resistive, from the parameter, which is under control. Diode-like thin film heterostructure based on nanometer-scaled semiconductor oxides can be used as the gas-sensitive receptor and transducer system [1]. Against resistive oxide sensors, which one has a linear current – voltage characteristics, the nonlinearity current – voltage characteristics of the diode-like heterostructure can be utilized for the new approaches to the creation gas-sensitive structures. In such structures all parameters, which characterize nonlinearity of the current – voltage characteristic of the heterostructure can be used as supplemented functionally important parameters.

The aim of the work is to study of the gas mixtures, which evolve at the various period and temperature of the storages of the meat and fish; to research responses of sensory structures depending on the weight thickness of adsorption-active layer in gases mixtures; to research responses of sensory structures depending on the different kinds of meat (beef and pork) and fish (carp) by sensors with the optimized parameters.

Experimental. For the analyzing of gases in experimental installation was used masses-spectroscopic MH-7304. The masses-spectroscopic was calibrated by nitrogen with energy ionizing electron 60 eV. The measurements were realized under room temperature. In process of the measurements parameters masses-spectroscopic did not change.

The experimental heterostructure *SnO$_2$-Si* structures with superthin *SnO$_2$* nanocrystalline layers were grown by magnetron sputtering deposition technique. Boron doped p-*Si <100>* single crystal wafers with receptivity equal 4 Ohm·cm. were used as a substrate. The *Au* (rectifying) and back (Ohmic) electrodes were deposited by vacuum evaporation technique. On Fig.1 the sensor structure is shown.

Measurements of the current – voltage characteristics were carried out as it defined in [2]. The feature of the measuring technique was that at the measurement of current – voltage characteristics on the DC is padding the alternating voltage by the amplitude less than 0,1 *V* at the frequency (*f*) range 100 - 1400 kHz was applied. The technique of research allowed to measure not only current - voltage characteristic on DC, but also second derivative of the current – voltage characteristics.

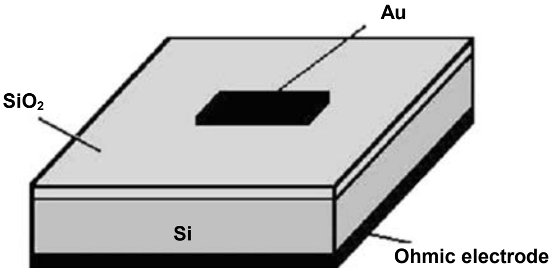

Fig. 1. The sensor structure.

For example, preliminary researches of sensory structures for testing of meat and fish at the various period of storage are on the Fig. 2 and Fig. 3.

Creation of prototypes of gas sensors and development of mathematical algorithm of analysis of the results got with their help shown that informative parameters are: i) position of maximum of second derivative (voltage); ii) normalized maximum of second derivative of the current-voltage characteristic; iii) the change of frequency on which is observed maximum of the second derivative of the current-voltage characteristic.

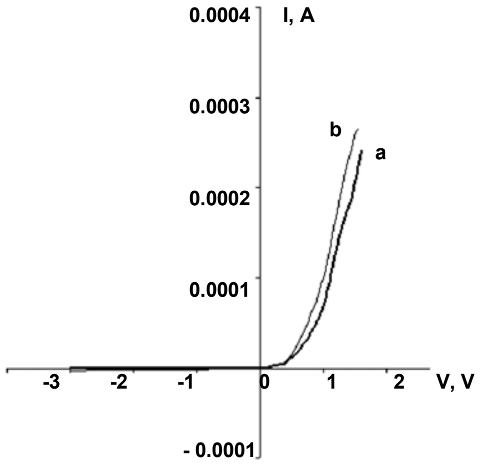

Fig. 2. The current-voltage characteristic of sensor structure with the weight thickness of the adsorption-active layer about 7 nm for the tests of gas from laboratory atmosphere (a) and container with fish for the term of 3 days storage at –1^0 C (b).

Gas-sensitive sensors based on SnO_2/p-Si with SnO_2 layer thickness equals 7 nm, 15 nm and 20 nm are used to analyze the gas release from meat (beef/pork) and fish (carp) samples. Selected information parameter, which quantitative and qualitative changes controls in measuring of current-voltage characteristics, was value of current-voltage characteristic second derivative maximum in gas environment normalized by the same sample measuring on start (storage time – 0 day). On the next step, gained data in current-voltage characteristics analysis compared with gas mixture analysis results of mass spectroscopy (MS) method.

The coefficient of correlation between the response of the gas sensor and data of MS has been calculated by the next way. If we have two sets of the data x_i (i = 1, 2, 3, ..., n) and y_i (i = 1, 2, 3, ..., n), the coefficient of correlation between them can be calculate by next expression:

$$corell(x;y)=\frac{\frac{1}{n}\sum x_i y_i-\frac{1}{n^2}\sum x_i\sum y_i}{\sqrt{\frac{1}{n}\sum(x_i-\bar{x})^2}\sqrt{\frac{1}{n}\sum(y_i-\bar{y})^2}}.$$

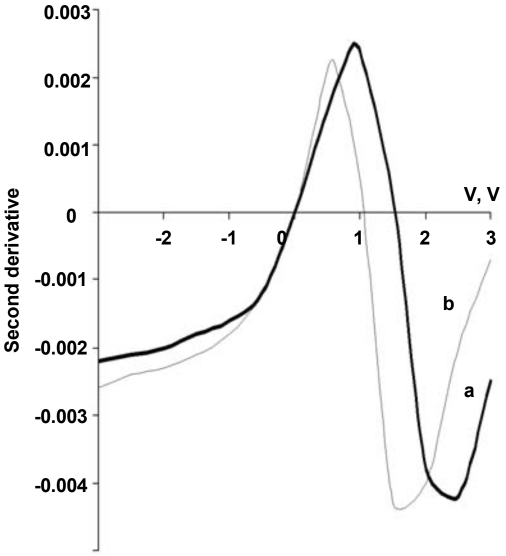

Fig. 3. Dependence of second derivative of current-voltage characteristic of sensor structure with the weight thickness of the adsorption-active layer about 7 nm for the tests of gas from laboratory atmosphere (a) and container with fish for the term of 3 days storage at –1^0 C (b).

Results and discussion. Gas mixture analysis results of mass spectroscopy shown, that in an atmosphere of a sample during the storage at +3 °C prevail the following components: atomic and molecular nitrogen (N and N_2), atomic and molecular oxygen (O and O_2), pairs of water (H_2O), an oxide of carbon (CO), a dioxide of carbon (CO_2), an argon and a radical OH. The masses numbers answering to the indicated components are given in the Table 1.

Table 1

Mass number	12	14	16	17	18	28	32	40	44
Components	C	N	O	OH	H_2O	CO	O_2	Ar	CO_2

The analysis of the received results allows asserting, that during the storage of meat under temperature +3 °C in atmosphere of exemplar of amount of the dioxide of carbon and an oxide of carbon increases.

Also for a changes example cause give pressures of other gas. These diagrams for temperature of storage at 20 °C are given on Fig. 4 and Fig. 5.

Analyzing results of the studies it is necessary to note, that quantity CO_2 which is oozed from stuffs food, depend on a period of storage, augment and gets peak meaning in 4-6 day of storage. Similar dynamics is observed and for carbon. Analyzing these result, and comparing them with visual observations over changes of explored product, it is possible to speak that meat starts to spoil intensively after the first day of a storage at 20 °C.

Values of correlation coefficient between sensor response and MS data for beef, pork and fish samples stored at -1 °C shown in Table 2.

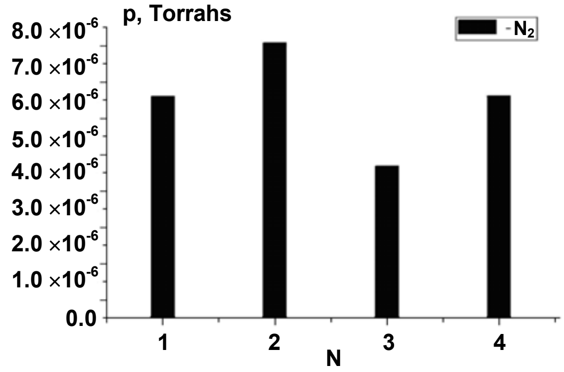

Fig. 4. Dynamics of changes of partial pressures of nitrogen at p=3·10^{-5} Torrahs:
1 – laboratory atmosphere; 2 – 1 day (meat) at 20°C; 3 – 3 days (meat) at 20°C; 4 – 6 days (meat) at 20°C.

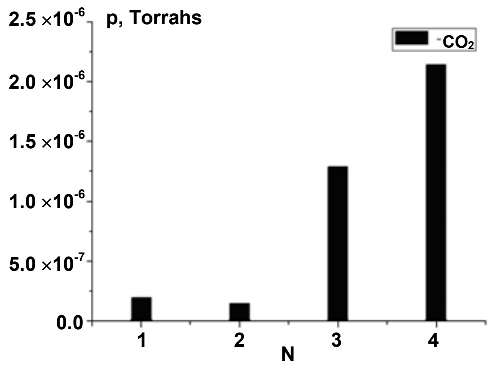

Fig. 5. Dynamics of changes of partial carbon dioxide pressures at $p=3\cdot10^{-5}$ Torrahs:
1 – laboratory atmosphere; 2 – 1 day (meat) at 20°C;
3 – 3 days (meat) at 20°C; 4 – 6 days (meat) at 20°C.

Table 2

	beef			pork			fish		
Sensor, nm.	7	15	20	7	15	20	7	15	20
Mass number 12									
corell(sensor(400 kHz);MS)	78%	26.9%	15.6 %	86.9%	-45.2%	-4.7%	53.9%	64.9%	-27%
corell(sensor(700 kHz);MS)	83%	39.3%	-15.2%	13.7%	29.4%	34.5%	56.8%	50.9%	46.4%
Mass number 14									
corell(sensor(400 kHz);MS)		66%	5.4%	-54.6%	2.1%	57%			16.5%
corell(sensor(700 kHz);MS)		-33.7%	24%	-98.9%	-4.9%	87%			87.9%
Mass number 16									
corell(sensor(400 kHz);MS)		44.6%	-8.1%		5.9%	45.6%			16.3%
corell(sensor(700 kHz);MS)		-4.8%	-5.1%		18.8%	84%			88.1%
Mass number 18									
corell(sensor(400 kHz);MS)		-43.8%		74.4%	-20.8%	-91.9%	17.2%	-31%	
corell(sensor(700 kHz);MS)		-14.5%		32.8%	96.1%	-81.9%	33.3%	-13.9%	
Mass number 28									
corell(sensor(400 kHz);MS)	84.3%			87.8%			55.4%		
corell(sensor(700 kHz);MS)	77.8%			74.4%			60.5%		
Mass number 44									
corell(sensor(400 kHz);MS)	78.8%	-22.9%		83.8%	-46.3%	-42.4%	49.2%	62.8%	21.6%
corell(sensor(700 kHz);MS)	86.1%	42.2%		11.6%	31.5%	-36.9%	58.8%	57.5%	-31.5%

So, obtained results allows us to make the conclusion that the SnO_2/p-Si gas sensors with the thickness of the SnO_2 film in 7 nm and 20 nm are the best for the analysis of the gas atmosphere of samples of meat and fish on the different stages of storage. For the SnO_2/p-Si gas sensor with the thickness of the SnO_2 film in 20 nm, the amplitude of maximum of the second derivative of current voltage characteristics mast be measured on frequency ~ 400 kHz. For the SnO_2/p-Si gas sensor with the thickness of the SnO_2 film in 7 nm, the amplitude of maximum of the second derivative of current voltage characteristics can be measured as on frequency ~ 400 kHz, so on frequency ~ 700 kHz.

The low values of the coefficient of correlation between the response of the gas sensor (especially for sensor with the thickness of the SnO_2 film in 20 nm) and data for a 28 mass (of mass-spectroscopy dates) for the samples of meat can be explained by not good monotony of the real dependencies for MS and sensor data, measured on frequency ~ 400 kHz.

The real dependencies for MS and sensor data for the samples of fish demonstrate good monotony, so the values of the coefficient of correlation between the response of the gas sensor and data for a 28 mass are higher.

Hence, we can make some conclusions based on obtained results. The most sensitive structure SnO_2/p-Si for gas environment analysis of meat (beef/pork) on different stages of storage time are sensor with SnO_2 layer thickness equals 7 nm. Best results observed for 400 kHz from high-frequency small magnitude signal. Sensor response on mentioned generated frequency shows good correlation with MS data (mass numbers 28 – CO and 44 – CO_2).

Gas extraction analysis for fish samples on different storage time observed for the same sensitive structure SnO_2/p-Si with adsorption-active layer thickness equals 7 nm. But best results for fish samples observed for 700 kHz from high-frequency small magnitude signal. Sensor response on indicated frequency shows satisfactory correlation with MS data (mass 28 – CO and mass 44 – CO_2).

Conclusions. In volumes where kept food products occur changes of partial pressures of gases are, in comparison with atmospheric air.

For analysis of freshness of the food products of possible change use of partial pressures a carbon and carbon dioxide.

As informative parameters which can be used in sensor, it is possible to select dependence of normalized maximum of the second derivative of the current-voltage characteristic.

The SnO_2/p-Si gas sensors with the weight thickness of the SnO_2 film about 7 nm is the best for the analysis of the gas atmosphere of samples of meat and fish on the different stages of storage.

1. *Il'chenko V.V., KravchenkoA.I., Grinchenko V.T.* Device for detection of gases and method of it use. Patent of Ukraine. #64151 G 01N7/00 G01N27/00. Priority from 17.02.2003. Bulletin #2, 16.02.2004.
2. *V.Il'chenko, V.Chehun, R.Gul, L.Il'chenko, A.Yushchenko.* Analysis of gas environment composition on the basis of analysis properties of the current-voltage characteristics of the nanostructure. // MICRO SYSTEM Technologies 2005 International Conference & Exhibition, Munich (Germany), 2005, p. 8. http://www.mesago.de/mst

Submitted on 25.10.11

UDC 535.326

I. Vasyliev, stud., S. Kolienov, Ph.D.

DIFFRACTION OF LIGHT BY ACOUSTIC WAVES IN PERIODIC LAYERED

У роботі за допомогою комп'ютерного моделювання досліджена дифракція світла на акустичних хвилях в періодичній структурі. З'ясовані особливості розповсюдження світлових та акустичних хвиль в періодичній структурі, зокрема в її елементарній комірці (хвилеводі). Показано, що в наведеній періодичній структурі розповсюджуються лише плоскі акустичні хвилі. Було показано, що наявність періодичної структури не впливає на кутовий розподіл дифракційного спектру, але впливає на амплітудний розподіл. Отримані дані порівняні з експериментом.

Ключові слова: дифракція на акустичних хвилях, дифракція Рамана-Ната, періодична структура, шаруваті середовища.

In presented article the diffraction of light by acoustic waves in a periodic structure is investigated. The features of light and acoustic waves propagations in a periodic structure, particularly in its unit cell (a waveguide) are clarified. It is shown that in the following periodic structure only plane acoustic wave is propagated. It was shown that the presence of the periodic structure does not affect on the angular distribution of diffraction spectrum, but effects on the amplitude distribution. The data is compared with experiment.

Keywords: diffraction of acoustic waves, Raman-Nath diffraction, periodic structure, layered environment.

Introduction. Diffraction of light at ultrasonic waves are widely used in optics, spectroscopy, laser physics, transmission systems and processing for spatial control of light beams. But there are certain problems such as increasing the efficiency of diffraction, managing energy distribution in the diffraction spectrum, and so on. Lately a lot of work, which revealed unique properties of periodic layered media, which were not previously observed in continuous media [3], while in some works proposed using periodic structures as a promising material for creating acoustic optical devices with improved performance [4]. It was therefore proposed to consider the usual diffraction of light by acoustic waves, but realized in the middle of the structure, which has a periodicity of refractive index against frequency created by the acoustic wave, and to investigate the diffraction spectrum formed in this structure.

Development and discussion. The proposed structure (Fig. 1) consisting from two layers: solid (layer I) and liquid (layer II). Layer thicknesses were identical and equal to 200 microns. As used solid glass, and as liquid used water. Consideration of the interaction of light with acoustic waves in this structure was carried out assuming that the acoustic wave is distributed only in layers of liquid.

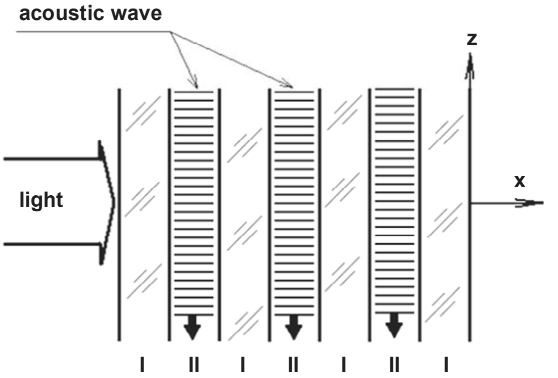

Fig. 1 Model of the periodic structure

In the middle of each cell formed by the second layer periodic structures, diffraction of light on acoustic waves occurred in the Raman-Nath mode. [1] In this mode, the distribution of light intensity on the diffraction maxima is described by the relation:

$$I_p / I_0 = J_p(qx) \quad (1)$$

where $J_p(qx)$ - Bessel functions, I_p – light intensity at p-diffraction peak, I_0 – the intensity of incident light. Charts the intensity of light in the zeroth, first and second maximum of ql shown in Fig. 2.

Diffraction of light on the sound waves in the liquid is considered in terms of the interaction of light with sound pole.

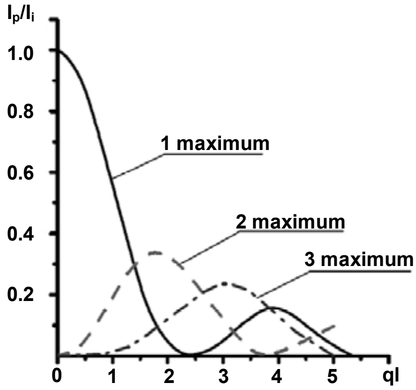

Fig. 2 Dependence of light intensity at the maxima

In this case, in each cell will occur diffraction of light on acoustic waves in the above-mentioned mode. Thus, for each cell of the acoustic wave (beginning with the second) the number of incoming rays that diffracts, equals the number of peaks that were formed during diffraction in the previous cell (Fig. 3).

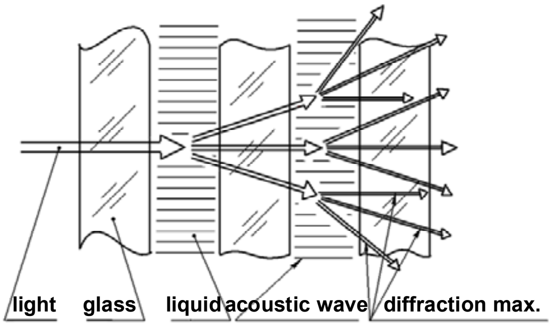

Fig. 3 Propagation of diffracted rays in the multilayer structure

Series experiments were made to find characteristics of acoustic wave propagating in a periodic structure. Speed of sound is determined from the diffraction spectrum. It is calculated from the angle of first maximum of diffraction. Calculated diffraction angle for liquid was 0.0019 rad. The experiments with the periodic structure and with clear liquid (without periodic structure) show that the angles of the first maximum of diffraction are identical and correspond to calculated one (Fig. 4).

So, we can assume that the sound is propagates inside the cells at the same speed as the outside (in the free atmosphere). Since speed is independent of the presence or absence on structure. It means that in the cell (waveguide) plane waves are propagated [2].

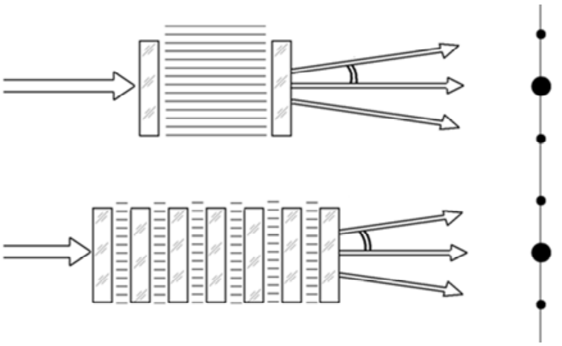

Fig. 4. Forming of the diffraction spectrum with diffraction maxima of the zeroth and first orders

Taking into account all above, the numerical calculation of the result of light and acoustic waves interaction in such structure was carried out. To check the results of calculation the periodic structure (period 400mkm, 22 layers) was set up. Propagation of diffracted rays in the multilayer structure is show on Fig 3. Diffraction spectrum, namely, the angular distribution of maximum intensity and the first maximum intensity changing relative to zero maximum intensity depending on the power of acoustic wave were investigated. Comparisons of the obtained results with the corresponding dependencies for the diffraction of light by an acoustic wave in the aperiodic medium with equivalent length were carried out also. Fig. 5 shows an example of the obtained dependences of the intensity of the first maximum (I1) with relative to the zero (I0), depending on the voltage at piezo transducer (V) for light with a wavelength of 532 nm, and frequency of acoustic waves - 2.5 MHz

Conclusions. It is revealed that the presence of the periodic structure does not affects to the spectral distribution of the diffraction pattern, but effects on the distribution of amplitude. It is determined that the acoustic wave propagation in cells (II) of this structure approximated corresponds plane waves propagation in a narrow waveguide with rigid walls. This approach was used in the simulation. A small divergence of the calculated and experimental data allows us to affirm the correctness of the choice model for theoretical calculations.

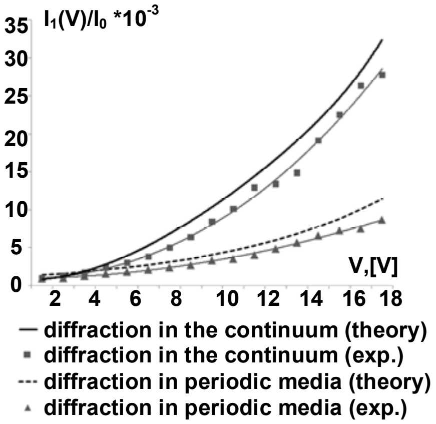

Fig. 5 Changing the intensity of the first maximum of diffraction spectrum (acoustic wave frequency 2.5 MHz)

Since the offered model agrees well with experiment, it allows the search of optimal conditions for increasing the efficiency of diffraction in a periodic structure by changing the elements of the periodic structure. Preliminary calculations have shown that at a certain choice of parameters of periodic structure with the smaller power of acoustic waves and smaller interaction length can give the diffraction spectrum such as for the solid medium. This suggests that creation of acousto-optic devices, with smaller dimensions and lower power consumption is possible.

1. *Балакший В.И., Парыгин В.Н., Чирков Л.Е.* Физические основы акустооптики – М.: Радио и связь, 1985. – 280 с. 2. *Бреховских Л.М., Годин О.А.* Акустика слоистых сред.-М.-Наука. Гл.ред. физ-мат. Лит., 1989. – 416 с. 3. *В.Г. Голубев, В.А. Кособукин, Д.А. Курдюков, А.В. Медведев, А.Б. Певцов.* Фотонные кристаллы с перестраиваемой запрещенной зоной на основе заполненных и инвертированных композитов опал–кремний // ФТП.- 2001, № 5. – С. 12–15. 4. *Z. A. Pyatakovaa, G. V. Belokopytov*. Acoustic-Optical Interaction in Photonic Crystals: Frequency Dependence of Bragg Angle // Moscow university physics bulletin – Vol. 64, No. 3, 2009, pp. 282–286.

Submitted on 14.10.11

UDC 537.6/.8

R. Verba, post grad. stud.

MICROWAVE PROPERTIES OF HEXAGONAL ARRAYS OF MAGNETIC NANO-DOTS

Spin-wave (SW) excitations in a two-dimensional magnonic crystal (MC) consisting of axially magnetized cylindrical nano-dots, arranged into hexagonal lattice, are considered. Frequency of ferromagnetic resonance (FMR) of an array into ferromagnetic (FM) state is shown to significantly depend on array's geometry. The possibility of array demagnetization into regular antiferromagnetic state is analyzed.

Key words: magnetic nano-dot, magnonic crystal, collective excitation, ferromagnetic resonance.

Розглядаються спін-хвильові збудження у двовимірному масиві аксіально намагнічених циліндричних магнітних наноточок, впорядкованих у гексагональну ґратку. Продемонстровано залежність частоти феромагнітного резонансу масиву у феромагнітному стані від геометрії масиву. Проаналізовано можливість розмагнічення масиву у регулярний антиферомагнітний стан.

Ключові слова: магнітна наноточка, магнонний кристал, колективні збудження, феромагнітний резонанс.

Introduction. Magnonic crystals (MCs) attract much attention recently due to their promising applications in microwave technologies [11]. There are two main types of MCs: first is formed by periodic patterning of continuous magnetic media (ferromagnetic film, etc.) [4, 5], while MCs of the second type are periodic arrays of distinct magnetic elements [6, 7]. MCs of the last type are interesting mainly since they can work (i.e. have nonzero resonance frequency, etc.) even in zero external magnetic field [3]. Also recently the possibility of changing MCs' microwave properties by variation magnetic ground state (magnetization distribution in an array) was shown, that opens a way to creation of tuneable artificial magnetic media [12, 13, 14].

In this work we consider two-dimensional MC with hexagonal lattice. For nano-dots of circular and hexagonal shape this type of lattice is the most close-packed, that leads to increasing of all collective effects. Also fabrication of arrays with hexagonal lattice can be simpler, especially while using modern self-ordering technology [1, Ch. 9].

The article is organized as following: firstly we will rewrite general theory of SW excitation in magnetic nano-dots' arrays [15] for our particular case, than microwave properties of MC in FM state is analyzed, and the possibility of dynamic ground state control is considered in the last section.

Theory. We will consider only FM state of an infinite periodic array, in which static magnetizations $\mathbf{M}_0$ of all dots are parallel (direction of $\mathbf{M}_0$ is denoted by unit vector $\boldsymbol{\mu}$ further). Assuming uniform profile of dynamic magnetizations $\mathbf{m}_j$ inside dots (so called macrospin approach), following equation for collective SW amplitude $\mathbf{m_k}$: $\mathbf{m}_j = \mathbf{m_k} e^{i\mathbf{k}\cdot\mathbf{r}_j}$ can be derived [15]:

$$-i\omega_{\mathbf{k}}\mathbf{m_k} = \boldsymbol{\mu} \times \widehat{\boldsymbol{\Omega}}_{\mathbf{k}} \cdot \mathbf{m_k}\,, \tag{1}$$

where tensor

$$\widehat{\boldsymbol{\Omega}}_{\mathbf{k}} = \gamma B \widehat{\mathbf{I}} + \gamma\mu_0 M_0 \widehat{\mathbf{F}}_{\mathbf{k}}\,. \tag{2}$$

Here $\gamma \approx 2\pi \cdot 28\, GHz/T$ is the modulus of gyromagnetic ratio; μ_0 is the magnetic permeability of vacuum; effective scalar magnetic field B is the sum of external field $\mathbf{B}_e$ and fields created by all other dots:

$$B = \boldsymbol{\mu} \cdot \left(\mathbf{B}_e - \mu_0 M_0 \widehat{\mathbf{F}}_{\mathbf{0}} \cdot \boldsymbol{\mu}\right). \tag{3}$$

Array's demagnetization tensor $\widehat{\mathbf{F}}_{\mathbf{k}}$ is defined as sum over reciprocal lattice L^* of two-dimensional Fourier-transform of mutual demagnetization tensor $\widehat{\mathbf{N}}(\mathbf{r})$ (defined in [2]):

$$\widehat{\mathbf{F}}_{\mathbf{k}} = \frac{1}{S_0} \sum_{\mathbf{K} \in L^*} \widehat{\mathbf{N}}_{\mathbf{k}+\mathbf{K}}\,, \tag{4}$$

where S_0 is the area of elementary cell of direct lattice, that in the case of hexagonal lattice with lattice constant a is equal to $S_0 = a^2\sqrt{3}/2$. For identical cylindrical dots with radius R and height h mutual demagnetization tensor is given by [2, 15]

$$\widehat{\mathbf{N}}_{\mathbf{k}} = \frac{4\pi J_1^2(kR)}{k^4} \begin{pmatrix} k_x^2 f(kh) & k_x k_y f(kh) & 0 \\ k_x k_y f(kh) & k_y^2 f(kh) & 0 \\ 0 & 0 & k^2\left(1 - f(kh)\right) \end{pmatrix}, \tag{5}$$

where J is the Bessel function of first kind and

$$f(x) = 1 - \frac{1 - e^{-x}}{x}\,. \tag{6}$$

Equation (1) is identical to the equation for a single macrospin with the effective demagnetization tensor $\widehat{\mathbf{F}}_{\mathbf{k}}$. Choosing a coordinate system (x', y', z'), in which the equilibrium magnetization direction $\boldsymbol{\mu}$ coincides with the z' axis, the SW frequency $\omega_{\mathbf{k}}$ can be derived in the explicit form:

$$\omega_{\mathbf{k}}^2 = \left(\gamma B + \omega_M F_{\mathbf{k}}^{(x'x')}\right)\left(\gamma B + \omega_M F_{\mathbf{k}}^{(y'y')}\right) - \left(\omega_M F_{\mathbf{k}}^{(x'y')}\right)^2, \tag{7}$$

where $\omega_M = \gamma\mu_0 M_0$.

The above formalism allows to define such practically important characteristics as SW damping rate

$$\Gamma_{\mathbf{k}} = \frac{\alpha_G \omega_{\mathbf{k}} \left|\mathbf{m_k}\right|^2}{i\mathbf{m}_{\mathbf{k}}^* \cdot \boldsymbol{\mu} \times \mathbf{m_k}} \tag{8}$$

and microwave absorption spectra

$$P(\omega) = \frac{\omega V N_d}{\mu_0} \mathbf{b}_e^* \cdot \widehat{\boldsymbol{\chi}}'' \cdot \mathbf{b}_e\,, \tag{9}$$

$$\widehat{\boldsymbol{\chi}}'' = \gamma\mu_0 M_0 \frac{i\Gamma_{\mathbf{0}}}{\left(\omega_{\mathbf{0}} - \omega\right)^2 + \Gamma_{\mathbf{0}}^2} \frac{\mathbf{m}_{\mathbf{0}}^* \otimes \mathbf{m_0}}{\mathbf{m}_{\mathbf{k}}^* \cdot \boldsymbol{\mu} \times \mathbf{m_k}}\,. \tag{10}$$

Above $\otimes$ denotes direct Cartesian product of vectors, α_G is the Gilbert damping parameter, ω is the frequency of external microwave field $\mathbf{b}(t) = \mathrm{Re}\left(\mathbf{b}_e e^{-i\omega t}\right)$, that is assumed to be uniform; N_d – number of dots in array and V – volume of dot.

Microwave properties. The above theory is applicable to any nano-dots array in ferromagnetic state in the case of simple lattice (i.e. when primitive cell contains only one dot). In this section the hexagonal array of dots, magnetized perpendicularly to array's plane is considered (see Fig. 1a).

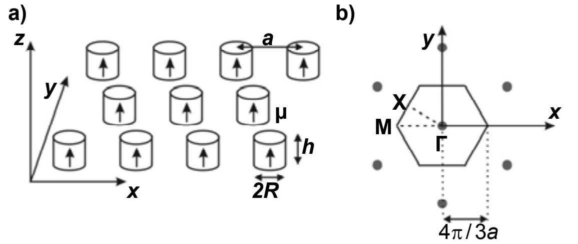

Fig. 1 Sketch of the array considered (a); the inverse lattice (gray circles) and boundary of the first Brillouin zone (solid lines) of the hexagonal lattice (b).

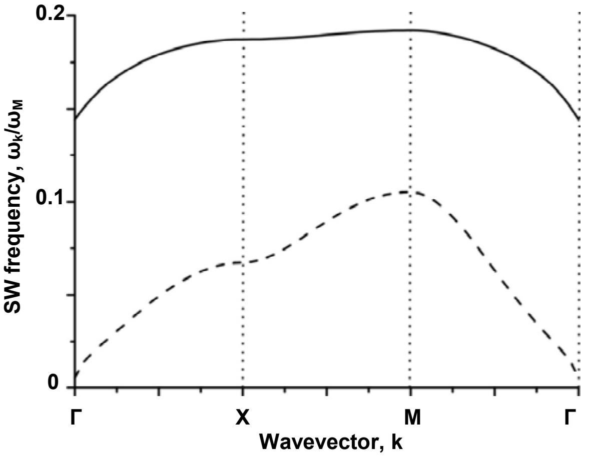

Fig. 2 SW spectrum in the hexagonal array of axially magnetized cylindrical nano-dots in FM state at zero external field. Parameters: dots' aspect ratio *h*/*R*=5, lattice constant *a*/*R*=5 (solid line) and *a*/*R*=3.7 (dashed line). Notation of symmetric points in Brillouin zone is shown on Fig. 1b.

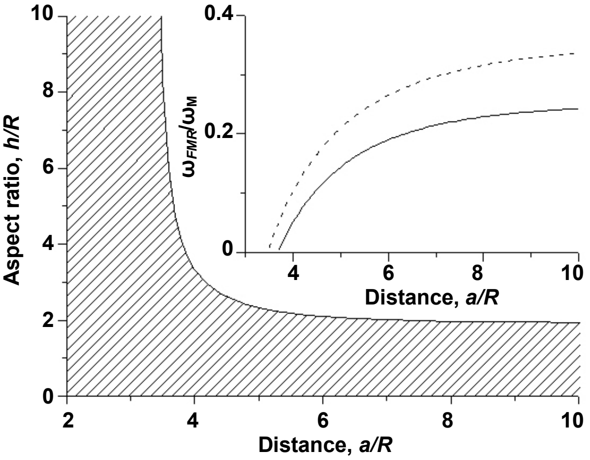

Fig. 3 Stability diagram. The region of FM state instability at zero external field is dashed. Inside: dependence of array's FMR frequency on lattice constant *a* for aspect ratio *h*/*R*=5 (solid line) and *h*/*R*=10 (dashed line).

Using Eq. (7) we have calculated SW spectrum of array considered (in this particular case coordinate systems (x, y, z) and (x', y', z') coincide). Excitation spectrum is monotonic in whole Brillouin zone and has minimum in its center and maximum in M-point (see Fig. 2) at any geometrical parameters and perpendicular to array's plane magnetic fields, at which FM state is stable. This means that FM state loses its stability firstly with respect to small wavevectors, and, particularly, under antiparallel magnetic fields array has to divide into domains with local FM states, just like continuous ferromagnetic film with out-of-plane anisotropy. Corresponding stability diagram is shown on Fig. 3. It should be noted, that even in the case of dots with large aspect ratio h/R FM state is not stable in zero field if dots are located edge-to-edge ($a/R=2$). This fact can be easily understood by noting, that such close packed array has to behave very similar to thin film, because array's plane sizes are assumed to be substantially greater than any other geometrical parameters. Of course, all above is true while dots are in the single-domain state [10].

From practical point of view it is important to know FMR frequency of array and velocity of SWs with small wavevectors (comparing to inverse lattice constant). Using Eqs. (4-5) one can shown that tensor $\hat{\mathbf{F}}_{\mathbf{0}}$ is diagonal with equal (*xx*) and (*yy*) components, that allow derive simple expression for FMR frequency:

$$\omega_{FMR} = \gamma B_e + \omega_M \left(F_{\mathbf{0}}^{(xx)} - F_{\mathbf{0}}^{(zz)} \right). \qquad (11)$$

FMR frequency is zero at the boundary of stability region and increase with separation between dots up to resonance frequency of one isolated dot (see Fig. 3). Thus, varying the geometrical parameter of array one can create a set of artificial materials with preassigned resonance frequency in range $[0, \omega_M/2]$ (for isotropic materials; by using anisotropic materials range of frequency variation can be substantially enlarged) that can work without applying external permanent magnetic field.

Near the point $\mathbf{k}=\mathbf{0}$ all tensors $\hat{\mathbf{N}}_{\mathbf{k}+\mathbf{K}}$, except $\hat{\mathbf{N}}_{\mathbf{k}+\mathbf{0}}$, can be expanded into common Tailor series:

$$\hat{\mathbf{N}}_{\mathbf{k}+\mathbf{K}} = \hat{\mathbf{N}}_{\mathbf{K}} + \hat{\mathbf{A}}_{\mathbf{K}} \cdot \mathbf{k} + O\left(k^2\right), \qquad (12)$$

where $A_{\mathbf{K}}^{(ij\alpha)} = \partial N_{\mathbf{k}+\mathbf{K}}^{(ij)} / \partial k_\alpha \Big|_{\mathbf{k}=\mathbf{0}}$ is the tensor of third rank. All $A_{\mathbf{K}}^{(ij\alpha)}$ are odd functions of either k_x, either k_y (but not of both together), thus after summation over inverse lattice linear term in $\hat{\mathbf{F}}_{\mathbf{k}}$ vanishes, because $\sum_{\mathbf{K}:|\mathbf{K}|=const,\neq\mathbf{0}} \hat{\mathbf{A}}_{\mathbf{K}} = 0$. The last term is expanded as

$$\hat{\mathbf{N}}_{\mathbf{k}+\mathbf{0}} \approx \frac{\pi h R^2 k}{2} \begin{pmatrix} \cos^2\theta_k & \cos\theta_k \sin\theta_k & 0 \\ \cos\theta_k \sin\theta_k & \sin^2\theta_k & 0 \\ 0 & 0 & 0 \end{pmatrix}, \qquad (13)$$

where θ_k is the angle between wavevector $\mathbf{k}$ and *x*-axis. Using above expression long-wave approximation for SW dispersion relation can be derived:

$$\omega_{\mathbf{k}} \approx \omega_{FMR} + \omega_M \frac{\pi h R^2}{2\sqrt{3}a^2} |\mathbf{k}| + O\left(k^2\right). \qquad (14)$$

So, SW spectrum in the range of small wavevectors is isotropic and has nonanalytical peculiarity at point $\mathbf{k}=\mathbf{0}$ (from above consideration it clear that this nonanalyticity is the general properties of arrays in FM state, which have mirror symmetry along *x* and *y* axes simultaneously). Comparing Eq. (14) with long-wave approximation of magnetostatic waves in perpendicularly magnetized thin film [9], one can see that group velocity in both cases are exactly the same if magnetic moments per unit area ($2\pi R^2 h M_0 / \sqrt{3}a^2$ for our case and hM_0 for film) are equal, like in array with square lattice [3, 15].

Ground state control. SW spectrum and, particularly, FMR frequency significantly depend on array's ground state. So, by ground state switching one may obtain artificial material with tunable microwave properties. Ground state control can be achieved in the arrays of nonidentical magnetic elements owing to dependence of magnetization reversal field on elements' geometry [12, 13]. However such arrays have following disadvantages: (i) slow quasistatic reversal processes and (ii) doubling of FMR peaks even in ferromagnetic state that may be not suitable for some application.

Arrays of identical magnetic dots have one FMR peak in FM state (if array's lattice is simple). Switching into FM state is trivial. Another ground state can be achieved by applying some field pulse with slow decreasing falling edge [14]. This method works if at some field small part of SW spectrum becomes instable, and array reaches state, that corresponds to instable wavevector.

It is of practical interest to switch arrays into fully demagnetized state (so called antiferromagnetic state – AFM), in which total magnetic moment of array is zero. In contrast to partially demagnetized states, AFM state can have rather simple periodic structure (i.e. small number of dots in elementary cell), like chessboard AFM state in the case of square array of dots [3] or stripe-like state of hexagonal spin lattice [8]. And number of dots in elementary cell is directly proportional to number of FMR peaks in absorption spectrum [15]. Obviously, in the case considered switching into AFM state is most probable under in-plane field pulse.

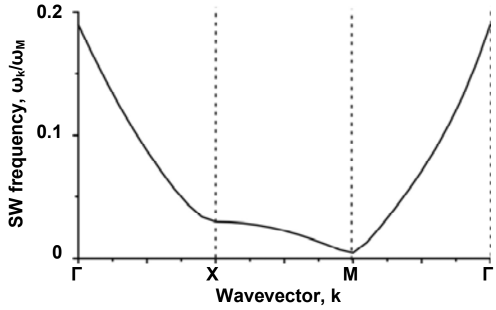

Fig. 4 SW spectrum of array in in-plane FM state under magnetic field *H/M*$_0$=0.217 directed along x-axis. Parameters: dots' aspect ratio *h/R*=5, lattice constant *a/R*=4. Symmetric points in Brillouin zone are chosen as on Fig. 1b.

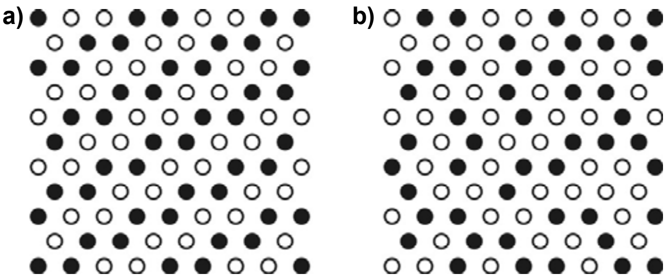

Fig. 5 Ideal periodic double-stripe AFM state (a) and remanent state of array after applying magnetic field pulse (b) with amplitude 0.25 *T* and length of falling edge 100 *ns* (numerical simulations, see detail in Ref. [14]). Black and white circles correspond to dots with opposite magnetizations. Array's parameters are as on Fig. 4.

SW spectrum of in-plane FM state is shown on Fig. 4. Near the boundary of stability spectrum has minimum at M-point at any in-plane direction of external field and at smaller fields M-point becomes instable. This corresponds to formation of double-stripe AFM state (see Fig. 5a), because wavevector in M-point $\mathbf{k} = (4\pi/3a, 0)$. But numerical simulation showed that this state forms only very locally (see Fig. 5b). Obviously, in such irregular state microwave absorption spectrum is very wide and isn't suitable for practice.

The reason of this behaviour is existing of three pairs of M-points in the Brillouin zone: $\mathbf{k}_{M_1} = (4\pi/3a, 0)$, $\mathbf{k}_{M_{2,3}} = \left(2\pi/3a, \pm 2\pi/\sqrt{3}a\right)$ and their mirror images. All of them can be transferred one to another by adding vector of inverse lattice $\mathbf{k}_{M_i} = \mathbf{k}_{M_j} + n\mathbf{K}_1 + m\mathbf{K}_2$, $\mathbf{K}_1 = \left(0, 4\pi/\sqrt{3}a\right)$, $\mathbf{K}_2 = \left(2\pi/a, 2\pi/\sqrt{3}a\right)$. Since SW spectrum is periodic with periodicity of inverse lattice (see Eqs. (2-4)), all M-points become instable at the same external field. Thus three different states may appear with equal probability, and long-range order can not be formed due to energy barriers between states formed by M_i-X-M_j zone (this barrier can be overcame if $\gamma k_B T \sim M_0 V(\omega_X - \omega_M)$. For the case considered this condition can be satisfied at room temperature by using dots with radius less than 3 nm for permalloy).

Conclusion. In this article the magnetic nano-dots' arrays with hexagonal lattice were investigated. From the point of microwave properties array in FM state is similar to ferromagnetic film with out-of-plane anisotropy – in both cases FMR frequency is nonzero at zero magnetic field, and SW spectrum in long-wave range is isotropic and nonanalytic. FMR frequency and SW group velocity significantly depend on array's geometry that can be used for creation of artificial magnetic materials with definite properties. Using of hexagonal arrays as dynamical magnonic crystals is not perspective due to: (i) complicated structure of demagnetized state and (ii) six-fold degeneracy of this state, that leads to appearing of complicated remanent state after demagnetization with broad FMR line.

The author is thankful to doct. V. S. Tiberkevich, Prof. A. N. Slavin and Prof. G. A. Melkov for valuable discussions.

This work was supported by the Grant No. M/90-2010 from the Ministry of Education and Science of Ukraine and by the Grant No. UU34/008 from the State Fund for Fundamental Research of Ukraine.

1. Advanced Magnetic Nanostructures, ed. by Sellmyer D. J. and Skomski R. – Springer, New York, 2006. 2. *Beleggia M., De Graef M.* On the magnetostatic interactions between nanoparticles of arbitrary shape // J. Magn. Magn. Mater. – 2004. – Vol. 278. – P. 270-284. 3. *Bondarenko P. V., Galkin A. Y., Ivanov B. A., Zaspel C. E.* Collective modes for an array of magnetic dots with perpendicular magnetization // Phys. Rev. B. – 2010. – Vol. 81. – P. 224415(1-13). 4. *Chumak A. V., Serga A. A., Hillebrands B., Kostylev M. P.* Scattering of backward spin waves in a one-dimensional magnonic crystal // Appl. Phys. Lett. – 2008. – Vol. 93. – P. 022508(1-3). 5. *Chumak A. V., Serga A. A., Wolf S., Hillebrands B., Kostylev M. P.* Scattering of surface and volume spin waves in a magnonic crystal // Appl. Phys. Lett. – 2009. – Vol. 94. – P. 172511(1-3). 6. *Gubbiotti G., Tacchi S., Carlotti G., Singh N., Goolaup S., Adeyeye A. O., Kostylev M.* Collective spin modes in monodimensional magnonic crystals consisting of dipolarly coupled nanowires // Appl. Phys. Lett. – 2007. – Vol. 90. – P. 092503(1-3). 7. *Gubbiotti G., Tacchi S., Madami M., Carlotti G., Adeyeye A. O., Kostylev M.* Brillouin light scattering studies of planar metallic magnonic crystals // J. Phys. D.: Appl. Phys. – 2010. – Vol. 43. – P. 264003(1-13). 8. *Joknys A., Tornau E. E.* Magnetic stripes on hexagonal lattice with competing exchange and dipole-dipole interaction // Acta Phys. Polonica A. – 2008. – Vol. 113. – P. 951-954. 9. *Kalinikos B. A., Slavin A. N.* Theory of dipole-exchange spin wave spectrum for ferromagnetic films with mixed exchange boundary conditions // J. Phys. C. – 1986. – Vol. 19. – P. 7013-7033. 10. *Metlov K. L., Guslienko K. Yu.* Stability of magnetic vortex in soft magnetic nano-sized circular cylinders // J. Magn. Magn. Matter. – 2002. – Vol. 242-245. – P. 1015-1017. 11. *Neusser S., Grundler D.* Magnonics: spin waves on the nanoscale // Adv. Mater. – 2009. – Vol. 21. – P. 2927-2932. 12. *Tacchi S., Madami M., Gubbiotti G., Carlotti G., Goolaup S., Adeyeye A. O., Singh N., Kostylev M. P.* Analysis of collective spin-wave modes at different points within the hysteresis loop of a one-dimensional magnonic crystal comprising alternative-width nanostripes // Phys. Rev. B. – 2010. – Vol. 82. – P. 184408(1-9). 13. *Topp J., Heitmann D., Kostylev M. P., Grundler D.* Making a reconfigurable artificial crystal by ordering bistable magnetic nanowires // Phys. Rev. Lett. – 2010. – Vol. 104. – P. 207205(1-4). 14. *Verba R. V.* Controllable transition of an identical magnetic nano-dots' array into antiferromagnetic state // Proceedings of the XIth international young scientists' conference on applied physics (Kyiv, June 15-18, 2011). – P. 58-59. 15. *Verba R., Melkov G., Tiberkevich V., Slavin A.* Collective spin-wave excitations in a two-dimensional array of coupled magnetic nano-dots // Phys. Rev. B – 2012 – Vol. 85. – P. 014427(1–14)

Submitted on 20.09.11

UDC 535. 36

Y. Ignatyev, stud., S. Radchenko, Ph.D.

ULTRASOUND QUANTITATIVE TEXTURAL ANALYSIS IN EFFECT OF THYROID HORMONES' INFLUENCE ON TISSUE GLAND STATE

В роботі аналізується характер розсіювання ультразвуку в тканинах щитоподібної залози при зміні фізичних параметрів стану паренхіми на прикладі концентрації гормонів у крові. В якості кількісної оцінки характеру розсіювання ультразвуку обрано параметр ефективної густини розсіювачів, яка вимірюється за допомогою розроблених алгоритмів обробки ультразвукових зображень щитоподібної залози.

Ключові слова: щитоподібна залоза, концентрація гормонів, розсіювання ультразвуку, ефективна густина розсіювачів.

This article analyzes kind of the scattering of ultrasound in thyroid tissues by changing physical parameters due to parenchyma state identified as the concentration of hormones in the blood. As a valuing of the measure of scattering of ultrasound chosen effective density of scatterers, which is measured using elaborated algorithm of thyroid gland ultrasonic images processing.

Keywords: thyroid gland, hormones' concentration, scattering of ultrasound, effective density of scatterers.

Introduction. Mechanical properties of tissues depend on the physiological condition of the thyroid gland and organs that support its functioning. Concentration of hormones leads to a value change of physical properties of soft tissue. This change in turn affects the kind of the ultrasound scattering on tissues investigation. Depending on the density of the location of the scatterers the registered signal used in thwconstruction of ultrasound images is changed. Functional disorder of the thyroid gland can be clearly seen as areas of brightness change in the image. As an index of the kind of ultrasound scattering on the tissue used the parameter of effective density of scatterers (EDS), which characterizes the fluctuation of the brightness of the area of ultrasound images from the norm.

Determination of the EDS allows evaluating the kind of the disease of the patient, knowing the correlation of the parameters of ultrasonic images with known diagnoses. The balance of hormones is broken by diseases of the thyroid gland. The result is hyper- or hyposecretion of a hormone that affects the functional condition of the gland and the condition of its tissues. Ultrasound images can capture such fluctuation of the condition as change of EDS.

Development and discussion. Iodized thyroid hormones include thyroxine (T4) and triiodothyronine (T3). They affect the growth and development of tissues, the total energy expenditure and circulation of almost all vitamins and hormones, including thyroid hormones themselves. Hormones act at cell nucleus, mitochonddria's level (affecting oxidizing exchange) and at the plasma membrane. The number of mitochondria increases with increasing the level of the thyroxin hormone. That is why the physical parameters affect the mechanical properties which changing. This change can be traced by assistance palpation.

Investigation of thyroid gland activity has cascading nature. Thyrotropin-releasing hormone is synthesized and secreted in the hypothalamus. Under its influence thyroid stimulating hormone (TSH) is secreted in anterior pituitary and entered the blood in thyroid gland and stimulates it to synthesis and release of thyroxine and triiodothyronine.

The balance of thyroxine and triiodothyronine content affects the content of substances that cause physical condition of tissues and influence their mechanical properties, for example scattering parameters and bulk modulus.

Using a model of tissue as a set of particles [1], which scatter ultrasound the EDS, can be calculate. For this purpose is defined a ratio of brightness distribution moments of 2-th and 4-th order of parts of the image of the thyroid gland. Moments of the brightness distribution are determined at the program level and then the necessary parameter is calculated.

Area is chosen on monochromatic image to determine this ratio. Every pixel is considered in the chosen area and then their values of brightness are recorded (from 0 to 255). Values of brightness for all pixels is used to calculate brightness distribution moment E of 2nd and 4th order and to calculate a ratio $r_4 = \mathrm{E}\{A^4\}/\left[\mathrm{E}\{A^2\}\right]^2$. Determined ratio allows estimation of EDS:

$$M = \left[2/(r_4 - 2)\right].$$

Ultrasound images of thyroid gland were recorded for each of the surveyed patients. As the thyroid gland is divided into two parts – the left and right and for each part was recorded two projections – longitudinal and transverse, so each patient has four ultrasound B-mode images.

One type of section was taken for correct estimation of the parameter (Fig. 1). There transverse section of thyroid gland image has a small size of area hence in this section we have more measurement errors of EDS than in longitudinal sections.

Calculations were made for the left part of thyroid gland. The EDS is determined on the chosen area on the image, in our case in a rectangle (Fig. 1).

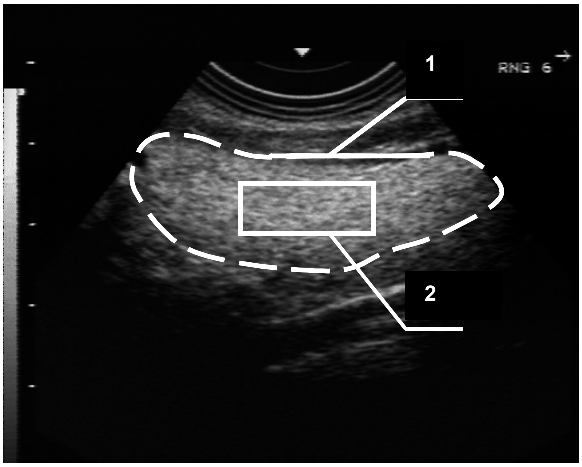

Fig. 1. Longitudinal section of the left part of the thyroid gland
(1 – image of thyroid gland,
2 – the chosen area to calculate the EDS)

Change of functional condition depends on changes of concentrations of hormones. That's why the distribution of dependence between EDS and the concentration of thyroid stimulating hormone was built for three groups of patients: for hyper- , hyposecretion function and normal health.

Results. As input data has been used database of examined patient and was selected 29 patients, including 16 with normal thyroid function and 13 has a function disorder of thyroid gland. This data include information about the concentration of hormones, diagnosis and appropriate ultrasound image of thyroid gland.

The content of hormones depends on gender, so measuring and calculations were performed separately for men and women.

Found that the concentration of triiodothyronine for men by 9% higher than the concentration of this hormone for women (Table 1).

Table 1

Average values of T3 hormones' concentration for men and women and their ratio

<T3 (m)>	<T3 (w)>	<T3(w)>/<T3(m)>	Δ<T3>
1,21	1,10	0,91	9%

Patients with diagnosis of hypothyroidism (thyroid hypofunction secretion of hormones) have a low concentration of hormones T3 and T4 and too much concentration of thyroid stimulating hormone (TSH), which inhibits deiodization from T4 to T3. Otherwise patients with diagnosis of hyperthyroidism (overactivity of secretion of thyroid hormones) have relatively high levels of triiodothyronine and thyroxin and insufficient quantity of thyroid stimulating hormone, which is not enough for normal control of deiodization from T4 to T3 and this is leading to hypersecretion function and production of thyroid hormones.

For each analyzed image were performed five independent measurements of EDS choosing of different rectangular areas within the thyroid gland and recorded five data sets.

The following calculations were carried out with the average value of EDS for each of the images. The average value of error calculations EDS is 4%.

Change of functional condition depends on changes of concentrations of hormones. That's why the distribution of dependence between EDS and the concentration of thyroid stimulating hormone was built for three groups of patients: with hyper- hyposecretion function and healthy.

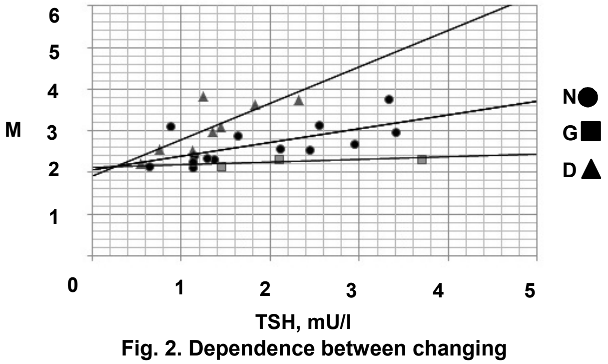

Fig. 2. Dependence between changing of TSH concentration with EDS for:
N – patient with normal condition of thyroid gland,
G – patient with hyposecretion function of thyroid gland,
D – patient with hypersecretion function of thyroid gland

Quantitative assessment of dependence between increasing the EDS with increasing concentrations of TSH allows conclude a linear dependence.

Line with bigger angle corresponds to patients with hypersecretion function of thyroid gland (D), which marked with triangles. A line passing below corresponds to patients with normal thyroid condition (N), which are marked by circles. The lowest line, which passes through the squares, corresponds to patients with hypothyroidism – decreased secretion of hormones (G).

A straight line that corresponds to the normal function of thyroid gland is described by the equation:

$$y = 0{,}33x + 2{,}05 .$$

A straight line that corresponds to the hypothyroidism (reduced secretion of hormones) is described by equation:

$$y = 0{,}06x + 2{,}12 .$$

A straight line that corresponds to the hypersecretion function of thyroid gland is described by equation:

$$y = 0{,}88x + 1{,}90 .$$

It is evident from the Fig. 2 that the straight lines intersect Y-axis in the environment of point M = 2. It is fact minimum value the effective density of scatterers M can assume with the completely no-scattering image which equals to 2. Therefore the straight lines, which characterize linear increase M depending on concentration TSH corresponds to the mathematical maintenance of this of the model [1].

Slope coefficients are correlated with the change of concentration of thyroid stimulating hormone. And the straight line is located by that more abruptly than hypersecretion shows its influence and vice versa (Table 2).

Divergences of the slope coefficients for each straight line do not overlap.

Conclusions. The effective density of thyroid tissue scatterers depends on the concentration of thyroid stimulating hormone which controls the balance of thyroxine and triiodothyronine content and deiodization. The method of statistical evaluation proved that the dependence of the effective density of scatterers of the content of thyroid stimulating hormone is different for the cases of hypo- and hypersecretion thyroid function and is linear for each of the cases.

Table 2

Slope coefficients for thyroid gland state with different concentration

State of thyroid gland	Hyposecretion function	Normal condition	Hypersecretion function
Slope coefficient	0,06	0,33	0,88

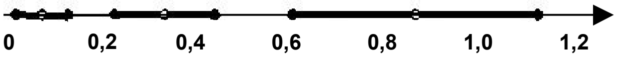

Fig. 3. Divergence of the slope coefficients of the straight lines

1. *Shankar PM.* A model for ultrasonic scattering from tissues based on the K-distribution // Phys Med Biol – 1995 – Vol.40 – P 1633–1649. 2. *Кононов М. В., Радченко С. П., Скрипаченко З.М., Айдоян Г.В.* Застосування оцінок флуктуаційного розсіяння ультразвукових хвиль для класифікації статистично неоднорідних середовищ" // Вісник Вісник КНУ Серія "Фізмат. науки". – 2007. - С 258-262 3. *Туракулов Я.Х., Ташходжаева Т.П.* Внутритиреоидное дейодирование тироксина: влияние ТТГ и денервации щитовидной железы // Проблемы эндокринологии, – 1986 – т32, №5, С 72-76.

Submitted on 18.10.11

UDC 519.9

**O. İl'chehko, post. grad. stud., V. Obukhovsky, Dr. Sci.,
V. Nikonova, post. grad. stud., V. Lemeshko, Ph.D., A. Kutsyk, stud.**

RAMAN SPECTROSCOPY RESEARCH ON COMPLEXATION PROCESSES IN WATER-METHANOL SOLUTIONS

Досліджувались спектри комбінаційного розсіювання для системи метанол-вода при різних концентраціях компонент в спектральному діапазоні 2000-4000 см$^{-1}$. Для аналізу отриманого набору спектрів комбінаційного розсіювання використовувався метод MCR-ALS. В результаті проведеного аналізу було визначено, що найбільш оптимальний опис суміші необхідно проводити з використанням трьохкомпонентної моделі. Отримані результати дозволяють описати структуру розчину метанол-вода. Модель оперує трьома компонентами: метанол, вода і комплекс метанол/вода (1:1). Отримані концентраційні профілі були порівняні з теоретичними підрахунками, що базуються на теорії нелінійної дифузії. Експериментальні і теоретичні результати співпадають в межах похибки експерименту.

Ключові слова: комбінаційне розсіювання світла, нелінійна дифузія, водневий зв'язок, кластер, метод MCR-ALS, концентрація.

Raman scattering spectra of water-methanol systems with various component ratios were detected within the spectral range 2000-4000 cm^{-1}. MCR-ALS analysis was used to decompose the Raman spectra into specific components of different composition. Three components were found necessary to obtain a satisfactory fit to the data. The results allow application of a mixture model to describe the structure of water-methanol solutions. The model consists of three species, namely, methanol, water and complex methanol/water (1:1). Resolved concentration profiles were compared with theoretical calculations based on non-linear diffusion theory. Experimental and theoretical results are in good agreement within the range of measuring error.

Key words: Raman scattering, nonlinear diffusion, hydrogen bond, cluster, MCR-ALS method, concentration.

Introduction. Vibrational spectroscopy provides invaluable information about hydrogen bonding in aqueous solution. Recently, the processes determining the structure of partially ordered liquids such as alcohols [2, 5, 8, 11, 20] are interesting. As a rule, the molecular structure of associates is studied using oscillation spectroscopy [23].

Recent experimental and theoretical methods open a new stage of research in this field. Femtosecond spectroscopy techniques provide information about the time of both rupture and recovery of hydrogen bond [5, 11, 12, 16]. Cluster isolation methods in Ar and He nanodrops gave an opportunity to study clusters of different sizes separately [2, 22]. On the other hand, modern computer programs let us to carry out quantum-chemical calculations and to obtain data of the structure and spectral properties of molecular systems.

The parameters of hydrogen bond in alcohol are close to similar parameters in water. But the alcohol molecules have carbon atoms that do not participate in the formation of H-bond. It allows studying the processes in the medium not only by the oscillatory band of hydroxyl (O-H) but by Raman scattering spectra of vibrations of C-O, C-H bonds. The alcohols are known to form H-bonds of medium power (5–15 kcal / mol) [15].

Despite the fact that a lot of investigations [3, 4, 13, 15, 20] are devoted to the study of properties of water-methanol solutions, the problems of the structural features of these solutions have been still far from resolving.

This article is devoted to investigation of Raman scattering spectra of water-methanol mixtures at different concentrations of components. Studying hydrogen bonds in aqueous solutions at different concentrations of methanol, proving the availability of cluster formations by comparative analysis of Raman scattering spectra of H_2O, CH_3OH and their mixtures were the main aims of the investigation.

Experimental part. The spectral-computation complex on the base of double monochromator system DFS-52 was used in the measuring process. The complex can be conditionally divided on three mail units: the unit of laser excitation, optical and process control units. The flow chart of the complex is shown on Figure 1. The main stages of modernization will be observe in detail.

1. Radiation source. Argon laser LGN-503 was used like an exciting radiation. The power supply unit of the laser works on water cooling system 1. Outside contour of cooling connects with the power supply unit of the laser 2. Inside contour works on the distilled water like a cooling system for active element GL-303B and metal bars of radiation laser unit 3. The type of active element resonator was Littrov prism. It takes a possibility of five wavelength generation: : 457,9 nm, 476,5 nm, 488 nm, 496,5 nm, 514,5 nm. The generation of wavelength 488 nm was used for all investigations. The half-width of wavelength 488 nm was measured in the spectral-computation complex on the base of double monochromator system DFS-52. It is about 1,8 cm^{-1} (Figure 2).

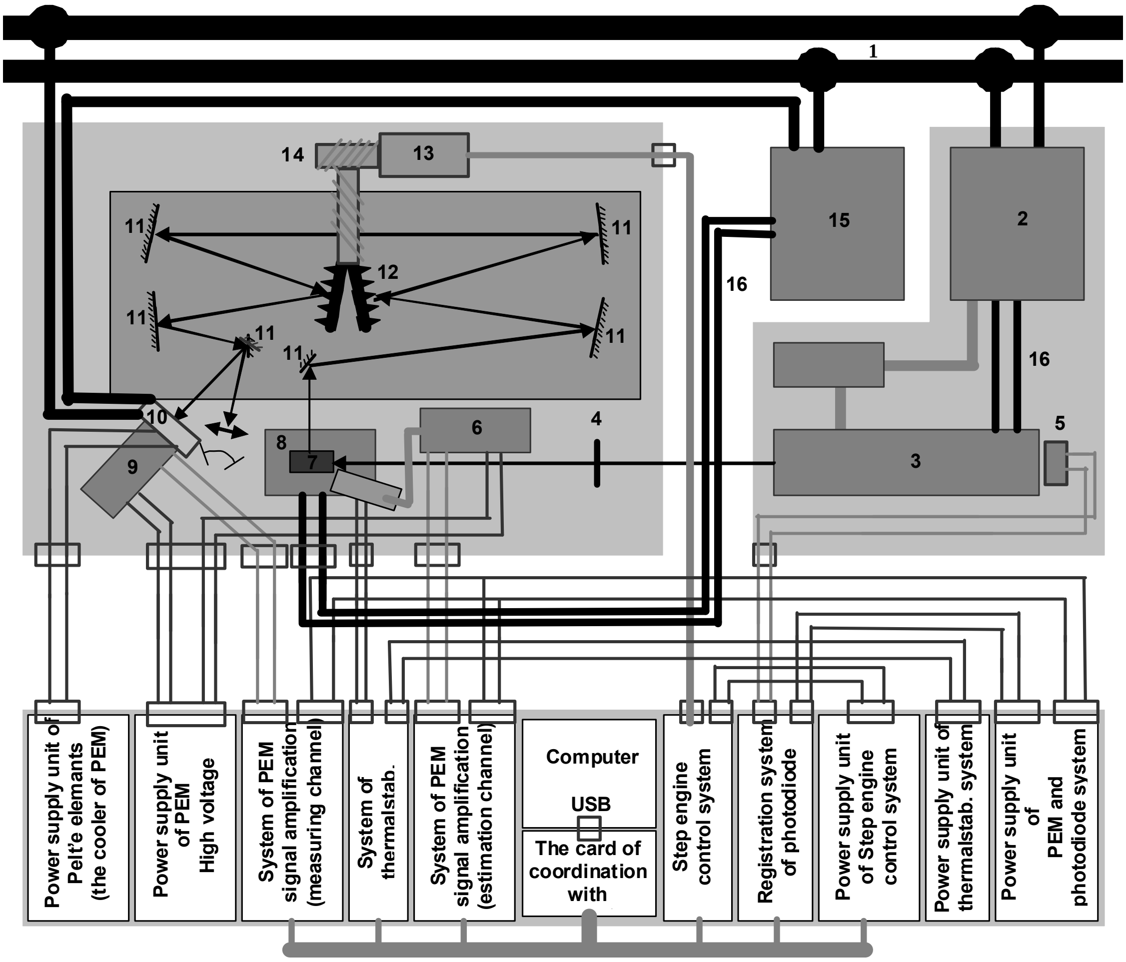

Fig. 1. The flow chart of the complex:
1 – water cooling, 2 – power supply unit of laser LGN-503, 3 – radiation source, 4 – interference filter, 5 – photodiode, 6 – estimation channel PEM-79 (photoelectrical multiply), 7 – ditch, 8 – thermostabilization, 9 - measuring channel PEM-79, 10 – PEM cooling, 11 – double monochromator mirror, 12 – diffraction grid, 13 – step engine, 14 – reducer, 15 – power supply unit of water cooling thermal stabilization system, 16 – water cooling inside contour

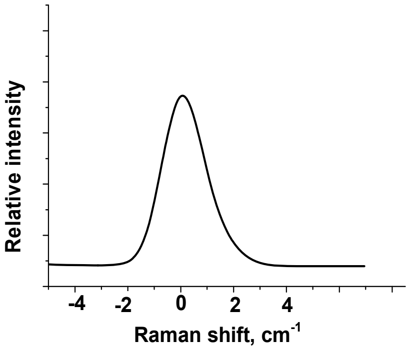

Fig. 2. The spectrum of laser LGN-503 radiation wavelength 488 nm

2. Estimation channel of laser radiation. Two estimation channels were realized in measuring complex.

It's a registration system of photodiode signal (5 on Figure 1) and registration system of PEM signal (6 on Figure 1). Registration system of PEM signal used for measuring the intensity of Relei radiation. The estimation channel with PEM has the imperfection. Raman spectrum of Relei intensity and the intensity of microdust in the sample has non leaner dependence. So it's necessary to use simultaneously two estimation channels. In this case it's possible to get the spectrum which is pure of non stability laser work error and additional microdust error.

3. Samples measuring conditions. Raman spectra of liquids are very sensitive to temperature changing [21]. Consequently the thermal stabilization system was designed (8 on Figure 1). The flow chart of the system is shown on Figure 3. Temperature stabilization is realized with the polarity power changing on Peitier element. The special designed software for the measuring process control was used to control the temperature stabilization. The temperature range of measuring can be varied from -15 ˚C to +100 ˚C. The accuracy of temperature stabilization in a range from +5 ˚C to +40˚C is 0,05˚C and in a range from

15˚C to +5 and from +40˚C to +100˚C is – 0,3˚C. The average temperature of environment is ~ 20˚C. Entering time regime specified accuracy stabilization is about 30–40 min. It's depend of required temperature of stabilization.

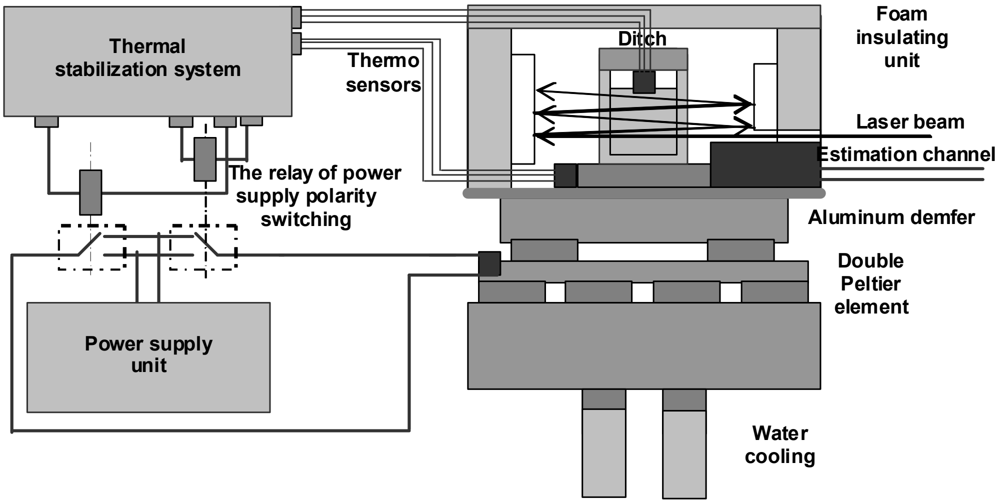

Fig. 3. The flowchart of the thermal stabilization system

There is an optical system (Figure 3) which was used like an amplifier of laser beam intensity and located inside of thermal stabilization unit. It's necessary for the Raman intensity increasing and the increasing of complex resolution respectively.

4. Registration system of Raman intensity. PEM-79 (photoelectrical multiply) was used like a detector of Raman intensity (9 on Figure 1). The cooling system for PEM-79 on forth Peltier elements was realized (10 on Figure 1). During the measuring process the cooling temperature was -10±0,5˚C. The dark noise of PEM was decreased in four times (Figure 4).

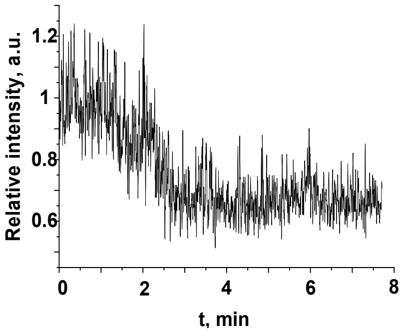

Fig. 4. The dark noise intensity measuring with turn off cooling power (the right part) and turn on cooling power (the left part)

This result was obtained during the dark noise intensity measuring with turn off cooling power (the right part on the Figure 4) and turn on cooling power (the left part on the Figure 4).

The software building Raman scattering spectrum on these data has been designed. Panoramic spectra within the range 2000 ... 4000 cm^{-1} with a spectral resolution of 2 cm^{-1} were recorded when registering a consistent signal. Accumulation time of the spectrum record amounted to a range of 40 minutes. Heating the sample during the measurement of Raman scattering spectra did not practically occur, due to small value of absorption coefficient under excitation frequency. Scattered light is observed at 90° relatively to the direction of incident laser beam. The spectra were recorded with the width of input and output gaps, which did not exceed 200 µ.

MCR-ALS analysis. MCR-ALS analysis was used to decompose the Raman spectra into specific components of different compositions. The MCR-ALS method [18] follows the general form

$$D = CS^T + E \qquad (1)$$

In (1) D is the original Raman data matrix, which contains the methanol solution data, is the matrix of pure concentration C profiles, and S^T is the pure component spectra. E is the matrix of residuals. MCR-ALS solves eq.1 iteratively by an alternating least-squares that calculates C and S^T matrices optimally by fitting the experimental data matrix D. During the ALS optimization, non-negativity, unimodality and closure constraints are applied [19]. Convergence is achieved when relative differences in standard deviations of residuals between experimental and ALS calculated are less than 0.1%.

The MCR-ALS algorithm implemented by Tauler et al. [9] was used to decompose the original Raman spectra matrix of water-methanol solutions into "pure" components and their concentrations. We find that three components are needed to obtain a good fit to the data.

Theory. It is known that the dissolution of one substance in another one is accompanied by the formation of molecular complexes arising due to the intermolecular interaction [1,7]. In the frame of the posed problem, we now consider a mixture of two molecular substances X and Y in the liquid state. The interaction between molecules leads to the formation (with some probability) of complexes of the X^nY^m type (n and m are the numbers of structural units (e.g., molecules) of a certain type in the complex). In what follows, we will consider only the "formation–decay" reactions:

$$nX + mY \to X^nY^m;\ X^nY^m \to nX + mY \qquad (2)$$

Within our model, this kind of a mixture consists of three components: X, Y, and X^nY^m[1].

Chemical reactions (the formation of complexes or associations) result in a local imbalance (the concentrations of individual components are changed) and in the appearance of nonlinear mixing flows. The mutual movement of various components occurs under the preservation of the total volume of a mixture [6,10]. Due to this circumstance, we will work with partial volumes, rather than with concentrations. Under this approach, the diffusion is described by next laws [6,17]:

---

[1] The real solutions can contain molecular complexes of different compositions. We will interpret the numbers n and m as the mean (effective) numbers for corresponding structural units in the complexes.

– equations of continuity

$$\frac{\partial M_i}{\partial t} + div\vec{j} = S_i \qquad (3)$$

– nonlinear diffusion flows

$$\vec{j}_i = \sum_j d_{ij}[M_j \nabla M_i - M_i \nabla M_j] \qquad (4)$$

Here the following notation were used: the indices i, j numerate the components of the liquid mixture; M_i – volume fraction of components i ("partial volume"); $\vec{j}_i$ volume's flow of i-substance; S_i – function of sources, which depend on the processes of i-component birth (decay); d_{ij} mutual diffusion coefficients, that forms matrix $\{d_{ij}\}$.

The preservation of conditions of the substance and the volume are determined by three integrals of motion (conservation laws):

$$\sum_i M_i = 1, \ \sum_i \vec{j}_i = 0, \ \sum_i S_i = 0 \qquad (5)$$

Reaction (2) determines the form of functions S_i (sources):

$$S_1 = \beta_1 M_3 - \alpha_1 M_1^n M_2^m,$$
$$S_2 = \beta_2 M_3 - \alpha_2 M_1^n M_2^m, \qquad (6)$$
$$S_3 = -(S_1 + S_2)$$

Below it is supposed the chemical reactions proceed quickly, but the spatial mass transfer – slowly. It corresponds to condition

$$S_i \cong 0 \qquad (7)$$

It means that diffusion occurs when local chemical equilibrium has been took place. In this case it follows from (5):

$$M_3 \cong \gamma M_1^n (1 - M_1 - M_3)^m, \ (\gamma = \frac{\alpha}{\beta}) \qquad (8)$$

Under diffusion process molecules are transported both individually and as part of complexes [$X^n Y^m$]. The total flux of matter X (measurable in experiments) [14]:

$$\vec{j}_1^{total} = -D_1^{ef}(M_1^{total}) \nabla M_1^{total} \qquad (9)$$

Where M_1^{total} – volume fraction of substance X (in free and bound state), D_1^{ef} – effective coefficient of diffusion. According to [14] the last can be found as:

$$D_1^{ef}(M_1^{total}) = \frac{(d_{12} - q_{11}M_3) + \frac{\partial M_3}{\partial M_1}(\eta d_{23} + q_{11}M_1)}{1 + \eta \frac{\partial M_3}{\partial M_1}}, \qquad (10)$$

where $\frac{\partial M_3}{\partial M_1} = \frac{M_3[n(1 - M_1 - M_3) - mM_1]}{M_1(1 - M_1 - M_3 + mM_3)}$; $\eta = \frac{n\Delta V_1}{n\Delta V_1 + m\Delta V_2}$ – volume fraction of substance X in complex; $q_{11} = (d_{12} - d_{13}) + \eta_1(d_{13} - d_{23})$.

The result (9) describes the diffusion in the liquid mixture with components X, Y, $X^n Y^m$. Material parameters of this system are the following: α_n, β_n, d_{nm}, ΔV_n.

Results and Discussion. Raman scattering spectra were detected in spectral range from 2000 to 4000 cm^{-1} (bands of stretching vibrations of CH- and OH-groups) for solutions with different methanol concentrations from pure water to pure methanol (Figure 5). The temperature of liquid samples was within the range 293 K. We devote special attention to behavior of the OH stretching band in water-methanol solutions due to the fact that the contour of this band is essentially affected by hydrogen bonding.

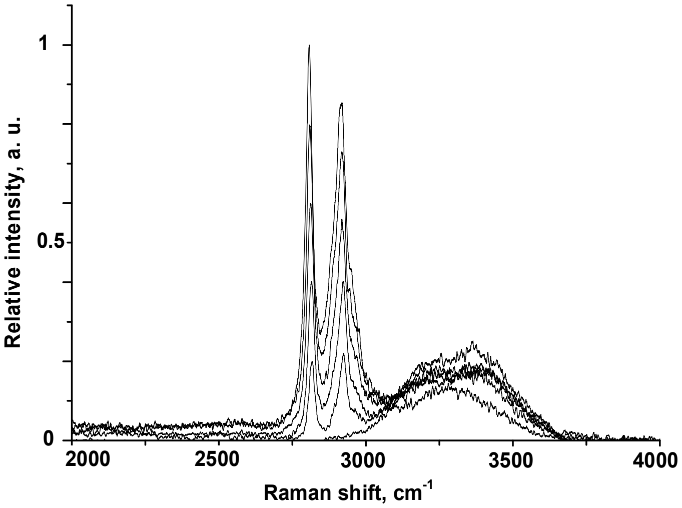

Fig. 5. Raman scattering spectra of water-methanol solutions with different component ratios.

MCR-ALS analysis. Our approach is based on a three-component MCR-ALS analysis of the Raman spectra of water-methanol solutions. The results on the resolved Raman spectra (S^T) and the concentrations (C) are shown in Figure 6. By comparing the resolved spectra (Figure 6, right) to the spectra of water-methanol solutions (Figure 5), the "pure" components have been identified as water, methanol hydrate ($CH_3OH{\cdot}H_20$) and methanol. The maximum of hydrate concentration is about 60 vol. % at 50 vol. % of pure methanol concentration.

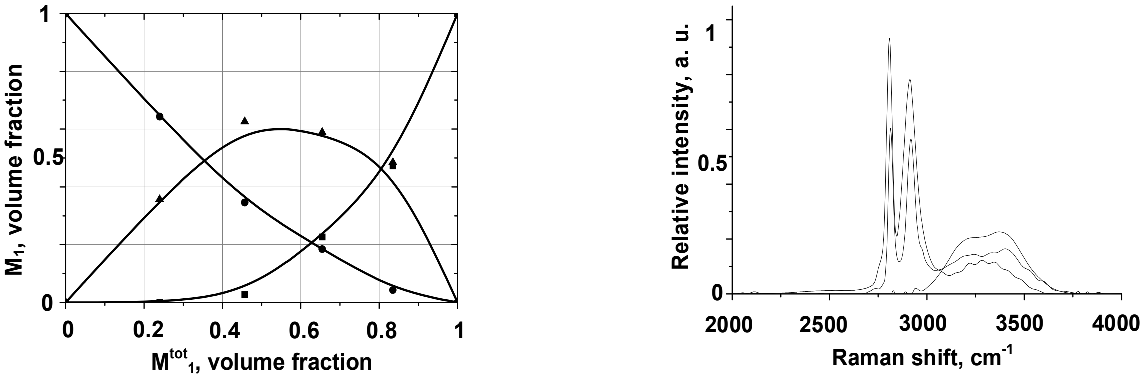

Fig. 6. Spectra (top figure) and concentration profiles (down figure) of "pure" components obtained by MCR-ALS analysis (circles, squares, trianglesindicate H_20, CH_3OH and $CH_3OH \cdot H_20$ respectively).

Analysis of diffusion in water-methanol mixture. The modified system of diffusion equations (3-6) was applied to analyze the mass transfer processes in a liquid water-methanol mixture. These substances are mutually soluble completely. According to (9) theoretical curve was calculated numerically. From the condition of the best agreement of theoretical curve with experimental results [23], the following material parameters were found:

$$n = 1/3, \quad m = 1/3, \quad d_{12} = 0.15, \quad d_{13} = 2.13,$$

$$d_{23} = 1.48, \quad \eta = 0.69, \quad \gamma = 1.39. \qquad (11)$$

Parameters (11) permit to find the concentration of molecular complexes.

Comparison. We compared the resolved concentration profiles with theoretical calculated ones. The result of comparison is shown in Figure 7.

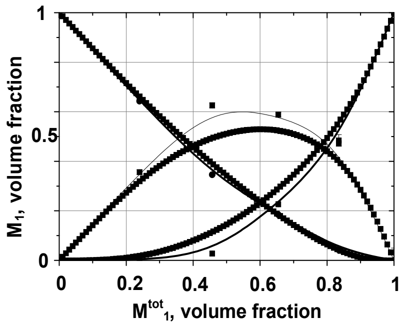

Fig. 7. The result of comparison of resolved concentration profiles and theoretical calculated ones.

Experimental and theoretical results are in good agreement within the range of measuring error.

Conclusions. The analysis of Raman spectra at different methanol concentrations in water-methanol system using MCR-ALS method was carried out. It can give very necessary information about complexacion processes in this mixture. Three components model the description of the model was chosen. Concentration profiles and modeling Raman spectra of mixture components were obtained. The effective (average) hydrate type was determined as 1:1.

Three components model of the mixture was used successfully for diffusion process description for one hydrate type only. The theoretically calculated average hydrate type was 1:1. It's the same result, which was obtained using MCR-ALS method for Raman spectra. The component concentrations were obtained using the material parameters from the theory.

Theoretical calculated concentration profiles are in good correlation with the experimental results.

1. Пиментел Джордж, К. Мак-Клеллан, Обри Л. Водородная связь. – М.: Мир – 1964. – 462 с. 2. Buck U., Huisken F. Infrared spectroscopy of size-selected water and methanol clusters // Chem.Rev. – 2002. – Vol.100, N 11. – P.3863-3890. 3. Cleveland D., Carlson M., Hudspeth E.D., et al. Raman Spectroscopy for the Undergraduate Teching Laboratory: Quantification of Ethanol Concentration in Consumer Alcoholic Beverages and Qualitative Identification of Marine Diesels Using a Miniature Raman Spectrometer // Spectrosc. Lett. 2007. Vol. 40. Iss 6. P. 903-924. 4. Egashira K., Nishi N. Low-Frequency Raman Spectroscopy of Ethanol-Water Binary Solution: Evidence for Self-Association of Solute and Solvent Molecules // J. Phys.-Chem. B. 1998. Vol. 102. № 21. P. 4054-4057. 5. Gaffney K., Davis P., Piletic I. et al. // Hydrogen bond dissociation and reformation in methanol oligomers following hydroxyl stretch relaxation // J.Phys.Chem. A. – 2002. – Vol.106, N 50. – P.12012-12023. 6. Yu.V. Gridneva, V.V. Obukhovsky, Visn. Kyiv. Univ.No. 3, 284 (2003). 7. E.S. Gyulnazarov, V.V. Obukhovsky, T.N. Smirnova. Theory of holographic recording on a photopolymerized material //SPIE "Milestone Seria". – 1996. – 130. – P. 473-475. 8. Handgraaf J.-W., van Erp T.S., Meijer E.J. Ab initio molecular dynamics study of liquid methanol // Chem.Phys.Lett. 367(2003) P.617. 9. J. Juamot, R. Gargallo, A. de Juan, R. Tauler // Chemometrics and Intelligent Laboratory Systems. – 2005, Vol.76 – P.101-110. 10. G.M. Karpov, V.V. Obukhovsky, T.N. Smirnova, andV.V. Lemeshko, Opt. Comm. 174, 391 (2000). 11. Laenen R., Gale G.M., Lascoux N. IR spectroscopy of hydrogen-bonded methanol: vibrational and structural relaxation on the femtosecond time scale. // J.Phys.Chem. A. - 1999. - Vol.103, N 50. - P.10708-10712. 12. Mukamel S., Zhuang W. Coherent femtosecond multidimentional probes of molecular vibrations // PNAS.– 2005.– Vol.102, N 39 .– P.13717-13718. 13. Nose A., Hojo M. Hydrogen bonding of water-ethanol in alcoholic beverages // J. of Bioscience and Bioengineering. 2006. Vol. 102. 14. V.V. Obukhovsky, V.V. Nikonova, Visn. Kyiv. Univ. No. 4, (2009). 15. Pimentel J., McClellan O. The Hydrogen bond / Freeman, San Francisco & London., 1960. 16. Tanimura I.I., Mukamel S. Two-dimensional femtosecond vibrational spectroscopy of liquids // J. Chem. Phys. – 1993. – Vol.99. – P. 9496-9511. 17. Yu.B. Rumer and M.Sh. Ryvkin, Thermodynamics, StatisticalPhysics, and Kinetics (Nauka, Moscow, 1977) (inRussian). 18. R. Tauler, B. Kowalski // AnalyticalChemistry. – 1993, Vol. 65 – P.2040-2047. 19. A. deJuan, R. Tauler // AnalyticaChimicaActa. – 2003, Vol. 500 – p.195-210. 20. Sanford C.L., Mantooth B.A., Jones B.T. Determination of Ethanol in Alcohol Samples Using a Modular Raman Spectrometer // J. Chem. Educ. 2001. Vol. 78. P. 1221-1225. 21. Scherer, J. Raman spectra and structure of water from -10 to 90° /J. Scherer, K. Go, S.Kint // Physical chemistry. – 1974. – Vol. 78. – №13.– P. 1304–1313. 22. Toennies J.P., Vilesov A.F. Superfluid helium droplets: a uniquely cold nanomatrix for molecules and molecular complexes // Angew. Chem. Int. Ed. - 2004. - Vol.43. - P.2622-2648. 23. I. M. J. J. Van de Ven-Lucassen, F. G. Kieviet, P. J. A. M. Kerkhof J. Chem. Eng. Data, 1995, 40 (2), P. 407–411.

Submitted 07.10.11

UDC 537.8.029.6, 538.97-405, 548:537.621

V. Kostenko, deputy director, A. Sorochak, trainee
T. Chamor, Ph.D, L. Chevnyuk, Ph.D

MICROWAVE AND MAGNETIC PROPERTIES OF ALUMINUM SUBSTITUTED BARIUM HEXAFERRITE

В роботі досліджені високочастотні характеристики резонаторів мм-діапазону з монокристалічного об'ємного матеріалу $BaFe_{11.1}Al_{0.9}O_{19}$ та епітаксійних плівок барієвого гексафериту заміщеного алюмінієм. Показано, що модовий склад спектру манітостатичних коливань (МСК) монокристалічного резонатора з $BaFe_{11.1}Al_{0.9}O_{19}$ при насиченні та в області багатодоменності (випадок ЦМД) помітно відрізняється від резонаторів з $BaFe_{12}O_{19}$. Особливо ця відмінність помітна при насиченні, де для резонатора з заміщеного гексафериту експериментально спостерігалася значно інтенсивніша основна мода ω_0 у порівнянні з вищими модами МСК. Мода (1,1,0) обчислена теоретично в магнітостатичному наближенні на експерименті не спостерігається. Показано, що в результаті заміщення алюмінію, поле анізотропії На в монокристалічних резонаторах при тому ж параметрі заміщення вище ніж у епітаксіальних плівках.

Ключові слова: магнітостатична мода, хвилі мм-діпазону, заміщення, барієвий гексаферит, монокристал, епітаксійна плівка.

High-frequency characteristics of mm-range resonators produced from bulk single-crystal material $BaFe_{11.1}Al_{0.9}O_{19}$ and epitaxial films of barium hexaferrite doped with aluminium have been investigated in this study. It was shown that the composition of magnetostatic (MS) oscillations modes spectrum of the single-crystal resonator from $BaFe_{11.1}Al_{0.9}O_{19}$ in a saturated state and in multidomain area (a case of cylindrical magnetic domain (CMD)) notably differs from resonators of $BaFe_{12}O_{19}$. Especially this difference is evident in a saturated state, when for the substituted hexaferrite resonator a more intensive fundamental mode ω_0 compared with higher MS oscillation modes has been experimentally observed. The mode (1,1,0) was theoretically calculated in the magnetostatic approximation and was not observed experimentally. As a result of aluminium substitution is that the anisotropy field H_a in single-crystal resonators, with the same parameter of substitution, is higher than in epitaxial films.

Keywords: magnetostatic mode, millimeter wave, substitution, barium hexaferrite, single-crystal, epitaxial film.

Introduction. Due to the high value of intrinsic crystallographic anisotropy field H_a the spectra of MS oscillations of resonators based on pure uniaxial hexaferrites can be obtained in broad band 40-60 GHz for relatively small values of biasing magnetic fields H_0=0-10 kOe. This, in the first place, promises their application to be prospective for spin-wave electronic devices in mm-band [11]. One more advantage of hexaferrite materials – the possibility to obtain as the epitaxial films [9,12].

Considerable advances have been made recently [10,7,4] in the experimental observation of the spin oscillations spectra behaviour for single domain and multidomain areas in mm-band resonators based on substituted uniaxial hexaferrites. Separately, it should be noted that there is a real opportunity to increase operating frequencies (over 100 GHz) of hexaferrite resonators substituting iron atoms (Fe^{3+}) with aluminum atoms (Al^{3+}). Considering this circumstance, the advancement of such researches are very important for the problems of modern radiophysics.

Results of experimental investigations of FMR spectra of Al-substituted strontium hexaferrite plateletlet ($SrFe_{11.2}Al_{0.8}O_{19}$), carried out in wide range of fields H_0=0-7 kOe, were published for the first time in [2]. Analogous investigations on a series of uniaxial $BaAl_xFe_{12-x}O_{19}$ specimens with substitution parameter x ranged from 0 to 2 have been carried out in [10]. In this research FMR frequency-field dependences in domain area were obtained only for the low-frequency branch ω_1 [8], as well as for FMR fundamental mode ω_0 in saturation [10]. The fact of the existence of higher types of MS oscillations in the saturated area, except sufficiently intensive mode ω_0, don't reported in [10].

Five MS oscillations modes in saturation with good intensity were experimentally observed when rectangular plateletlet of high quality $BaFe_{12}O_{19}$ with normal biasing magnetic field has been investigated [5].

Experimental results and analysis. In this study, we report results of experimental investigations MS excitation spectra in normally biased specimen of Al-substituted barium hexaferrite ($BaFe_{11.1}Al_{0.9}O_{19}$) with created CMD structure in initial state (Fig.1). The investigations were carried out by the method of measuring of high-frequency spectra in domain and saturation areas. A specimen was made in the form of rectangular plateletlet a×b=1.42×1 mm^2 in size, cut from single-crystal material $BaFe_{11.1}Al_{0.9}O_{19}$, with magnetic easy axis (EA) perpendicular to the platelet surface. The ferrite specimen was pasted-in thin (100 microns) quartz platelet in order to make it mechanically durable. Later, edges of the platelet were carefully polished for achieving conditions of the best excitation of MS oscillations modes in saturation.

Numerous calculations for investigated specimen were carried out in the same way as for the plateletlet of pure barium hexaferrite which was investigated in [5]. Thus, we made more complete quantitative experimental verification of the results of theories in [8,1] developed in magnetostatic approximation. It is worth to mention that in this case, as in [5], there are good agreement between calculation and experimental data (Fig. 1).

All the spectrum of exitated modes of the $BaFe_{11.1}Al_{0.9}O_{19}$ specimen (Fig. 1.), in both physically different (multidomain and saturated) states, has raised to frequency on the amount of the difference $\gamma(H_a' - H_a)$ relatively to spectrum of modes of pure $BaFe_{12}O_{19}$ [5]. We noticed the important fact that in the absence of H_0 the value of the difference between high-frequency modes $\omega_3 - \omega_2 \approx 6.5$ GHz, for the specimen of pure $BaFe_{12}O_{19}$ [5], diminishes almost doubly $\omega_3 - \omega_2 \approx 3.32$ GHz for the investigated substituted $BaFe_{11.1}Al_{0.9}O_{19}$ specimen. It is seen from Fig.1 that theoretical results, used for calculations and represented in [8], almost exactly have foreseen and described such a behaviour of branches ω_2, ω_3 and once more have assured us that practical application of this theory for single-crystal M-type hexaferrite is good. It also follows from this that if we know resonance frequencies of MS modes for CMD structure, even with absence of external biasing field H_0 , we get the possibility to determine unambiguously such important parameters of these ferrites as H_a and M. In contrast to the specimen of pure $BaFe_{12}O_{19}$ [5,11], in the experimental spectrum of the excitation of MS modes in saturation for $BaFe_{11.1}Al_{0.9}O_{19}$ plateletlet we registered only two initial modes (Fig. 1, Fig. 2).

The calculation of MS modes for the investigated rectangular $BaFe_{11.1}Al_{0.9}O_{19}$ plateletlet with *a* and *b* sides, biased perpendicularly in saturated area, was fulfilled in magnetostatic approximation and was considered in [1]. The theoretical frequency of uniform ferromagnetic resonance was calculated for the specimen which was formed as a platelet with its EA||H_0 perpendicular to the surface and does not coincide with the theoretically obtained lowest MS mode (1,1,0) for the same orientation of H_0 (Fig. 1). Therefore, both in the case with the rectangular plate of pure $BaFe_{12}O_{19}$ [5] and in the case of our this research the lowest experimental mode in saturation is identified as ω_0 mode, but not as (1,1,0). This very interesting physical fact needs further experimental and theoretical research for entire understanding of the excitation nature of MS oscillations in resonators based on bulk hexaferrite.

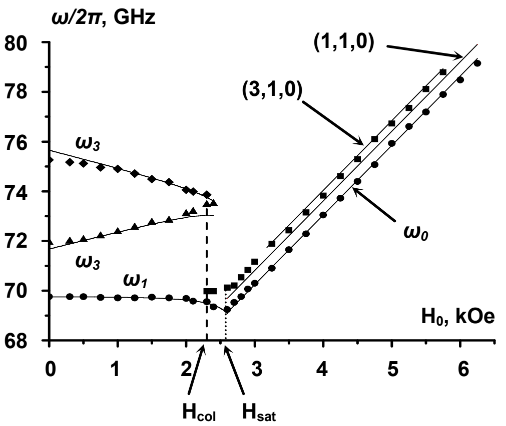

Fig. 1 Frequency-field dependence of MS oscillations in single-crystal $BaFe_{11.1}Al_{0.9}O_{19}$ plateletlet with CMD in initial state. t_f=41 μm, a×b=1.42×1 mm², H_a=24.94 kOe, M= 0.227 kGs. Dotted line – experiment, solid lines – calculated curves

The amplitude distribution of absorption resonance of investigated specimen, as one can see in Fig. 2, does not have slowly descending character. This is not typically for high quality rectangular $BaFe_{12}O_{19}$ specimens [5,6].

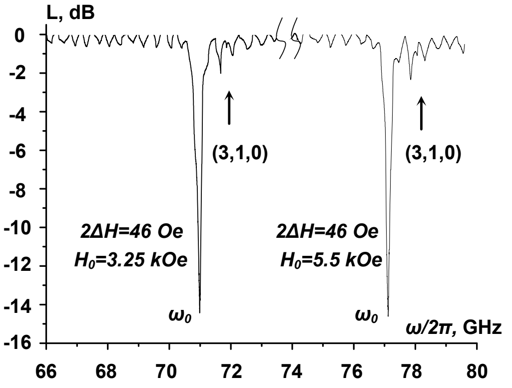

Fig. 2. Experimental spectrum of absorption resonance lines of the plateletlet, same as represented in Fig. 1, for two values of H_0 in saturation

The fundamental mode ω_0 becomes excited more efficiently than (3,1,0) mode. So, FMR linewidth of fundamental mode – $2\Delta H \approx 50$ Oe, is close to data of $2\Delta H$ for high quality film materials on basis of barium hexaferrite [3,4]. We note that in epitaxial films only a uniform FMR mode is observed [3,6].

In regard to possible existence of forward volume MS oscillations (FVMSO) above the mode (3,1,0) we cannot to identify them because they have very small intensity as one can see in Fig. 2. Practically the same experimental situation has been observed in single single-crystal $SrFe_{11.2}Al_{0.8}O_{19}$ plateletlet [2]. So, the analysis of obtained results allows in some way to assume that for Al substituting in a barium hexaferrite notably influences on the formation of higher types of MS oscillations. It is important to carried out a comparative analysis of obtained magnetic parameters of rectangular single-crystal $BaFe_{11.1}Al_{0.9}O_{19}$ specimen with analogous parameters for epitaxial films with appropriate level of aluminum substitution.

In Fig. 3 we represent the experimental dependence of the influence of the substitution parameter x on the value of field H_a for epitaxial barium hexaferrite films. Its behaviour does not differ substantially from the dependence obtained in [4]. These films were grown on strontium hexagallate (SHG) substrate with 400 μm thick and the ferrite film thickness was 3-8 μm. At that figure, on the H_a dependence is plotted a point (round) which corresponding to the value of H_a of single-crystal $BaFe_{11.1}Al_{0.9}O_{19}$ plateletlet investigated above.

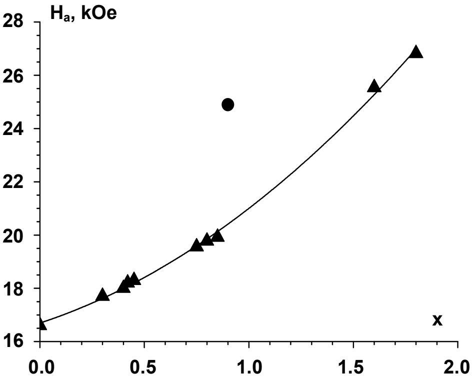

Fig. 3. The dependence of the value of uniaxial anisotropy field H_a versus x for epitaxial films $BaFe_{12-x}Al_xO_{19}$. The value H_a for single-crystal $BaFe_{11.1}Al_{0.9}O_{19}$ plateletlet is plotted as separate round point

As one can see in Fig. 3, the experimental data are well approximated by the functional dependence that can be written as:

$$H_a = 16.7 + 2.54x + 1.75x^2$$

The influence of the substitution in bulk single-crystal with the same parameter substitution considerably differs from epitaxial films. So, FMR linewidth for single-crystal specimen is $2\Delta H \approx 42$ Oe and for epitaxial film is $2\Delta H \approx 150$ Oe [4]. From Fig. 3 one can see that the H_a value for epitaxial film is 5.3 kOe less and that arouses interest to the origin of such difference. As known, in the case with specimens of epitaxial films and bulk single-crystals of unsubstituted $BaFe_{12}O_{19}$ this difference in practice does not exceed 0.5-1 кЕ and in the best specimens of epitaxial films the value $2\Delta H$ almost coincides [12]. One of possible origins of this phenomenon is the presence of magnetoelastic interactions in the film-substrate structure as well as obtaining sometimes film materials with low quality because the imperfect technology of their growth.

Conclusion.

1. It was ascertained experimentally that in barium hexaferrite rectangular specimens doped with aluminium only the intensive mode ω_0 in saturation area has been observed. So, the substitution of Fe atoms by Al atoms notably influences on the excitation of higher types of MS oscillations.

2. It was shown that for rectangular resonators basis on pure and substituted hexaferrites the coincidence of the lowest experimental MS mode with the calculated mode of uniform FMR ω_0 takes place. At the same time the mode (1,1,0) calculated in magnetostatic approximation was not observed.

3. The investigation of magnetic spectra for the substituted epitaxial film $BaFe_{12-x}Al_xO_{19}$ and single-crystal $BaFe_{11.1}Al_{0.9}O_{19}$ plateletlet has shown that for single-crystal specimen FMR linewidth is $2\Delta H \approx 42$ Oe and for the epitaxial film $2\Delta H \approx 150$ Oe. The value of anisotropy film in epitaxial film is 5.3 кЕ less and the additional experimental research is needed to find out the origin of such differences.

1. *Akhiezer, A.I., Bar'yakhtar, V.G., and Peletminskii, S.V., Spinovye volny (Spin Waves), Moscow: Nauka, 1967.* 2. *Chamor T. G., Chevnyuk L. V., Kostenko V. I., Romanyuk V. F., Sorochak A. M.* Reversal magnetization process in the monocrystalline samples of strontium hexafferite // 18th Int. Crimean Conference "Microwave & Telecommunication Technology" (CriMiCo'2008), Sevastopol, – 2010. – P. 554-555. *3. Harris V. G., Geiler A.,* et al. Recent advances in processing and applications of microwave ferrites // J. Magn. Magn. Mater. 2009. Vol. 321. No. 14. P. 2035-2047. *4. Kostenko V. I., Chamor T. G, Chevnyuk L. V.* Ferromagnetic resonance in epitaxial films of Al-substituted barium hexaferrites // Ukr. J. Phys. – 50, № 3. – P. 265-267. 5. *Kostenko V.I., Sorochak A.M., Chamor T.G., Chevnyuk L.V.* Magnetostatic spectra in rectangular platelet of barium hexaferrite in the normal biasing mode // New in magnetism and magnetic materials (NMMM): Materials of XXI Int. Conference. Moscow. – 2009. – P. 895-897. 6. *Kostenko V.I., Sorochak A.M., Nechyporuk O.Yu., Chevnyuk L.V., Chamor T.G.* Investigation of barium hexaferrite FMR amplitude-frequency characteristics in saturated area // IX International Young Scientists' Conference on Applied Physics, Kyiv, June 17-20 2009, p. 13. *7. Popov A., Zavislyak I., Ustinov A., Srinivasan G.* Sub-Terahertz Magnetic and Dielectric Excitations in Hexagonal Ferrites // IEEE Trans. On Magn. – 2011. – Vol. 47, № 2. - P. 289-294. *8. Sigal M. A., Kostenko V. I.* Magnetostatic modes in a thin uniaxial plateletlet with bubble lattice at normal magnetization // Phys. Stat. Sol (a). – 1991. – Vol. 128, № 1. – P. 219-234. *9. Shagaev V. V.* Effect of the substrate on the ferromagnetic resonance linewidth in barium ferrite films // Tech. Phys. – 2008. – vol.53, № 3. – P. 353-356. 10. *Ustinov A. B., Tatarenko A. S., Srinivasan G., Balbashov A. M.* Al substituted Ba-hexaferrite single-crystal films for millimeter-wave devices // J. Appl. Phys. – 2009, Vol. 105, №. 2, P. 023908. 11. *Vizard D. R.* Millimeter-wave applications: From satellite communications to security systems // Microw. J., – 2006. vol. 49. - P. 22–36. 12. *Zavislyak I. V., Kostenko V. I., Chamor T. G, Chevnyuk L. V.* Ferromagnetic resonance in epitaxial films of uniaxial barium hexaferrites // Tech. Phys. – 2005. – 50, № 4. – P. 520-522.

Submitted on 05.11.11

UDC 537.6/.8

G. Melkov, Dr. Sci., D. Slobodianiuk, post grad. stud.

PARALLEL PUMPING THRESHOLD IN FERROMAGNETIC ELLIPSOID

Theoretical expression for parametric parallel pumping threshold in ferromagnetic ellipsoid is obtained. Result summarizes previous results.

Key words: ferromagnetic ellipsoid, ferromagnetic resonance, parallel pumping.

В роботі отримано вираз для порогу параметричної накачки в намагніченому феромагнітному еліпсоїді. Одержана формула узагальнює попередньо одержані для даного випадку.

Ключові слова: феромагнітний еліпсоїд, феромагнітний резонанс, паралельна накачка.

Introduction. In ferromagnetic samples it is possible to excite different types of oscillations and waves. Nonlinearity of Landau-Livshitz equation leads to their coupling hereby determining different nonlinear effects. One of the major effects is parametrical excitation effect when one type of oscillation or waves excites another one after some threshold.

There are several possible mechanisms of such excitation. First of all external magnetic field can transmit energy to inform precision mode of a sample. Due to mentioned above nonlinearity of Landau-Livshitz equation spin system of a sample manifest some nonlinear effects, thus uniform precision and spin-waves are connected. Due to this it is possible to pass energy from uniform precision mode to spin-waves, and after some threshold, when energy income will cover dissipation loses cause their instability. In this case external varying excitation field if transverse to saturation magnetization thus this effect is called perpendicular pumping.

Another possibility is realized when external varying magnetic field directly excites spin-waves. In [3] Schlömann E., Green J.J., and Milano U. detected threshold absorption of electromagnetic energy by the ferromagnetic sample in varying external magnetic field parallel to constant external magnetic field. This effect is caused by spin-waves instability under external electromagnetic pumping, so-called parametric excitation under parallel pumping.

The goal of this work is to obtain an expression for parallel pumping threshold in ferromagnetic ellipsoid. Typically such expressions were obtained in a case of radial symmetry of the sample. In our work general case of unequal demagnetization factors will be considered. Thus obtained results will be general and will cover wide range of sample forms.

Theory. Initial equation is Landau-Livshitz equation [1;2]

$$\frac{\partial \mathbf{M}}{\partial t} = -\gamma\left[\mathbf{M}\times\mathbf{H}\right], \tag{1}$$

where $\mathbf{M}$ is magnetization and $\mathbf{H}$ total effective magnetic field applied to a sample. Assuming that $\mathbf{H} = H_0\mathbf{z} - \mathbf{N}\mathbf{M_0} + \mathbf{h_e} - \mathbf{N}\mathbf{m_0}$ where H_0 external constant magnetic field, $\mathbf{h_e}$ - external varying pumping field, $\mathbf{M_0}$ – saturation magnetization, $\mathbf{m_0}$ – dynamic magnetization and $\mathbf{N}$ – demagnetization factor tensor. We haven't included any dissipation term in equation (1) because it is convenient to introduce dissipation later if final equations.

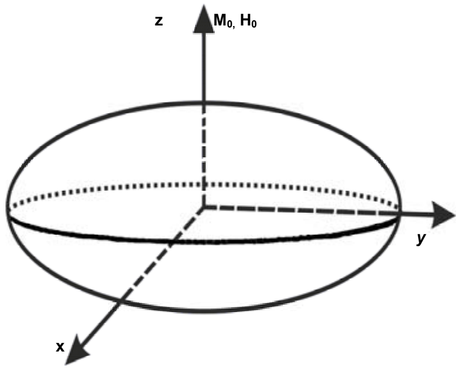

Fig. 1. The geometry of a model.
External constant magnetic field H_0 is parallel to z axis.

Assuming that $\mathbf{m_0} << \mathbf{M_0}$, $\mathbf{h_e} << H_0$ substituting expression for $\mathbf{H}$ into equation (1) one can get:

$$\frac{\partial \mathbf{m_0}}{\partial t} = -\gamma\left[-\mathbf{M_0}\times\mathbf{N}\mathbf{m_0} + \mathbf{M_0}\times\mathbf{h_e} + \mathbf{m_0}\times\mathbf{z}H_0 - \mathbf{m_0}\times\mathbf{N}\mathbf{M_0}\right] \tag{2}$$

Projecting equation (2) into coordinate axes and keeping only first order of vanishing terms we obtain next system:

$$\begin{aligned} \frac{\partial m_{0x}}{\partial t} &= -\gamma\left[M_0N_y m_{0y} - M_0h_{ey} + m_{0y}H_0 + m_{0y}h_{ez} - m_{0y}N_zM_0\right] \\ \frac{\partial m_{0y}}{\partial t} &= -\gamma\left[-M_0N_x m_{0x} + M_0h_{ex} - m_{0x}H_0 - m_{0x}h_{ez} + m_{0x}N_zM_0\right] \end{aligned} \tag{3}$$

Here we assumed that chosen coordinate system (see Fig.1) match with demagnetization tenzor $\mathbf{N}$ normal coordinates, thereby:

$$\mathbf{N} = \begin{pmatrix} N_x & 0 & 0 \\ 0 & N_y & 0 \\ 0 & 0 & N_z \end{pmatrix} \tag{4}$$

The next step is switching from real pares of variables $\left(m_{0x}, m_{0y}\right)$ and $\left(h_{ex}, h_{ey}\right)$ into following complex variables

$$a_0 = \frac{m_{0x} - im_{0y}}{M_0} \qquad h_{e-} = h_{ex} - ih_{ey} \tag{5}$$

Physical meaning of these variables is next: they represent left or right procession depending on a sight near complex unit.

After this transformation system (3) takes a form:

$$\frac{\partial a_0}{\partial t} = -i\omega_H a_0 - i\gamma M_0\left[-N_y\frac{a_0^* - a_0}{2} + N_x\frac{a_0 + a_0^*}{2}\right] \qquad (6)$$
$$+ i\gamma h_{e-} - i\gamma h_{ez}a_0 + \gamma N_z i a_0 M_0,$$

where $\omega_H = \gamma H_0$. After some transformation we obtain:

$$\frac{\partial a_0}{\partial t} = -i\left[A_0 a_0 + B_0 a_0^*\right]a_0 + i\gamma h_{e-} - i\gamma h_{ez}a_0, \qquad (7)$$

where $A_0 \equiv \omega_H - \gamma N_z M_0 + \gamma N_y M_0 / 2 + \gamma N_x M_0 / 2$ and

$B_0 \equiv \gamma M_0\left(N_x - N_y\right)/2$ for simplicity.

Now it is essential to make one more transformation to obtain equation for uniform precession mode of an ellipsoid. This transformation is a classical analog of the third Holstein-Primakoff transformation. In fact it is a well know Bogolubov transformation [1] in a form:

$$\begin{aligned} a_0 &= u_k c_0 + v_k c_{-k}^* \\ a_0^* &= v_k^* c_0 + u_k c_0^* \end{aligned}. \qquad (8)$$

Transformation parameters u_k, v_k are

$$\begin{aligned} u_k &= \frac{1}{\sqrt{2}}\sqrt{\frac{A_0}{\omega_0} + 1} \\ v_k &= -\frac{1}{\sqrt{2}}\sqrt{\frac{A_0}{\omega_0} - 1} \end{aligned}. \qquad (9)$$

Finally equation for uniform precession mode c_0 of an ellipsoid can be written in a form:

$$\frac{\partial c_0}{\partial t} = -i\omega_0 c_0 + i\gamma h_{e-} - i\gamma h_{ez}\frac{|B_0|}{\omega_0}c_{-0}^* \qquad (10)$$

where $\omega_0 \equiv \sqrt{A_0^2 - |B|_0^2}$. ω_0 can be treated as a ferromagnetic resonance frequency of an ellipsoid in general case. Substituting concrete demagnetization parameters into equation for ω_0 one can obtain ferromagnetic resonance frequency in different cases. For example for ideal sphere $N_x = N_y = N_z = 4\pi/3$ and we get $\omega_0 = \omega_H$.

Equation (10) describes excitation of uniform precision mode by an external varying field h_{ez} parallel to a saturation magnetization M_0 (parallel pumping) and perpendicular varying field h_{e-} (perpendicular pumping).

For further investigation lets assume that only parallel pumping is applied to the sample. Taking external pumping field in a form $h_{ez} = \frac{1}{2}h_z\left[e^{i\omega_p t} + e^{-i\omega_p t}\right]$, where ω_p is pumping frequency. Substituting this expression into equation (10) and leaving only resonant terms leads to the equation:

$$\frac{\partial c_0}{\partial t} + i\omega_0 c_0 + i\gamma h_z\frac{|B_0|}{2\omega_0}c_{-0}^* e^{i\omega_p t} = 0 \qquad (12)$$

Denoting $V_0 = \frac{\gamma|B_0|}{2\omega_0}$ which has a physical meaning of a coupling parameter between electromagnetic field h_z and uniform precision mode of an ellipsoid c_0. Taking into account dissipation $\Gamma = \gamma\frac{\Delta H_k}{2}$ where ΔH_k is ferromagnetic resonance linewidth in a sample, equation (12) can be written in a form:

$$\frac{\partial c_0}{\partial t} + \Gamma c_0 + i\omega_0 c_0 + i\gamma h_z V_0 c_{-0}^* e^{i\omega_p t} = 0 \qquad (15)$$

At this point it is vital to make some remarks. First of all, equation (15) represents two coupled equations for uniform precision mode amplitude. The coupling parameter has dependence on time $e^{i\omega_p t}$. Such systems are called parametrical and from oscillation theory it is well known that hat in such case energy can be transmitted from the source modulating coupling to the oscillators. If amplitude of a modulation grows beyond some threshold, energy transmitted to the oscillators compensates loses and their amplitude begin to grow exponentially. That's why such processes are called parametric amplification.

This effect can be explained from quantum-mechanical point of view also. Taking into account that quantum analogs of spin-waves are magnons and analogs of electromagnetic pumping are fotons described processes can be explained like foton splitting into two magnons. For such processes energy and momentum conversation laws must be fullfield. Energy conversation law gives a condition for magnon pair frequency, which is $\omega_m = \omega_p / 2$ and momentum conversation law states that magnons in a pair will have equal but oppositely directed moments. This is so because foton momentum is very small comparing to magnons one and can be neglected.

Finally for obtaining expression for threshold pumping field one has to make substitution $a_0 = c_0 e^{i\omega_p t}$ into equation (14). This is classical analog of quantum-mechanical unitary transformation introducing rotating coordinate system. In classical case variables a_0 are so-called "slow" variables. This substitution vanishes term $e^{i\omega_p t}$ near the coupling parameter bringing equation (15) into the ordinary differential equation with constant parameters which can be easily solved. After that (15) takes a form:

$$\frac{\partial a_0}{\partial t} + \Gamma a_0 + i\left(\omega_0 - \omega_p/2\right)a_0 + i\gamma h_z V_0 a_{-0}^* = 0 \qquad (16)$$

In experiments with parametrical amplification condition $\omega_0 = \omega_p / 2$ is always satisfied, so this term in (16) vanishes. Noting that equitation (16) due to complex variables (5) is in fact system of two coupled equations for a_0 and a_{-0}^* we can solve this system with substitution $a_0, a_{-0}^* \sim e^{\eta t}$. Physical meaning of this substitution is next: mode amplitudes exponentially grow infinitely with time with increment η. Thereby threshold condition is $\eta = 1$. After mentioned substitution one can get:

$$\begin{aligned} a_0\eta + \Gamma a_0 + i\gamma h_z V_0 a_{-0}^* &= 0 \\ a_0^*\eta + \Gamma a_0^* - i\gamma h_z V_0 a_0 &= 0 \end{aligned} \qquad (17)$$

Algebraic system (17) has nontrivial solution only if its determinant is equal to zero. Using this condition after some simple math we finally obtain the next expression for parametrical instability threshold in ellipsoid:

$$h_{zthr} = \frac{\omega_p \Delta H_k}{2|B_0|} \qquad (18)$$

or substituting expression for B_0:

$$h_{zthr} = \frac{4\pi\omega_p \Delta H_k}{\omega_M\left|N_x - N_y\right|} \qquad (19)$$

If threshold condition (19) is satisfied then amplitude of mode begin to grow infinitely with time like $a_0 \sim Exp\left[h_z V_0 - \Gamma\right]$.

From expression (19) it is clear enough that threshold field is proportional to the losses. As it was mentioned above this is because external pumping must compensate spin-wave losses. Also from equation (19) we can see strong dependence of threshold from sample form. For example in a case of a sphere one can get $h_{thr} = \infty$ which means that parallel pumping threshold in sphere can not lead to instability. This is so because ellipticity of magnetic precession is needed to cause instability [2].

In a case of thin tangentially magnetized plane we get

$$h_{zthr} = \frac{\omega_p \Delta H_k}{\omega_M} \qquad (20)$$

As we can see parametrical threshold is the lowest in a case of tangentially magnetized plane.

Some typical sample forms and calculated thresholds are given in a Table 1.

Conclusion. Theoretically obtained general expression of parametrical instability threshold in ferromagnetic ellipsoid. Obtained expression describes wide range of sample forms depending on demagnetization factors.

Table 1

Typical sample forms and corresponding thresholds expressions

Sample	Magnetization direction	N_x	N_y	N_z	h_{thr}
Thin plane	Tangential	0	4π	0	$\frac{\omega_p \Delta H_k}{\omega_M}$
	Normal	0	0	4π	∞
Thin cylinder	Longitude	2π	2π	0	∞
	Lateral	2π	0	2π	$\frac{2\omega_p \Delta H_k}{\omega_M}$
Sphere		$\frac{4\pi}{3}$	$\frac{4\pi}{3}$	$\frac{4\pi}{3}$	∞

1. *Ахиезер А. И., Барьяхтар В. Г., Пелетминский С. В* Спиновые волны – М. 1967. 2. *Гуревич А.Г., Мелков Г.А.* Магнитные колебания и волны. – М., 1994. 3. *Schlömann E., Green J.J., and Milano U.* Recent developments in ferromagnetic resonance at high power levels // J.Appl.Phys. – 1960. - Vol. 31, №5. – P. 386S.

Submitted on 09.09.11

UDC 535. 36

A. Mokhovyk, stud., S. Radchenko, Ph.D.

SPATIAL 3D SIMULATING OF THE ULTRASOUND PROPAGATION IN STOCHASTIC HETEROGENEOUS SOFT BIOLOGICAL TISSUES

В роботі наведені результати дослідження впливу локальних стохастичних флуктуацій характеристик середовища, а саме коефіцієнту об'ємної стисливості та густини, на параметри сигналу відлуння при ультразвуковому дослідженні м'яких тканин. Тканина моделюється як двовимірна сітка точкових кульок масою m, розташованих на відстані а одна від одної та з'єднаних невагомими пружними нитками з коефіцієнтом пружності k. Значення параметрів моделі розраховано з відповідних характеристик середовища, а саме коефіцієнту об'ємної стисливості, густини та коефіцієнту затухання м'яких тканин. На основі результатів математичного моделювання показано домінуючий вплив флуктуацій модуля об'ємної стисливості тканин на розкид амплітуди сигналу відлуння від вказаних областей.

Ключові слова: біологічна тканина, точкова модель середовища, розсіяння акустичних хвиль, флуктуації характеристик середовища.

The paper presents results of research on the impact of local stochastic fluctuations of media characteristics, namely the coefficient of volume compressibility and density of the echo signal under ultrasound investigation of soft tissues. Tissue is simulated as a two-dimensional grid of point balls with mass m, located at distance a one from another and connected by weightless elastic springs with a coefficient of elasticity k. The values of model parameters are obtained from the relevant characteristics of the environment, namely the coefficient of volume compressibility, density and attenuation coefficient of soft tissue. Based on mathematical modeling, the dominant influence of fluctuations of volume compressibility modulus variation in tissues on the amplitude of the echo signal from indicated regions was shown.

Keywords: biological tissues, point model of media, scattering of acoustic waves, fluctuations of media characteristics.

Introduction. Local stochastic fluctuations of characteristics media influence on the echo signal is investigated under ultrasound scanning of soft tissues. When there is pathology of functional states, then the media heterogeneity characteristics change. Current task is to find relations variance parameters with functional states of biological tissues for identify pathologies. It will be useful in diagnostics of various diseases.

Backscattering waves, which completed image, dependent on these fluctuations and the task of inverse problem to find out the relation between which statistical distribution of tissue characteristics is the most appropriate for describing the envelope of the backscattered ultrasonic echoes from different type tissues.

Biological tissues in its structure are heterogeneous media, variance parameters are defined as functional states. Its acoustic properties at the microscale level are poorly studied. That is primarily due to the lack of values of many parameters.

Simple theoretical models are usually used for the investigation of dissipating properties of biological tissues. None of the models can fully describe all physical processes taking place in biological tissues during propagation of ultrasonic waves. Depending on the problem, we describe the media in such a model which is good with the relevant properties of tissues. Nowadays the most common is the model of discrete scatters, the model heterogeneous continuum [6] and model of system of coupled oscillators [2].

Biological tissue can be described as a randomly distributed set of point scatters. There is a strong interest of providing a better fit of scattering conditions and correspond to real fluctuation of tissue density and bulk modulus under different pathological states. To make the model closer to the real physical media the density, bulk modulus and attenuation were taken into account.

Method basis. Elastic inertial relaxation oscillation, which varies only in the direction of wave propagation reflected in theoretical model for simulated of propagation acoustic wave. As the basis there was taken a mathematical model describing the tissue as a two-dimensional grid of point balls with mass *m*, located at a distance *a* from each other and connected by weightless elastic springs (Fig.1*)*. The coefficient of elasticity between balls of the model is *k.* Attenuation that is proportional to the velocity is observed when the ball moves. Weight of the balls *m* and coefficient of elasticity springs *k* are some stochastic variables, which are changed according to a given law within certain values. At the input of the systems the perturbation in the form of common mode sinusoidal oscillations of given amplitude and frequency of a certain number of balls is set for some time.

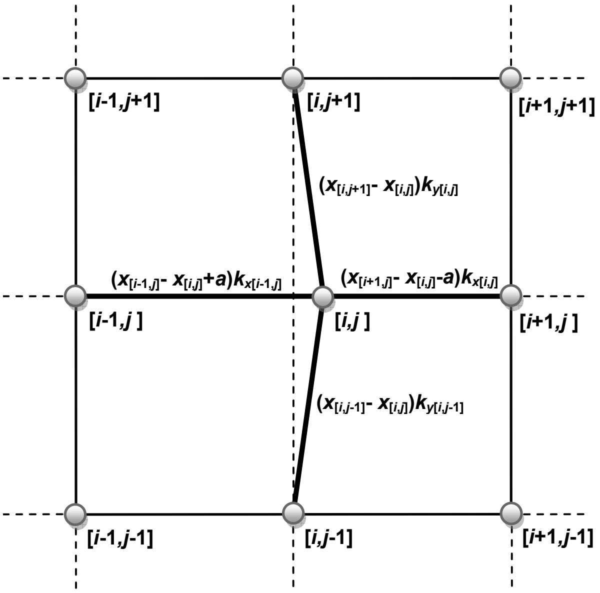

Fig. 1. Spatial scheme of relationships points of the model

The process of acoustic wave propagation is considered as oscillatory movement points model taking into account inertia and relaxation characteristics of grid. Coordinates of points are found as momentary position of relative equilibrium solutions based on Newton's equations of motion (1).

$$m_{[i,j]}\frac{d^2x_{[i,j]}}{dt^2}=(\Delta x_{[i+1,j]}-a)k_{x[i,j]}-(\Delta x_{[i-1,j]}+a)k_{x[i-1,j]}+ \\ +\Delta x_{[i,j-1]}k_{y[i,j-1]}+\Delta x_{[i,j+1]}k_{y[i,j]}+\mu_{[i,j]}\frac{dx_{[i,j]}}{dt} \tag{1}$$

where $m_{[i,j]}$ is mass *i, j* ball, $k_{x[i,j]}, k_{y[i,j]}$, are coefficient of elasticity springs, $\Delta x_{[i+1,j]}$ is distance between *i*+1, *j* and i, *j* balls, $\mu_{[i,j]}$ is damping coefficient of *i, j* ball.

The set of equations is solved by numerical methods based on the Verle algorithm [3]. With Verle algorithm the calculation of the position of each ball with the iterative step *Δt* is implemented:

$$x_{n+1[i,j]}=x_{n[i,j]}+v_{n[i,j]}\Delta t+\tfrac{1}{2}a_{n[i,j]}(\Delta t)^2$$

$$v_{n+1[i,j]}=v_{n[i,j]}+\tfrac{1}{2}(a_{n-1[i,j]}-a_{n[i,j]})\Delta t$$

$$a_{n[i,j]}=\left(F_{el}-\mu v_{n[i,j]}\right)/m\ ,$$

where $x_{n+1[i,j]}$ is a coordinate, $v_{n+1[i,j]}$ is a velocity, $a_{n+1[i,j]}$ is a acceleration of *i, j* balls to *n + 1* step. The presence in the algorithm of the second order of approximation preserves total energy (potential and kinetic energy in consideration of dissipation at any time).

Assuming that our model is a cross section of tissue located at a distance *a* to the same section. Transfer of parameters of biological tissue for one cell carried out the calculation of model parameters. 3D cell of the model with dimensions *a* is provided in Fig. 2.

The parameters of our model (weight of ball, the coefficient of elasticity) are calculated from the known parameters of the biological media (coefficient of volume compressibility and density). The mass was determined with a given density $m=V\rho=a^3\rho$. The coefficient of elasticity was determined from a given coefficient of volume compressibility $K=-V\frac{dP}{dV}=-a^3\frac{-k\Delta/a^2}{a^2\Delta x}=\frac{k}{a}$,. so $k=aK$. Velocity of wave propagation in our model is $c=a\sqrt{k/m}$. Where *ρ* is tissue density, *K* is coefficient of volume compressibility, *a* is distance between the balls of the model, *m* is mass of the ball, *k* is a coefficient of elasticity spring.

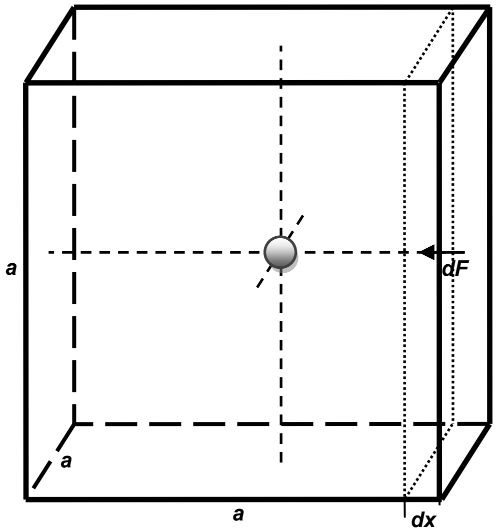

Fig. 2. 3D cell of the model

For full compliance with the real media the following restrictions on model parameters are imposed: wavelength *λ* should be much longer than the distance *a* between the balls; sampling time *Δt* should be smaller than the wave passing through one cell a/c; area diameter of excitation d_{ex} should be more than the wavelength *λ* to consider a wave to be plane; amplitude excitation *A* should be less than the distance between balls *a*; the investigated areas should be further than the near-field region *D,* calculated by the equation $D=\frac{d_{ex}^2}{4\lambda}$ [1].

Results. For the estimations, were used characteristics of water, which are close to the soft biological tissues as a first approximation [5]. Therefore, the following characteristics of media were used: velocity of sound is $c=1500\ m/s$, density is $\rho=1000\ kg/m^3$, coefficient of volume compressibility is $K=225\cdot10^7\ N/m^2$ and coefficient of attenuation is $\alpha=0.005\ dB/cm$.

Calculated parameters of the model: distance between the balls is $a=42{,}8\cdot10^{-6}m$; weight of the ball is $m=78{,}4\cdot10^{-9}g$; an elasticity coefficient of spring is $k=96{,}3\cdot10^3\ N/m$; coefficient of dissipation is $\mu=11\cdot10^{-7}\ N\cdot s/m$. Perturbation is caused by harmonic oscillations at a frequency of $\nu=3{,}5MHz$. Wavelength at a given frequency is $\lambda=0{,}428\cdot10^{-3}m$.

To test the model the backscattering signal from a homogeneous media and velocity of propagation of acoustic wave was investigated. Energy conservation in missing dissipation showed that our model well preserves total energy. The congruence of real value and model velocity of wave propagation was also obtained.

Statistical evaluation was carried out by dependence distribution amplitude scattered at point heterogeneities of the layer, which is located at a distance, which is more than the near-field region, namely 200*a*. From physical considerations, as the variance of soft tissue of volume compressibility coefficient is more than variance of density [4] the following range of model parameters are set. Variance of parameter mass was set from ±1% to ±5% of Simpson distribution**.** Variance of parameter coefficient of elasticity was set from ±1% to ±20% of Simpson distribution.

Dependence of the mean amplitude *A* of the backscattering signal of variance of coefficient of volume compressibility *ΔK* relative to the average, and the backscattering signal of variance of density *Δρ* relative to the average provided in Fig. 3 and Fig. 4 respectively. The amplitudes *A* are normalized of the perturbation signal.

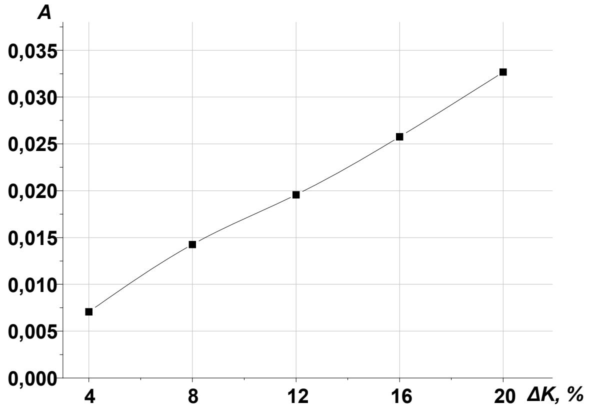

Fig. 3. Dependence of the amplitude of the variance of volume compressibility coefficient

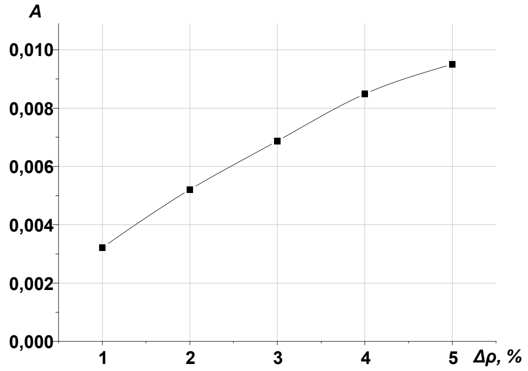

Fig. 4. Dependence of the amplitude of the variance of density

Variance of coefficient of volume compressibility more impact on the fluctuations of the backscattering signal than variance of density because coefficient of volume compressibility in real soft tissues has larger scattering.

The probability density distribution of envelope amplitude of echo signal for the sample of 500 measurements for volume compressibility coefficient variance and density variance were calculated. Frequency of occurrence $f(A_{nc})$ values of normalized centered amplitude, which is calculated by the equation $A_{nc} = (A - A_{av})/\sigma$. Frequency of occurrence amplitude for variance of density ± 5% and variance of coefficient of volume compressibility ± 20%, provided in Fig.5 and Fig.6 respectively.

Analysis of plots of probability density distribution of envelope amplitude of echo signal allows considering them to be of the same shape in the first approximation. The value of standard deviation $\sigma = \sqrt{\sum (A_i - A_{av})^2 / n}$ for plots of scattering of density ± 5% is σ=0.0029 and for plots of scattering of coefficient of volume compressibility ±20% is σ=0.0109. The standard deviation increases with increasing of scattering of the parameter.

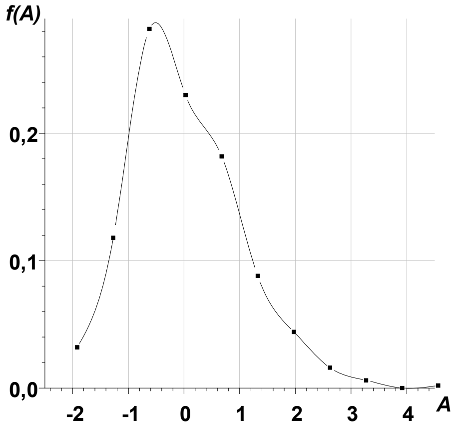

Fig. 5. Frequency of occurrence amplitude for variance of density ± 5%

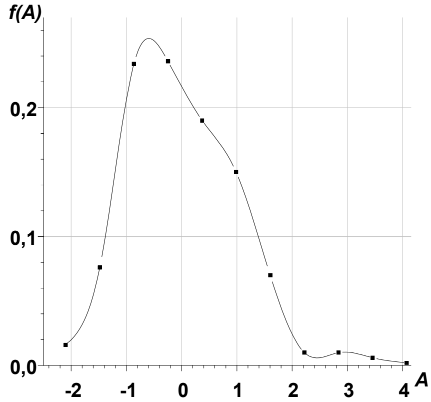

Fig. 6. Frequency of occurrence amplitude for variance of coefficient of volume compressibility ± 20%

Full width at half maximum for plots (Fig.5) of scattering of density ± 5% is $\mathrm{FWHM}_{\Delta K\pm5\%}$=2.1σ, for plots (Fig.6) of scattering of coefficient of volume compressibility ±20% is $\mathrm{FWHM}_{\Delta K\pm20\%}$=2.2σ.

When variance of parameters of tissue is ±1% then the amplitude of backscattering signal is proportional to the noise of system, so the signal at this level cannot be considered to be informative.

Simulation of tissue for 2D and 3D representation is also compared. The relationship between the amplitudes of acoustic waves scattered by inhomogeneity coefficient of elasticity, with fluctuation ±20% for 2D and 3D models of tissue is evaluated. The propagation velocity of acoustic waves for 2D and 3D is the same for the same parameters. But for the 3D model more scattering causes a decrease in echo signal amplitude, therefore during the transition from 2D to 3D the coefficient of dissipation *μ* for the measurements conformity should be changed.

Conclusion. The scattering of acoustic waves in soft biological tissues was studied by methods of mathematical modeling during ultrasound scanning.

There was presented the adequacy of description of the scattering of ultrasonic waves in biological soft tissues using two-dimensional grid of point balls with mass *m*, located at distance *a* one from another and connected by weightless elastic springs with a coefficient of elasticity k (the calculation of model parameters was carried out by the known characteristics of biological tissues). In 3D compared to 2D there is more scattering that leads to a decrease in echo signal amplitude.

By methods of statistical evaluation it was proved that in soft biological tissue the volume compressibility coefficient variance has a greater impact on the fluctuations of the amplitude echo signal than the variance of density of the media.

Variance of coefficient of volume compressibility should be considered as a more informative parameter for determination the functional state of tissue during ultrasound scanning.

1. *Кононов М.В., Радченко С.П., Судаков О.О.* Фізичні основи медичної техніки: Методичні вказівки до проведення лабораторних робіт. – К., 2004. – 36. 2. *Мелешко В.В., Улитко А.Ф., Маципура В.Т*. Вступ до теорії хвилеводів. – К., 2008 3 *Склярова Е. А*. Курс лекций "Общий физический практикум" http://portal.tpu.ru/stud/studentu/Tab/Lk5.pdf, 10.06.2010. 4 *Скрипаченко З., Радченко С.* Статистичне оцінювання параметрів паренхіматозних органів на основі моделі К-розподілу // Біофізичний вісник. – 2006 р. № 16. – С. 70–74. 5. *Уэбб С., Данс Д., Эванс С*. Физика визуализации изображений в медицине. – М., 1991. 6. *Хилл К., Миллер Э., Бэмбер Дж.* Применение Ультразвук в медецине // Физические основы. – М.:Мир, 1989.

Submitted on 10.10.11

UDC 537. 635

A. Netreba, Ph.D., O. Naguliak, engineer,
M. Kononov, Ph.D.

DIFFUSION WEIGHTED IMAGE SEGMENTATION AND RECONSTRUCTION USING SIMPLE MRI DATA

В роботі запропоновано модель процесу сегментації досліджуваних тканин за типом біологічної тканини (сіра речовина, або біла речовина) та реконструкцію зображення біологічної тканини з врахуванням дифузійних процесів води в ній. В якості досліджуваної біологічної тканини взято сіру речовину яка характеризується ізотропними властивостями дифузії. В якості вхідних даних моделі взято реконструйоване зображення об'єкту без врахування дифузійних процесів води.

Ключові слова: ЯМР візуалізація, дифузія води, реконструкція, візуалізація зважена за дифузією, сегментація зображення.

The paper presents a model of segmentation of biological tissues by the type of biological tissues (gray matter or white matter) and image reconstruction of biological tissue taking into account the diffusion processes of water in it. The grey matter tissue type, which is characterized by isotropic diffusion properties of water, is the object of study. The reconstructed image without water diffusion processes is used for input data for image segmentation and further reconstruction.

Keywords: MRI, water diffusion, reconstruction, diffusion MRI, image segmentation.

Introduction. Diffusion MRI is a magnetic resonance imaging (MRI) method that produces in vivo images of biological tissues weighted with the local microstructural characteristics of water diffusion [1-3]. In diffusion weighted imaging (DWI), each image voxel (three dimensional pixel) has an image intensity that reflects a single best measurement of the rate of water diffusion at that location. This measurement is more sensitive to early changes after a stroke than more traditional MRI measurements such as T1 or T2 relaxation rates. DWI is most applicable when isotropic water movement e.g. grey matter in the cerebral cortex and major brain nuclei dominates the tissue of interest—where the diffusion rate appears to be the same when measured along any axis.

Modeling. There have been modeled the process of tissue segmentation and image reconstruction according to the water diffusion characteristics in grey matter. In diffusion-weighted images, instead of a homogeneous magnetic field, the homogeneity is varied linearly by a pulsed field gradient. Since precession is proportional to the magnet strength, the protons begin to process at different rates, resulting in dispersion of the phase and signal loss. The reconstructed object without diffusion weighting was used for segmentation and modeling the spatial density reconstruction with the diffusion characteristics of discovered tissues Fig. 1. The proposed reconstructed image is to be presented like the matrix of signal values without diffusion weighting [4,6]. Image data is to be corrected on water diffusion for obtaining water diffusion reconstruction from simple MRT data [7-9]. For diffusion weighting reconstruction the image segmentation is used.

Image segmentation. For image segmentation and further reconstruction, the simple image data is to be represented like the array of voxels, which stands for volume image episodes. The 2D situation is observed due to the isotropic nature of water diffusion in grey matter and to simplify calculations [11–12]. Such image episodes (voxel) might stand for volume picture elements and consist of the set of pixels. The segmentation is to be provided by the use of Mathematics application. The picture element (voxel) consists of 4*4 pixel elements of simple image data Fig 1. All picture elements are to be identified according to the type of tissue: weather it is grey or the white one. Each type of tissue can be characterized by the signal intensity. After simple image data segmentation, the average intensity values of each voxel are to be calculated and compared with characteristic intensity values of tissue type. All voxels of grey matter are to be reconstructed with water diffusion weighting. Voxels of the white matter are not to be weighted with water diffusion because of its anisotropic nature. Diffusion weighting of white matter is more complex problem [5] and might be the question of next paper.

Image reconstruction. By rearranging the formula for signal lose due to amount of diffusion to isolate the diffusion-coefficient; it is possible to obtain an idea of the properties of diffusion occurring within a particular voxel (volume picture element).

$$\frac{S}{S_0} = e^{-\gamma^2 G^2 \delta^2 (\Delta - \delta/3) D} = e^{-bD}, \tag{1}$$

where S_0 is the signal intensity without the diffusion weighting, S is the signal with the gradient, γ is the gyromagnetic ratio, G is the strength of the gradient pulse, δ is the duration of the pulse, Δ is the time between the two pulses, and finally, D is the diffusion-coefficient. According to the model radial diffusion occurs in grey matter. So the grey matter voxels are to be corrected on radial diffusion

$$S = S_0 e^{-bD\frac{(-(x-x_0)^2+(y-y_0)^2)}{2{\sigma_x}^2{\sigma_y}^2}} \tag{2}$$

After applying radial diffusion to grey matter, new water diffusion weighted reconstruction is to be performed. Obtained reconstructed images of the model with diffusion weighting Fig. 2,a-b. Reconstructed images of the model with water diffusion weighting is of a little bit difference in contrast the one without diffusion. It might give additional diagnostic information taking into account water diffusion in grey mater.

ADC calculation from simple MRI data. By rearranging the formula to isolate the diffusion-coefficient, it is possible to obtain an idea of the properties of diffusion occurring within a particular voxel (volume picture element). These values, called apparent diffusion coefficient (ADC) can then be mapped as an image, using diffusion as the contrast. The first successful clinical application of DWI was in imaging the brain following stroke in adults. Areas which were injured during a stroke showed up "darker" on an ADC map compared to healthy tissue. At about the same time as it became evident to researchers that DWI could be used to assess the severity of injury in adult stroke patients, they also noticed that ADC values varied depending on which way the pulse gradient was applied. This orientation-dependent contrast is generated by diffusion anisotropy, meaning that the diffusion in parts of the brain has directionality. This may be useful for determining structures in the brain which could restrict the flow of water in one direction, such as the myelinated axons of nerve cells (which is affected by multiple sclerosis). However, in imaging the brain following a stroke, it may actually prevent the injury from being seen. To compensate for this, it is necessary to apply a mathematical operator, called a tensor, to fully characterize the motion of water in all directions. According to proposed model the next method of image segmentation and reconstruction might be proposed. The same way of simple MRI image data segmentation is to be used. The image data is divided into voxels according to proposed image data segmentation method. The average voxel intensity is to be calculated according to next formula

$$\bar{S} = \sum_{i}^{k} I_i \Big/ k, \tag{3}$$

where I_i – pixel intensity within the voxel, k – the amount of pixels within the voxel and $\bar{S}$ – the average meaning of signal intensity within the voxel. The next proposed way to obtain the ADC of the voxel is to find diffusion coefficients according next formula

$$\frac{\bar{S}}{S_0} = e^{-bD} \tag{4}$$

where S_0 is the signal intensity without the diffusion weighting, $\bar{S}$ is the signal with the gradient, D is the diffusion-coefficient.

According to proposed method of image segmentation the ADC meaning can be found using next formula

$$ADC = \ln\left(\frac{\sum_{i}^{k} \frac{\bar{S}}{S_0}}{k}\right) \tag{5}$$

Proposed method of calculation of might be used for obtaining more diagnostic information using ADC contrast map Fig. 3.

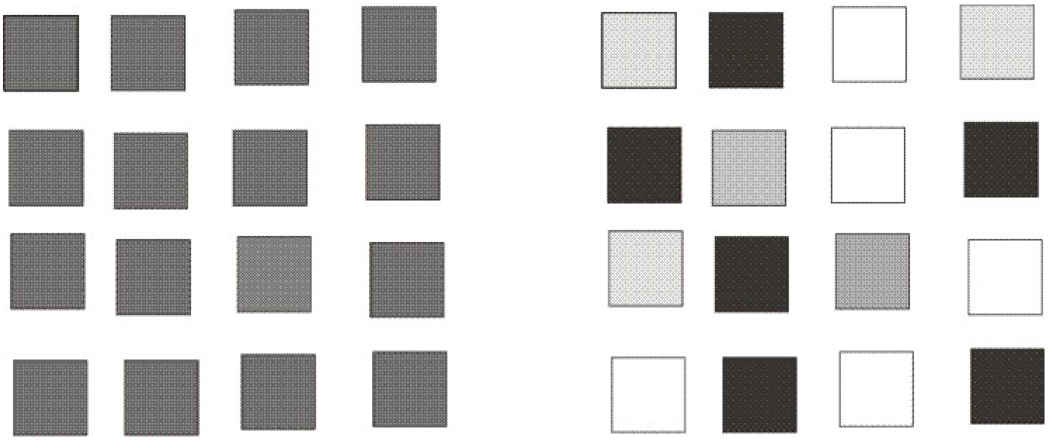

Fig. 1. Image element of 4*4 pixels

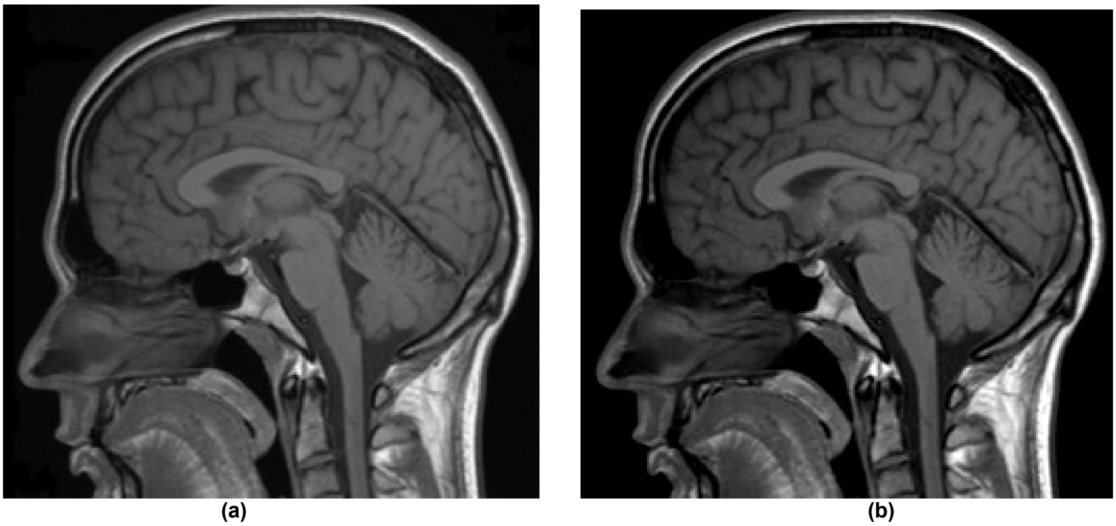

(a) (b)

Fig. 2. Image without diffusion weighting(a), Image with diffusion weighting (b)

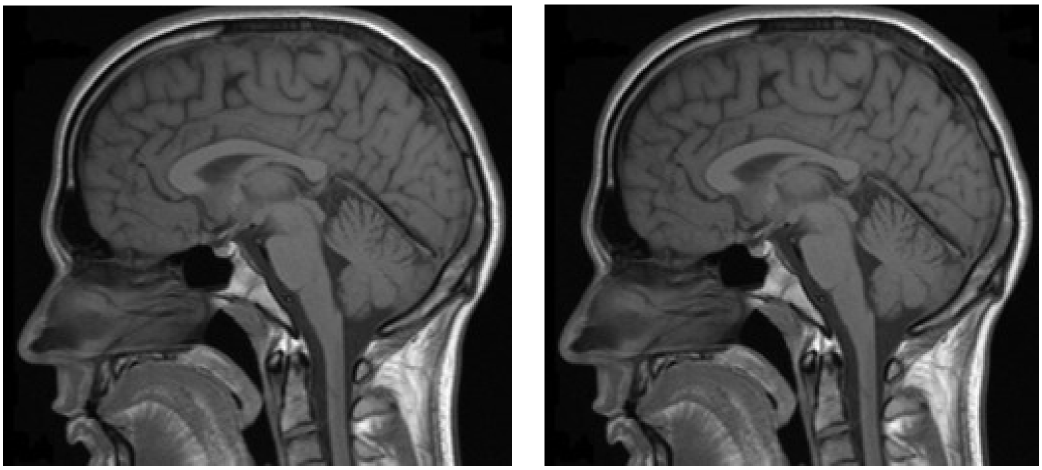

(a) **(b)**

Fig. 3. Image without diffusion weighting(a), Image according ADC contrast map (b)

For more informative image reconstruction it is possible to obtain reconstructed image weighted on water diffusion using simple MRI data. Obtained weighted images give more contrast diagnostic information for early brain diseases following brain stroke, which cannot be marked using simple MRI. The proposed image segmentation method is to eliminate the statistic artifact in high resolution simple MRI images [10]. The proposed ADC reconstruction method gives opportunity to estimate the water diffusion rate within the image element using simple MRI data. ADC using contrast map gives more diagnostic information then simple MRI.

1. Carpinelli G, Carapella CM, Palombi L, Raus L, Caroli F, Podo F (1996) Differentiation of glioblastoma multiforme from astrocytomasby in vitro 1H MRS analysis of human brain tumors. Anticancer Res 16:1559–1563. 2. Chih-Liang Chin, Felix W. Wehrli*, Scott N. Hwang, Masaya Takahashi, David B. Hackney Biexponential diffusion attenuation in the rat spinal cord: Computer simulations based on anatomic images of axonal architecture. 3. Eyal Carmia,T, Siuyan Liub, Noga Alona, Amos Fiata,T, Daniel Fiatc, Resolution enhancement in MRI , Magn Reson Med Sci. 2009;8(1):1-7. 4.Gyngell ML, Hoehn-Berlage M, Kloiber O, Michaelis T, Ernestus RI, Hörstermann D, Frahm J (1992) Localized protonNMR spectroscopy of experimental gliomas in rat brain in vivo. NMR Biomed 5:335–340. 5. Imae T, Shinohara H, Sekino M, Ueno S, Ohsaki H, Mima K, Ohtomo K. Estimation of cell membrane permeability and intracellular diffusion coefficient of human gray matter. 6. Kononov M. Netreba A. Sudakov A. Naguliak O. Reconstruction in NMR by the Method of Signal Matrix Pseudoinversion: Radioelectronics and Communications Systems 2008; 10: 21-25. 7. Manenti; Carlani, M; Mancino, S; Colangelo, V; Di Roma, M; Squillaci, E; Simonetti, G (2007). "Diffusion tensor magnetic resonance imaging of prostate cancer". Investigative radiology 42 (6): 412–9. 8. Mulkern RV, Bowers J (1994) Density matrix calculations of AB spectra from multiple sequences: quantum mechanicsmeets in vivospectroscopy. Concepts Magn Reson 6:1–23. 9. Peeling J, Sutherland G (1992) High-resolution 1H NMR spectroscopystudies of extracts of human cerebral neoplasms. MagnReson Med 24:123–136. 10. Pruessmann KP, Weiger M, Scheidegger MB, Boesiger P. SENSE: sensitivity encoding for fast MRI. Magn Reson Med 1999;42: 952–62. 9. 11.Qing Jia, John O. Glassa, Wilburn E. Reddicka, . A novel, fast entropy-minimization algorithm for bias fieldcorrection in MR images. 12. Yu-Chung N Cheng, Jaladhar Neelavalli and E Mark Limitations of calculating field distributions and magnetic susceptibilities in MRI using a Fourier based method \Phys. Med. Biol. 54 (2009) 1169–1189 doi:10.1088/0031-9155/54/5/005

Submitted on 20.11.11

UDC 537.311.33, 621.315.592

S. Pavlyuk, Ph.D., R. Kuzmych, stud.

IMPACT OF TEMPERATURE TO MODIFICATION OF DIODE'S PARAMETERS OF POWERFUL CURRENT PULSE

В роботі розглянуто вплив зовнішньої температури на модифікацію часу життя носіїв заряду напівпровідникового діода потужним імпульсом струму.

Ключові слова: діод, температура, модифікація, імпульс струму

In this work was considered the influence of outside temperature on the modification of carrier lifetime semiconductor diode powerful current pulses

Key Words: diode, temperature, modification, impulse of current

Introduction. When passing through a semiconductor diode powerful shock pulse of current is changed parameters of the diode [1]. This is due to the fact that the current shock leads excess of the of the maximum permissible effective temperature of the p-n junction, which at the time of service rarely diode with a limited number of repetitions due to unusual conditions of the device. This current can exceed the current direct current diode I tens of times [2]. Joule heating is very heterogeneous. The p-n area transition is heated the most, and contact area by selecting the heat in the output – is heated the least. There is a strong temperature gradient, that leading severe mechanical deformation in the p-n junction. In this area there are additional thermal defects and related additional levels of recombination in the gap semiconductor diode.

These levels are located deep in the gap [3] and lead to a significant increase in the rate of recombination and reduce the lifetime τ of minority carriers in the diode. Studies have shown that changing τ for different conditions reached 10 times.

Research that performed earlier and described in works [1-3], carried out at room temperature. [In a small increase in temperature at 278–373 K was observed annealing thermal defects and increase the lifetime of carriers almost to its original value]. There was annealing thermal defects and increase the lifetime of carriers almost to its original value In a small increase in temperature 278–373 K.

Experimental results. There were researched silicon crystals that used for the manufacture of diodes KD 105, KD 209. They looked like washers with a diameter of 1,8 mm, high - 0,3 mm. The frontal contacts of the crystal are metalized with gold. The basic material is silicon KEF40; p-domein thickness of 0,1 mm, alloyed by boron. The concentration of acceptors in the +- area was Na ~

1017 cm-3, and donors - area Nd ~ 10 14 cm-3. The Methodology of research is described in detail in this work [4].Single pulses of current with adjustable amplitude and duration were conducted in the process of carrying

Also used a DC mode I=const because this mode allows to stabilize in a crystal selected power and reduces the likelihood of crystal's failure [5].

Submitted to the crystal short rectangular current pulses to determine the lifetime τ of change carriers in the diode chip conjoined, the methodology "after injection EMF".

The research was conducted lots of crystals for each temperature of 10 pieces selected from the same initial parameters.

The graphs had the most typical average results because the studies used a lot of crystal diodes and most of them went down during the experiment.

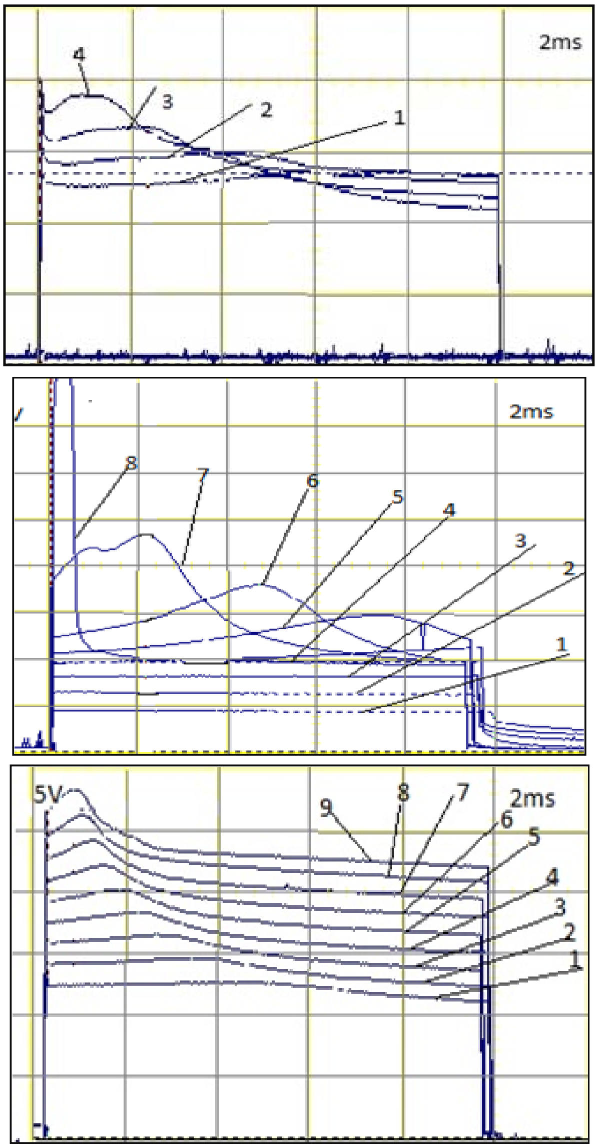

Fig. 1.
(a): T=77 K; I(A);1-35, 2-40, 3-45, 4-50
(b): T=300 K; I(A): 1-5, 2-10, 3-15, 4-20, 5-25, 6-30, 7-35
(c): T=620 K; I(A);1-35, 2-40, 3-45, 4-50, 5-55, 6-60, 7-65, 8-70, 9-75

Research conducted by three outside temperatures: 1: T=77 K, 2: T=300 K, 3:T=620 K. Duration of pulse modification was 10 ms. This duration is most common in practice in twice semiperiodic networking rectifier voltage.

Experimental results and their discussion. The figure 1 shows the oscillogram of decline electrical pressure across the crystal for different temperatures and amplitudes of current's pulses. As we can see in the figure when the amplitude of pulse improves, the fall of voltage increases proportionally. Then there is a peak of voltage and forms s-shaped area.

The figure 2 shows CVC that built for oscillogrames. s-shaped area with temperature T=620 K is absent in explicit form. It's connected with high level of heat conductivity. Because it'll cause that modulation of diode conduction heat with leaking current is negligible.

The figure 3 shows that the lifecycle of charge carrier is depend on amplitude of modificatory pulse of current.

As we can see the biggest influence of τ happens at a room temperature (Fig. 1.a.; 2.3; curve 2). Changes in τ reached 10 times. The initial lifetime is very small at a nitrogen temperature (Fig. 1, A; Fig. 2, 3, curve 1) because charge carriers are at their level and do not participate in conduction. However in gradual heating the temperature of crystal diode increases and the liquid nitrogen starts to boil. Around the crystal appear the shell of nitric gas and the liquid nitrogen stop being cooler. For these conditions the changing τ happens in 5.7 times. But life cycle returns to its initial meaning. In the next heating this diode to a room temperature and in second cooling. There was thermal annealing of defects created by low temperature in heating. The figure 1.b, shows the oscillograms of falling of voltage at a high temperature. The curve 3 in figure 2, shows CVC. The curve 3 in the figure 3 shows the changing lifecycle. The life cycle halves. The meaning of lifecycle keeps in modified form after cooling to a room temperature.

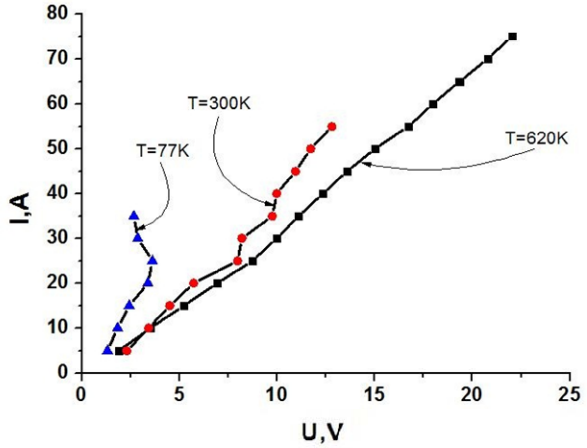

Fig. 2. Diode current-voltage characteristics of crystals with different T

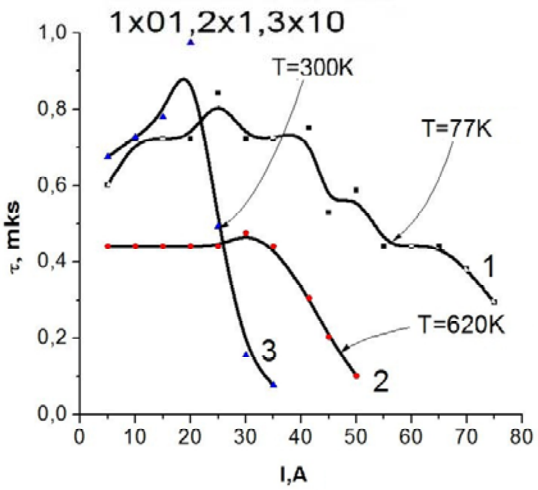

Fig. 3. Change of lifetime of minority carriers at different foreign T

Conclusions: 1. Modification of the lifetime of charge carries in the crystal diode is available in a wide range of external temperature. 2. Modifications of the crystal diodes must conduct at a high temperature for conservation the changing of parameters.

1. *Григорьев О.П.* "Диоды" : справочник / О. П. Григорьев, В. Н. Замятин, Б. В. Кондратьев, С.Л. Пожидаев// Радио и свіязь, 1990. − 336 с. 2. *Нінідзе Г.К.* Вісник Київського університету "Визначення параметрів додаткового рекомбінаційного центру в забороненій зоні кремнійових силових діодів" / Г. К. Нінідзе, В. В. Кушніренко, С. П. Павлюк// " Радіофізика і електроніка" № 9, 2009. −13-15 с. 3. *Нінідзе Г.К.* Вісник Київського університету "Дослідження параметрів модифікованих кремнійових діодів" / Г. К. Нінідзе, В. В. Кушніренко, С. П. Павлюк// Фізіко-математичні науки № 3, 2005.−435-439 с. 4. *Нінідзе Г. К.* Вісник Київського університету "Спосіб контрольованої зміни часу життя неосновних носіїв заряду у P$^+$-N діоді модифікуючими імпульсами прямого струму великої амплітуди" / Г. К. Нінідзе, В. В. Кушніренко, С. П. Павлюк// Фізіко-математичні науки № 3, 2005. −344−347 с. 4. *Павлюк С.П.* Вісник Київського університету "Саморегуляція виділеної потужності напівпровідникового діодного кристала" / С. П. Павлюк, Л.В. Іщук, В.М. Кисліцин// Фізіко-математичні науки № 1, 2002. – 344−347с.

Submitted on 11.11.11

UDC 537.6/.8

O. Prokopenko, Ph.D.

THRESHOLD SPIN-TORQUE MICROWAVE DETECTOR

Запропоновано новий режим роботи мікрохвильового детектора на основі шаруватих магнітних наноструктур, що базується на збудженні прецесії намагніченості з великим кутом прецесії. Проведено аналіз властивостей детектора в цьому режимі роботи і показано, що він працює як широкосмуговий пороговий мікрохвильовий детектор низькочастотних сигналів. Такий режим роботи детектора існує за мікрохвильових струмів $I_{RF} > I_{CR}(\omega)$ і стабільний в області частот $\omega < \omega_{CR}$. Залежність напруги на виході такого детектора від вхідного струму має вигляд сходинки: вона майже нуль при $I_{RF} < I_{CR}(\omega)$ і слабко залежить від I_{RF} при $I_{RF} > I_{CR}(\omega)$.

Ключові слова: магнітна наноструктура, мікрохвильовий детектор, прецесія поза площиною, пороговий детектор.

We propose a novel regime of operation of a spin-torque microwave detector (STMD), based on excitation of large-angle out-of-plane magnetization precession. We analyze the performance of a STMD in this regime and show that detector operates as a non-resonant broadband threshold microwave detector in a wide range of low frequencies. This regime of operations of STMD exists for RF currents with amplitudes $I_{RF} > I_{CR}(\omega)$ and is stable for the frequencies of RF signal $\omega < \omega_{CR}$. The output DC voltage U_{DC} of such STMD has a step-like behavior: it is near zero for $I_{RF} < I_{CR}(\omega)$ and weakly depends on I_{RF} for $I_{RF} > I_{CR}(\omega)$.

Key words: spin-torque microwave detector, out-of-plane precession, threshold detector.

Introduction. The spin-transfer torque (STT) carried by a spin-polarized electric current [1–3, 6, 8–9] can give rise to several types of magnetization dynamics (magnetization auto-oscillations and reversal) and, therefore, allows one to manipulate magnetization of a nano-scale magnetic object [7].

One of possible applications of the STT is the spin-torque microwave detectors (STMD) based on the so-called spin-torque diode effect [5, 10–11]. In a STMD, a microwave current $I_{RF}(t) = I_{RF}\sin(\omega t)$ is supplied to a magnetic tunnel junction (MTJ) structure and excites magnetization precession in the "free" magnetic layer (FL). The resistance oscillations $R(t)$ resulting from this precession mix with the driving current $I_{RF}(t)$ to produce the output DC voltage $U_{DC} = \langle I_{RF}(t)R(t)\rangle$ (here $\langle ...\rangle$ denotes averaging over the period of oscillations $2\pi/\omega$ of the external microwave signal).

In traditional regime of operation of a STMD [5, 10–11] STT excites a small-angle in-plane (IP) magnetization precession about equilibrium direction of magnetization in the FL of a MTJ. In that regime the STMD operates as frequency-selective quadratic microwave detector with resonant frequency that is close to the ferromagnetic resonance (FMR) frequency ω_0 of the FL. Frequency operation range of the detector has an order of FMR linewidth Γ and the output DC voltage of the detector is proportional to the input microwave power: $U_{DC} = \varepsilon P_{RF}$, where ε is the volt-watt sensitivity of the detector and $P_{RF} \sim I_{RF}^2$. Below we shall refer to this regime of STMD operation as the IP-regime. The resonance sensitivity of traditional STMD $\varepsilon = \varepsilon_{res}$ (at $\omega = \omega_0$) is predicted about $\varepsilon_{res} \sim 10^4$ V/W [11], while the best yet achieved experimental result is about $\varepsilon_{res} \approx 300$ V/W [5].

However, the recent experiments performed by Prof. I.N. Krivorotov [3–4] have proved that the sensitivity of spin-torque diodes can be substantially greater and can exceed $\varepsilon \sim 10^5$ V/W. It is important to note that the sensitivity of such STMD is more than 100 times higher than the sensitivity of Schottky diode (about $\varepsilon \sim 10^3$ V/W). The existence of such ultra-high sensitivity of a STMD (substantially larger than the value predicted by the theory [11]) is explained by the existence of so-called "nonadiabatic stochastic resonance" of magnetization excited by the AC STT [4–5].

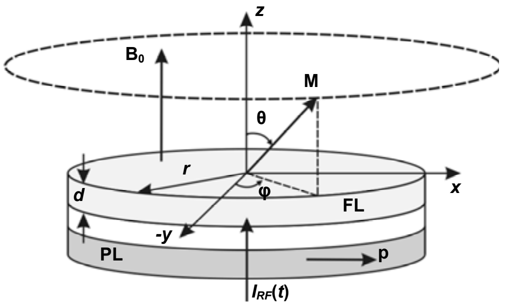

Fig. 1. The model of considered system: circular nano-pillar of radius *r* consists of the "free" magnetic layer (FL) of thickness *d* and the "pinned" magnetic layer (PL). Under the action of RF current $I_{RF}(t) = I_{RF}\sin(\omega t)$ magnetization vector M is precessing along large-angle out-of-plane (OOP) trajectory (shown by a dashed curve) about the direction of a weak DC bias magnetic field $\mathbf{B}_0 = \mathbf{z}\, B_0$ ($B_0 < \mu_0 M_S$), μ_0 is the vacuum permeability, M_S is the saturation magnetization of the FL, p = x is the unit vector in the direction of the magnetization of the PL, x and z are the unit vectors of *x*- and *z*-axis, respectively.

But there may be an alternative explanation of the obtained experimental results. We believe that they may be explained (at least, partially at the qualitative level of severity) by a simple model in which magnetization of the FL is precessing along a large-angle out-of-plane (OOP) trajectory (fig. 1). We shall refer to this regime of operation of a STMD as the OOP-regime.

Hence, the main aim of the article is to analyze the general properties of a STMD in the OOP-regime and prove that the output DC voltage of a STMD may be quite large in this regime.

Model. We consider the OOP-regime of operation of a STMD using simple theoretical model with the following major limitations:

(a) we use the macrospin approach during the theoretical analysis, therefore we assume that the magnetization of the FL $\mathbf{M}$ is spatially uniform and depends on time t only, i.e. $\mathbf{M} \equiv \mathbf{M}(t)$;

(b) the considered MTJ is supposed to be the circular nano-pillar of radius r with no in-plane anisotropy (see fig. 1);

(c) induction of bias DC magnetic field $\mathbf{B}_0$ is perpendicular to the plane of the FL of MTJ ($\mathbf{B}_0 = \mathbf{z}B_0$, where $\mathbf{z}$ is the unit vector of z-axis) and is smaller than the saturation field, i.e. $B_0 < \mu_0 M_S$ (μ_0 is the vacuum permeability, $M_S = |\mathbf{M}|$ is the saturation magnetization of the FL), so the magnetization of the FL is in the unsaturated state;

(d) direction of magnetization of the "pinned" magnetic layer (PL) is defined by the unit vector $\mathbf{p}$ that lies in plane of the MTJ (for simplicity we assume that it lies along x-axis, thus, $\mathbf{p} = \mathbf{x}$);

(e) no DC bias current is applied to the MTJ;

(f) the damping in the system is small, i.e. the Gilbert dimensionless damping constant $\alpha \ll 1$ (its typical value is $\alpha \sim 0.01$).

Theory. In the scope of our model the dynamics of the magnetization vector $\mathbf{M} \equiv \mathbf{M}(t)$ of the FL under the action of microwave current $I_{RF}(t) = I_{RF}\sin(\omega t)$ is described by the Landau-Lifshits-Gilbert-Slonczewski equation:

$$\frac{d\mathbf{M}}{dt} = \gamma\left[\mathbf{B}_{eff} \times \mathbf{M}\right] + \frac{\alpha}{M_S}\left[\mathbf{M} \times \frac{d\mathbf{M}}{dt}\right] + $$

$$+ \frac{\sigma I_{RF}}{M_S}\left[\mathbf{M} \times \left[\mathbf{M} \times \mathbf{p}\right]\right]\sin(\omega t), \qquad (1)$$

where $\gamma \approx 2\pi \cdot 28$ GHz/T is the modulus of the gyromagnetic ratio, $\mathbf{B}_{eff}$ is the effective magnetic field, which has contributions from an external DC magnetic field $\mathbf{B}_0 = \mathbf{z}B_0$ and the demagnetization field, α is the Gilbert damping constant, $\sigma = \frac{\sigma_\perp}{1 + P^2\cos\beta}$ is the current-torque proportionality coefficient, $\sigma_\perp = \left(\frac{\gamma\hbar}{2e}\right)\frac{P}{M_S V}$, $\hbar$ is the reduced Planck constant, e is the modulus of the electron charge, P is the spin-polarization of current, β is the angle between the directions of magnetization in the FL and PL, $V = \pi r^2 d$ is the volume of the FL (r is its radius and d is its thickness), and $\mathbf{p} = \mathbf{x}$ is the unit vector in the direction of the magnetization of the PL.

We represent the magnetization $\mathbf{M}$ in the form $\mathbf{M} = M_S\left(\mathbf{x}\sin\theta\cos\varphi + \mathbf{y}\sin\theta\sin\varphi + \mathbf{z}\cos\theta\right)$ in Eq. (1) and find the equations for θ and φ, where $\theta \equiv \theta(t)$ is the out-of-plane angle between the magnetization and *z*-axis, $\varphi \equiv \varphi(t)$ is the in-plane angle between the magnetization projection on *x–y* plane and *x*-axis (see fig. 1). Note, that under the action of small RF current the magnetization vector is precessing with angular frequency ω of RF current, however, the significant influence of RF current on the motion of magnetization is observed only if the average value of this action is non-zero. Therefore we represent φ in the form $\varphi = \omega t + \psi$, assume that θ and ψ are the "slow" variables, average the equations for θ and φ over the period $2\pi/\omega$ of RF current oscillations and obtain after neglecting small terms ($\sim \alpha^2$):

$$\left\langle \frac{d\theta}{dt} \right\rangle = -\alpha\omega(\theta)\sin\theta + v\frac{\sigma_\perp I_{RF}}{2}\cos\theta\sin\psi, \qquad (2a)$$

$$\left\langle \frac{d\psi}{dt} \right\rangle = \omega(\theta) - \omega + u\frac{\sigma_\perp I_{RF}}{2}\frac{1}{\sin\theta}\cos\psi, \qquad (2b)$$

where $\omega(\theta) = \omega_B - \omega_M\cos\theta$ is the frequency of OOP precession, $\omega_B = \gamma B_0$, $\omega_M = \gamma\mu_0 M_S$,

$$\begin{pmatrix} u \\ v \end{pmatrix} \approx \frac{1}{\sqrt{1-P^4}}\left[1 \mp \frac{\left(\sqrt{1-P^4} - 1\right)^2}{P^4}\right], \quad u, v \approx 1 \text{ for } P \le 0.7 .$$

The stationary solution of Eqs. (2) is $\theta = \theta_S$, $\varphi_S = \omega t + \psi_S$. In that case assuming $\theta_S \approx \pi/2$ one can found from Eqs. (2) that the OOP precession mode exists for microwave currents I_{RF} larger than the critical value

$$I_{CR}(\omega) \approx \frac{2\alpha}{v}\frac{\omega_M}{\sigma_\perp}\frac{\omega}{\omega_B - \omega}. \qquad (3)$$

Also it is follows from Eqs. (2) that the OOP precession is stable for low frequencies $\omega < \omega_{CR} \approx \omega_B$. Thus, it means that STMD operates as a broadband threshold microwave detector in OOP-regime for input RF signals with frequencies $\omega < \omega_{CR} \approx \omega_B$ and currents $I_{RF} > I_{CR}(\omega)$.

If we assume that the angular dependence of MTJ resistance is $R(\beta) = \frac{R_\perp}{1 + P^2\cos\beta}$, then the output DC voltage of a STMD in OOP-regime can be found as

$$U_{DC,OOP} \approx -I_{CR}(\omega)R_\perp\xi, \qquad (4)$$

where $\xi \approx \frac{1}{\sqrt{1-P^4}}\frac{\sqrt{1-P^4} - 1}{P^2} < 0$. One can see from Eq. (4) the output DC voltage $U_{DC,OOP}$ in OOP-regime is weakly depends on input microwave power $P_{RF} \approx I_{RF}^2 R_0/2$, where $R_0 = R_\perp\varsigma$, $\varsigma \approx \frac{1}{\sqrt{1-P^4}}$.

Results and discussion. STMD works as broadband low-frequency non-resonant microwave detector in the OOP-regime in contrast to the traditional resonance STMD. The response of the STMD on input microwave signals with different magnitude I_{RF} is also substantially different in the case of OOP- and IP-regime of operation of a STMD. The output DC voltage $U_{DC,OOP}$ of the diode in the OOP-regime of operation has a step-like dependence:

$$U_{DC,OOP} = \begin{cases} 0, & I_{RF} < I_{CR}(\omega) \\ -I_{CR}(\omega)R_\perp\xi, & I_{RF} > I_{CR}(\omega) \end{cases}. \qquad (5)$$

Thus, in OOP-regime STMD operates as a non-resonant broadband threshold microwave detector of low frequency RF signals.

The results presented above correspond to the case of no DC bias current applied to the MTJ ($I_{DC}=0$). If this is not the case and $I_{DC}\neq 0$, supplied DC bias current may partially or completely compensate damping in the MTJ, that leads to the decrease of critical current $I_{CR}(\omega)$. On the other hand in-plane anisotropy and/or in-plane bias field create energy barrier between regions of small-angle IP- and large-angle OOP-trajectories, which may be overcome by thermal fluctuations or by the supplying DC bias current. This means that large-angle OOP-regime of operation of STMD in a real anisotropic system is thermally- or DC bias current-activated.

Conclusion. We have demonstrated that there is a novel regime of operation of a STMD, based on excitation of large-angle OOP precession mode. In that regime STMD operates as a non-resonant broadband threshold microwave detector of low frequency RF signals. This regime is realized, when magnitude of RF signal greater than the threshold ($I_{RF} > I_{CR}(\omega)$) and the frequency of RF signal ω is smaller than $\omega_{CR}\approx\omega_B$. It is characterized by a step-like dependence of output DC voltage on magnitude of input signal.

The author would like to thank to Prof. A.N. Slavin and Dr. V.S. Tiberkevich for fruitful discussions.

This work was supported in part by grant M/212-2011 of The State Agency of Science, Innovations and Informatization of Ukraine and by grant UU34/008 of The State Fund for Fundamental Researches of Ukraine.

1. *Погорілий А.М., Рябченко С.М., Товстолиткін О.І.* Спінтроніка. Основні явища. Тенденції розвитку // Український фізичний журнал. Огляди. – 2010. – Т. 6, № 1. 2. *Berger L.* Emission of spin waves by a magnetic multilayer traversed by a current // Physical Review B. – 1996. – Vol. 54. 3. *Cheng X., Boone C.T., Zhu J., Krivorotov I.N.* Nonadiabatic stochastic resonance of a nanomagnet excited by spin torque // Physical Review Letters. – 2010. – Vol. 105. 4. *Cheng X., Boone C.T., Zhu J., Krivorotov I.N.* Spin torque diode detectors with sensitivity exceeding that of Schottky diodes // Abstracts of the 55th Annual Conference on Magnetism and Magnetic Materials (MMM 2010, Atlanta, Georgia, USA). – 2010. – EC-03. 5. *Ishibashi S., Seki T., Nozaki T., Kubota H., Yakata S., Fukushima A., Yuasa S., Maehara H., Tsunekawa K., Djayapravira D.D., Suzuki Y.* Large diode sensitivity of CoFeB/MgO/CoFeB magnetic tunnel junctions // Applied Physics Express. – 2010. – Vol. 3. 6. *Ralph D.C., Stiles M.D.* Spin Transfer Torques // Journal of Magnetism and Magnetic Materials. – 2008. – Vol. 320. 7. *Slavin A., Tiberkevich V.* Nonlinear auto-oscillator theory of microwave generation by spin-polarized current // IEEE Transaction on Magnetics. – 2009. – Vol. 47. 8. *Slonczewski J.C.* Current-driven excitation of magnetic multilayers // Journal of Magnetism and Magnetic Materials. – 1996. – Vol. 159. 9. *Slonczewski J.C.* Excitation of spin waves by an electric current // Journal of Magnetism and Magnetic Materials. – 1999. – Vol. 195. 10. *Tulapurkar A.A., Suzuki Y., Fukushima A., Kubota H., Maehara H., Tsunekawa K., Djayaprawira D.D., Watanabe N., Yuasa S.* Spin-torque diode effect in magnetic tunnel junctions // Nature. – 2005. – Vol. 438. 11. *Wang C., Cui Y.-T., Sun J.Z., Katine J.A., Buhrman R.A., Ralph D.C.* Sensitivity of spin-torque diodes for frequency tunable resonant microwave detection // Journal of Applied Physics. – 2009. – Vol. 106.

Submitted on 18.10.11

UDC 539.951

D. Tanygina, post grad. stud.,
I. Anisimov, Dr. Sci., S. Levitsky, Dr. Sci.

FORMATION OF CHARGED PARTICLES' FLOWS IN THE BACKGROUND PLASMA AT THE INITIAL STAGE OF THE BEAM-PLASMA INSTABILITY

Шляхом комп'ютерного моделювання показано, що на початковій стадії розвитку плазмово-пучкової нестійкості в області, де досягається максимум інтенсивності високочастотного поля, формується потік електронів фонової плазми, спрямований назустріч електронному пучку. Виникнення цього потоку пов'язується з початковим етапом деформації профілю концентрації плазми під впливом тиску неоднорідного високочастотного електричного поля.

Ключові слова: плазмово-пучкова взаємодія, пондеромоторна сила, квазістаціонарне електричне поле.

Formation of the flow of the background plasma electrons moving to the electron beam injector at the initial stage of the beam-plasma instability in the region of maximum HF electric field intensity is demonstrated via computer simulation. This flow is caused by the initial stage of the plasma density profile deformation due to the pressure of the inhomogeneous HF electric field.

Key words: beam-plasma interaction, ponderomotive force, quasi-stationary electric field.

Introduction. Interaction of electron beams with plasma is one of the most interesting problems of plasma physics. Most studies of the beam-plasma instability paid the primary attention to instability mechanisms at the linear stage of the beam-plasma interaction. Further studies show that nonlinear effects play the essential role in the beam-plasma interaction. These effects mainly demonstrate themselves in the electron beam, while plasma nonlinearities were generally left out of the scope of researchers. At the same time, plasma nonlinearities were noticed in experiments, for instance, the modular instability of the Langmuir waves, exited in plasma by the electron beam, and the following deformation of plasma density profile with the consequent collapse of cavities [8]. It is evident that nonlinear effects in plasma have to be accompanied by the kinetic effects, like heating of the background plasma by the electric fields, exited by the electron beam, as it was shown in [2]. However, by the present day kinetic effects, which take place during the development of beam-plasma instability, are not entirely studied.

It was noticed in [4] that during the interaction of the electron beam with plasma, according to the law of impulse conservation, the electron beams' impulse is partially transferred to plasma electrons. It results to the formation of plasma electrons' flows. In our latest works formation of such flows was observed at the late stages of interaction, when deformation of plasma density profile started [5].

The aim of the present work is to study the formation of background plasma charged particles' (both electrons and ions) flows at the initial stage of the beam-plasma instability via computer simulation. We consider the initial stage as the time period during which the significant deformation of ions' density profile is not observed; in other words, redistribution of plasma density doesn't lead to reverse influence on the HF-field distribution in plasma.

Model description and parameters. To study the formation of plasma particles' flows, one-dimensional computer simulation using modified package PDP1 [1] was carried out. In 1D space plasma was located between two conductive walls. At the initial time point injection of the monoenergetic electron beam into plasma started from the left wall of the simulation space. Beam electrons were absorbed by the right wall (collector). Initial velocity distribution function of plasma electrons was maxwellian. Simulation was carried out for the beams' current density j_b=24 A/m^2 and beam velocity $V_b=3\cdot 10^7$ m/s. Other simulation parameters: plasma density – $n_{e,i}=2\cdot 10^{15}$ m^{-3} (corresponding electron plasma period – T_p=2,49ns); distance between injector and collector – L=0,5cm; thermal velocities of plasma electrons and ions – $V_{Te}=2\cdot 10^6$ m/s and $V_{Ti}=1\cdot 10^4$ m/s, respectively.

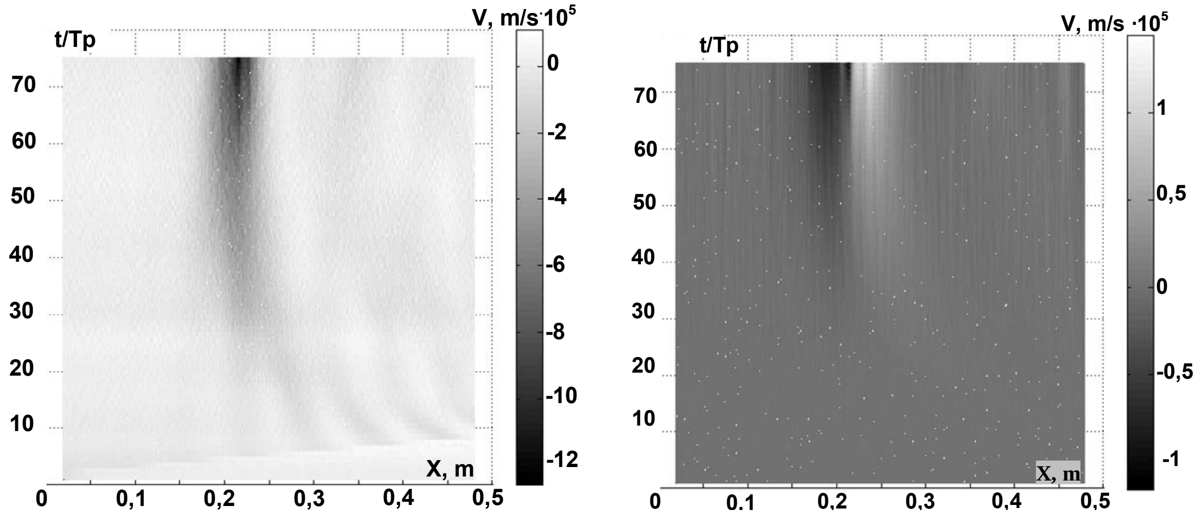

a b

Fig. 1. Space-time distributions of plasma electrons (a) and ions (b) averaged velocity, averaged over the plasma period

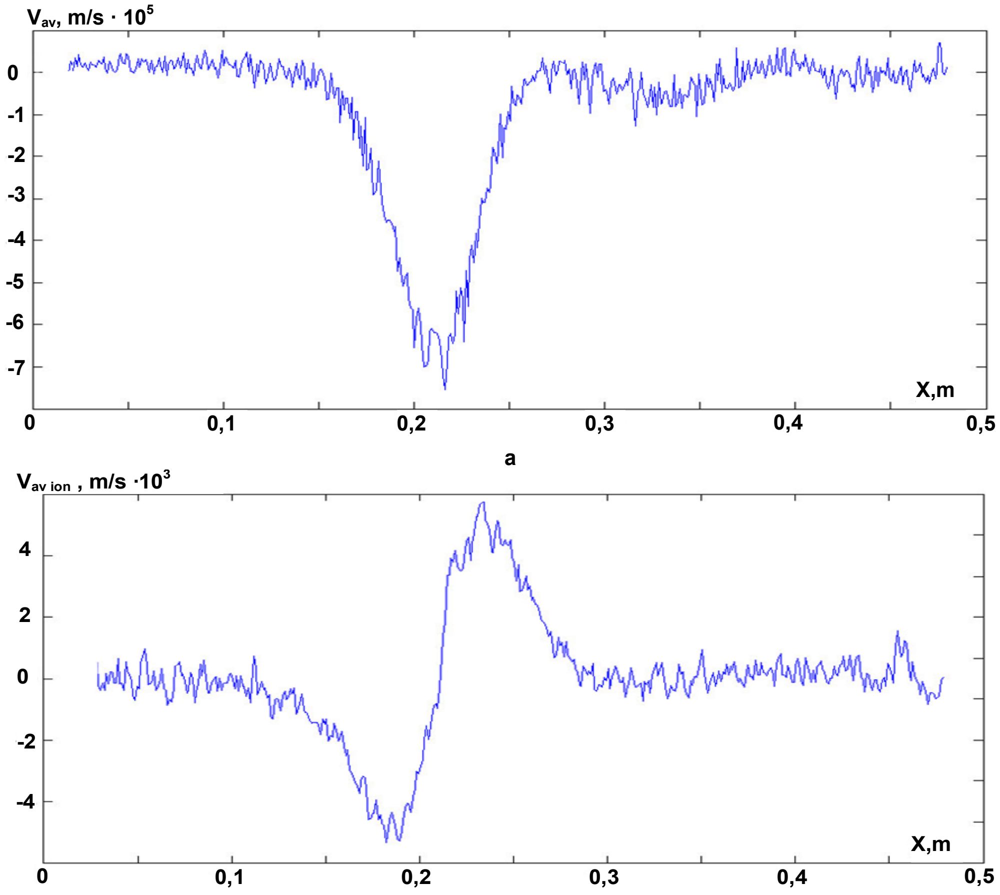

a

b

Fig. 2. Instantaneous space distributions of plasma electrons (a) and ions (b) averaged velocity, averaged over the plasma period, for the time point t=60T$_p$

3. Results and discussion

3.1. Particles' flows formation in the background plasma. Fig.1a,b presents space-time distributions of plasma electrons' and ions' averaged velocities, correspondingly. These velocities were averaged over plasma period and over the ensemble in the small space interval Δx. Corresponding instantaneous space distributions for the time point $t = 60T_p$ are presented on Fig.2a,b.

As it is clear from Fig.1-2, at the initial stages of the beam-plasma instability plasma electrons are accelerated primarily in the direction of the beam injector. At the same time, plasma ions are accelerated both to the injector and to the collector.

3.2. Quasi-stationary electric field is a cause of flows' formation in the background plasma. To explain the results obtained, we considered an instantaneous space distribution of electric field, exited by the electron beam, averaged over the plasma period, for the time point $t = 60T_p$ (Fig.3). In essence, this distribution of averaged electric field represents its slow component (in the time scale of plasma period). It is clear from Fig.3 that area of negative field is located near the injector, while the positive field area with the larger strength value is located near the collector. Localization of flows' formation area coincides with the area of the most intensive quasi-stationary electric field.

Under the influence of negative field, plasma electrons are accelerated to the collector. Consequently they appear in the area of larger positive field, and finally they start to move to the injector. Otherwise, negative field accelerates ions to the injector, and positive field – to the collector. Thus, electrons of the background plasma are accelerated to the injector, while ions are accelerated both to injector, and (primarily) to the collector. Proposed mechanism of the electron flow formation is confirmed by the quasi-stationary potential distribution (Fig.3 c). The right edge of the potential well for electrons is higher then the left one, so plasma electrons are accelerated by the corresponding electric field mainly to the left.

Spatial distribution of quasi-stationary electric field allows to explain the formation of particles' flows in the background plasma (at least, at the qualitative level). Thereby, the electron beam, which is decelerated by the exited HF-electric field, indirectly transfers its impulse exactly to plasma ions. So one can conclude preliminary, that law of impulse conservation is satisfied in the present system.

3.3. Mechanism of the quasi-stationary electric field formation. The quasi-stationary electric field formation is a result of plasma electrical neutrality perturbation owing to the plasma electrons' extrusion from the area of intensive HF electric field (ponderomotive force) [3]. Instantaneous spatial distribution of HF electric fields' intensity, averaged over the plasma period, for the time point t=60T_p is presented on Fig.4. Present mechanism is a first stage of background plasma striction nonlinearity development under the influence of inhomogeneous HF electric field, exited by the electron beam (at the next stage quasi-stationary electric field results to redistribution of plasma ions' density, so quasi-neutrality perturbation is not observed).It is clear from Fig.4, that gradient of the HF electric field intensity is larger from the side of collector comparing with injectors' side. Thus, the magnitude of corresponding quasi-stationary electric field has to be larger, which is in a good accordance with Fig.3.

Fig.4 demonstrates spatial distribution of striction electric field, averaged over plasma period, for the time point t=60T_p. This field is related with HF electric fields' intensity gradient by the expression:

$$E_{str} = \frac{e}{4m\omega_p^2}\frac{d}{dx}\left\langle E^2\right\rangle,$$

where $\omega_p = 2\pi/T_p$ is the electron plasma frequency, $\left\langle E^2\right\rangle$ is the HF electric field intensity, averaged over the plasma period. Comparison of Fig.4c and Fig.3b demonstrates that exactly the striction field makes the main contribution in the formation of quasi-stationary electric field, which results to the formation of plasma electrons' and ions' flows. Asymmetry of the HF field intensity distribution results to the formation of the background plasma electrons' flow directed to the electron beam injector.

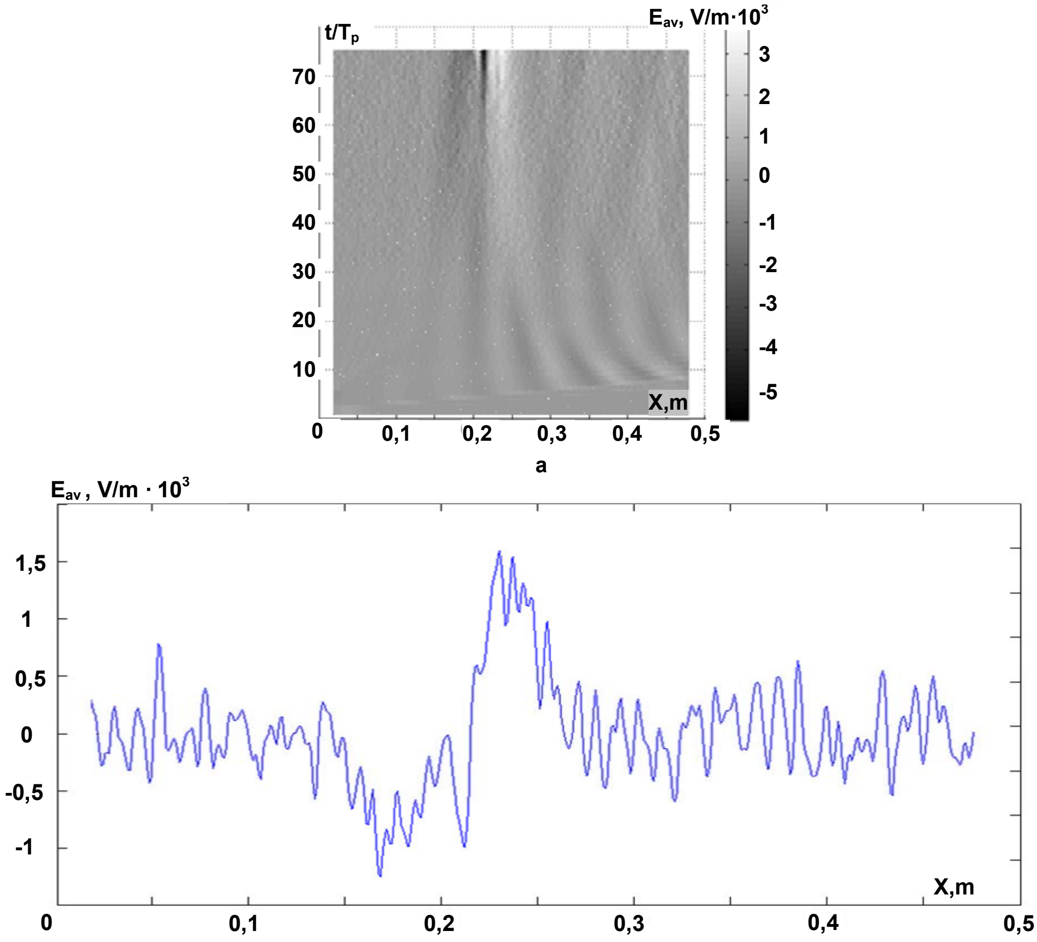

a

b

Fig. 3: (a) – space-time distribution of the electric field averaged over the plasma period; (b) – its' instantaneous space distribution for the time point t=60T_p;

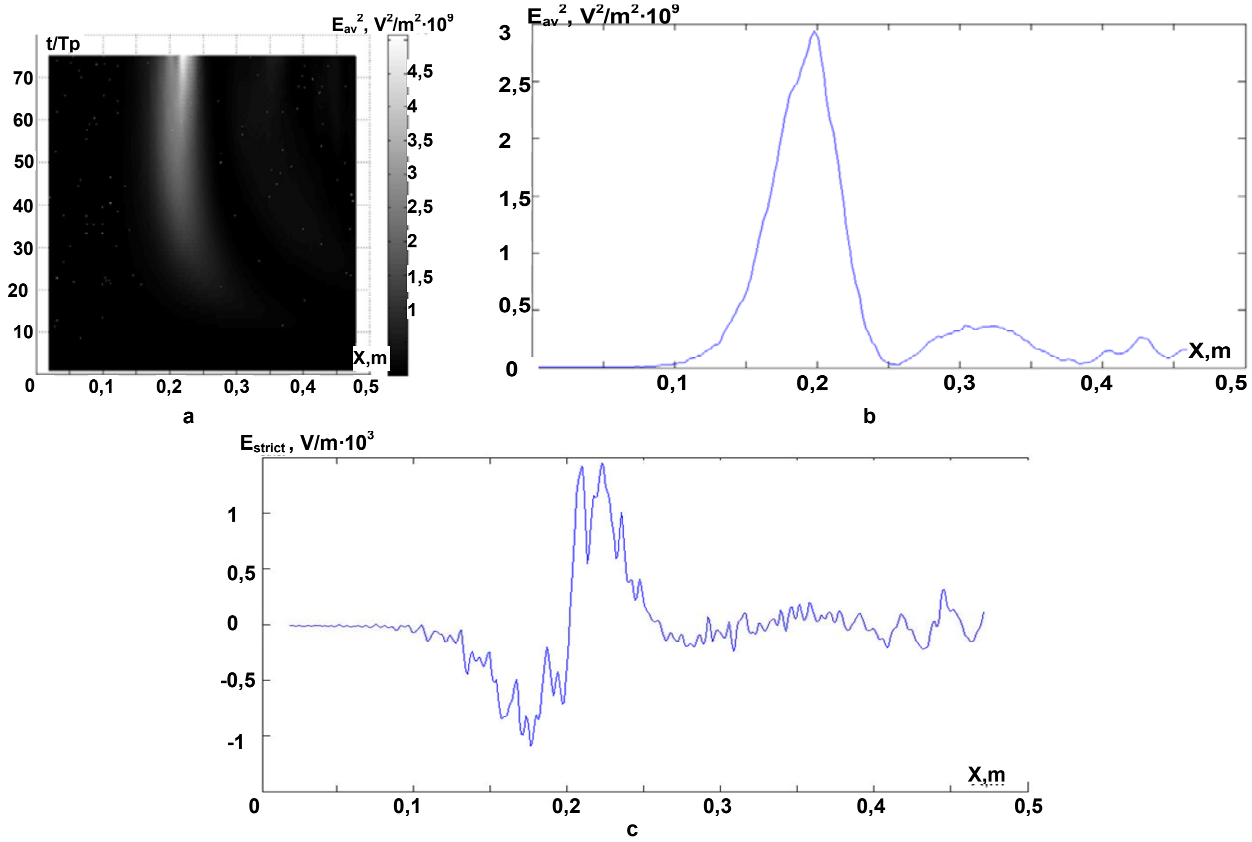

Fig. 4: (a) – Space-time distribution of HF electric fields' intensity, averaged over plasma period; (b) – its' instantaneous spatial distribution for the time point t=60T$_p$; (c) – striction field, caused by the gradient of HF electric fields' intensity for the time point t=60T$_p$.

4. Conclusion. 1. At the initial stages of the beam-plasma instability the flow of plasma electrons appears in the area of the intensive HF electric field. This flow is directed to the electron beam injector (oppositely to the direction of the beam motion). In the same region the flows of plasma ions appear with opposite directions. Moreover, the ions' flow, directed along the electron beams' propagation direction, is more intensive. 2. The cause of plasma particles' flows formation is quasi-stationary electric field, which change its' direction in space. Area of negative field is located nearer the injector, while region of positive field is located further from the injector, and its' absolute value is larger. 3. Calculation shows that the cause of quasi-stationary electric field formation is plasma electrons' extrusion from the region of intensive HF electric field. Thereby, peculiarities of quasi-stationary field space distribution are defined by the distribution of HF field intensity.

Preliminary results of this work are presented in the works [6-7].

1. *Anisimov I.O., Sasyuk D.V., Siversky T.V.* Dynamical System Modelling and Stability Investigation // Thesis of Conference Reports. – Kyiv, 2003. 2. *Cheung P.Y., Wong A.Y.* // Phys. Fluids. – 1985. – 28. – № 5. 3. *Hekker I.R.* Interaction of strong electromagnetic fields with plasma. – Moscow: Atomizdat, 1978 (in Russian). 4. *Tanygina D.M., Anisimov I.O., Levitsky S.M.* // Proceedings of the VI International Conference "Electronics and Applied Physics". – October, 21–24, 2010. – Kyiv, Ukraine. 5. *Tanygina D.M., Anisimov I.O., Levitsky S.M.* // Вопросы атомной науки и техники. Серия: физика плазмы (17). – 2011. – №1. – P. 86–88. 6. *Tanygina D.M., Anisimov I.O., Levitsky S.M.* // Plasma electrons' collective motion and density profile perturbation on the initial stages of beam-plasma instability development. – Proceedings of the XIth International young scientists' conference on applied physics. – June 15–18. – 2011, Kyiv, Ukraine. – P. 180-181. 7. *Tanygina D.M., Anisimov I.O., Levitsky S.M.* // Charged particles' flows formation in background plasma on the initial stage of beam-plasma instability development. // Proceedings of the VII International Conference "Electronics and Applied Physics". – October, 19–22, 2011. – Kyiv, Ukraine. – P. 166–167. 8. *Wong A.Y., Quon B.H.* // Physical Review Letters. – 975. – 34. – № 24. – P. 1499–1502.

Submitted on 11.12.11

Наукове видання

ВІСНИК

КИЇВСЬКОГО НАЦІОНАЛЬНОГО УНІВЕРСИТЕТУ ІМЕНІ ТАРАСА ШЕВЧЕНКА

РАДІОФІЗИКА ТА ЕЛЕКТРОНІКА

Випуск 17

Друкується за авторською редакцією

Оригінал-макет виготовлено Видавничо-поліграфічним центром "Київський університет"

КИЇВський ВПЦ 2012 УНІВЕРСИТЕТ

Формат $60x84^{1/8}$. Ум. друк. арк. 9,0. Наклад 300. Зам. № 212-6043.
Гарнітура Arial. Папір офсетний. Друк офсетний. Вид. № Рф1.
Підписано до друку 30.03.12

Видавець і виготовлювач
Видавничо-поліграфічний центр "Київський університет"
01601, Київ, б-р Т. Шевченка, 14, кімн. 43
☎ (38044) 239 3222; (38044) 239 3172; тел./факс (38044) 239 3128
e-mail: vpc@univ.kiev.ua
http: vpc.univ.kiev.ua
Свідоцтво суб'єкта видавничої справи ДК № 1103 від 31.10.02